COMPACT WAVEGUIDE BENDS AND APPLICATION IN A WAVEGUIDE DEPOLARIZER

by

LIXIA LI

A DISSERTATION

Submitted in partial fulfillment of the requirements
for the degree of Doctor of Philosophy
in
The Optical Science & Engineering Program
to
The School of Graduate Studies
of
The University of Alabama in Huntsville

HUNTSVILLE, ALABAMA

2004

In presenting this dissertation in partial fulfillment of the requirements for a doctoral degree from The University of Alabama in Huntsville, I agree that the Library of this University shall make it freely available for inspection. I further agree that permission for extensive copying for scholarly purposes may be granted by my advisor or, in his/her absence, by the Director of the Program or the Dean of the School of Graduate Studies. It is also understood that due recognition shall be given to me and to The University of Alabama in Huntsville in any scholarly use which may be made of any material in this dissertation.

(student signature) (date)

DISSERTATION APPROVAL FORM

Submitted by Lixia Li in partial fulfillment of the requirements for the degree of Doctor of Philosophy in Optical Science and Engineering and accepted on behalf of the Faculty of the School of Graduate Studies by the dissertation committee.

We, the undersigned members of the Graduate Faculty of The University of Alabama in Huntsville, certify that we have advised and/or supervised the candidate on the work described in this dissertation. We further certify that we have reviewed the dissertation manuscript and approve it in partial fulfillment of the requirements of the degree of Doctor of Philosophy in Optical Science & Engineering.

______________________________ Committee Chair

____

____

____

____

____

______________________________ Program Director

______________________________ College Dean

______________________________ Graduate Dean

ABSTRACT
The School of Graduate Studies
The University of Alabama in Huntsville

Degree Doctor of Philosophy Program Optical Science & Engineering

Name of Candidate Lixia Li

Title Compact Waveguide Bends and Application in a Waveguide Depolarizer

The goal of integrated optics is to integrate more optical functions, such as modulation, switching, generation, and detection, in one optical chip in a compact form. However, the bend radius required for low-index and low-Δ (index contrast) waveguides, such as silica and polymer waveguides, is typically on the order of multiple millimeters, which limits the compactness of planar lightwave circuits (PLCs). To fully utilize the advantages of these low-index and low-Δ waveguides, such as low propagation loss and low coupling loss to optical fibers, decreasing the bend area is highly desired.

This dissertation focuses on designing very compact waveguide bends for low-index and low-Δ waveguides. The 2-D finite-difference time-domain (FDTD) method is used as a design tool to rigorously evaluate the optical bend performance. Some of the designs have applied a combination of micro-genetic algorithm (μGA) optimization and FDTD methods. Single air-interface bends are shown to have high optical bend efficiency when appropriately designed. The waveguide plane wave expansion theory has been used to explain observed behaviors and suggest alternate geometries for high-efficiency waveguide bends. Among them, the approach using multi-layer structures is particularly promising and versatile to create not only compact bend structures but also splitters.

Both amplitude and polarization beamsplitters have been designed and simulated. Combining waveguide bends and polarization beamsplitters, a system-level device, a waveguide-based depolarizer, has been proposed and experimentally evaluated using bulk optical elements.

Since waveguide bends and beamsplitters are such basic and crucial elements for PLCs, higher-level devices, such as directional couplers, resonators, and arrayed waveguide gratings (AWGs), may be redesigned in a more compact fashion using the components proposed in this dissertation.

Abstract Approval: Committee Chair ____________________
(Date)

Program Director ____________________

Graduate Dean ____________________

ACKNOWLEDGMENTS

It is a long journey to pursue a Doctor of Philosophy (Ph.D.) degree, and it is really part of my life. Fortunately, I am not alone along this journey. There are great people who encouraged and supported me so that I could make it to today. First I would like to thank the Center of Applied Optics (CAO) for providing me financial support at the very beginning. Professor David Pollock and Dr. Joseph Geary have helped me work on an interesting MTF optical bench project. My current advisor, Dr. Gregory Nordin, supports and guides me in all kinds of ways; especially he has patiently fine-tuned my academic skills both in writing journal papers and giving oral presentations. Dr. Jianhua Jiang, my husband, is always there to discuss problems, to help on computers, and cook food when back home. He is such a hard-found good fellow. The staff and graduate students in the Nano and Micro Devices Laboratory (NMDL), Linda, Judy, Jermi, Jong, Jinbo, Seung, Bin, and others are all nice and kind to give a hand and make life a little easy and merry. Special thanks are extended to all the other committee members, Dr. English, Dr. Nayyer and Dr. Lindquist, and their help in every phase of my Ph.D. journey are sincerely appreciated.

My dear daughter, Alice, has been my joy and spirit through this journey. She helps and trains me to be a mother while being a scholar. Gratefulness is also owed to my dear parents in China; they always encourage me to overcome any difficulties and go forward to be my best. For all the people above and some beyond, together with my second expected child, I will say I am grateful I have you all in my life along this journey.

TABLE OF CONTENTS

LIST OF FIGURES

LIST OF TABLES

CHAPTER 1

INTRODUCTION

In the integrated optics field, the large bend radius required for low-index and low-Δ (index contrast) waveguides, such as silica and polymer waveguides, is typically on the order of multiple millimeters, which limits the compactness of planar lightwave circuits (PLCs). To fully utilize the advantages of these low-index and low-Δ waveguides, such as low propagation loss and low coupling loss to optical fibers, decreasing the bend area is highly desired.

This dissertation focuses on designing waveguide bends for low-index and low-Δ waveguides. High-efficiency waveguide bends have been designed in very compact and simple form. A system-level device, a waveguide depolarizer, based on compact waveguide bends and polarization beamsplitters, has been proposed and experimentally evaluated using bulk optical elements.

1.1 Motivation

With the widespread commercial deployment of optical components and devices, optical networks that exhibit high speed, high capacity, and configurability are becoming a reality [1]. Nearly 100% of the long haul network, or internet backbone, employs fiber optics and other advanced photonics [2]. Just like optical fibers are the basic "wires" for long haul networks, optical waveguides are the basic light guiding mediums for functional photonics devices, such as switches, couplers, and routers. These devices help distribute optical signals to the proper addresses in a local network. However, some of these devices are still in electronic versions and the data has to be converted back and forth from photons to electrons, and from electrons to photons; thus it slows down the data's communication speed and makes the system complex. Photonics device technology, often called integrated optics, is meant to integrate more and more optical functions such as modulation, switching, generation, and detection in one optical chip to become optical integrated circuits (OICs), or called planar lightwave circuits (PLCs).

Although it is still in its development period, there have been many commercially available optical chips. In the future, these fully-optical devices together with optical fibers-to-the-home (FTTH) would make full-optical communications not a dream. People will enjoy the full advantages from full-optical communications, such as huge bandwidth and extremely large information capacity, immunity to crosstalk and electromagnetic interference, smaller size and weight, lower power consumption, improved reliability, and best of all, the speed of light communications.

In the integrated optics regime, small and compact optical devices are highly desirable since they are crucial to lower power and space consuming, lower costs and higher yields [3]. However, these PLCs have compactness limits most of the time due to the large bend radii required for low-loss transmission, especially for low-index and low-Δ waveguides [4]. Reducing the large bend area without lowering transmission is a problem asking for high bend-efficiency waveguide bends. For traditional circular waveguide bends, bend radii on the order of millimeters is required for all silica waveguides [5], while silica waveguides have waveguide width in only several microns. Obviously these are not compact bends; researchers have proposed some approaches for higher-efficiency bends along the years; however, they all have their pros and cons. This dissertation proposes some novel bend designs with single or multiple air-interface mirror features, and some of the components have been fabricated. Besides compact bend structures, high-performance beamsplitters and one system-level device have been designed in this dissertation. Applications of bends and beamsplitters are ubiquitous, thus more high-level devices, such as directional couplers, resonators, interferometers, and arrayed waveguide gratings (AWGs), may all be redesigned in a more compact fashion using the components proposed in this dissertation.

1.2 Overview of the dissertation

This dissertation mainly focuses on designing high-efficiency compact waveguide bends for low-index and low-Δ waveguides. In this dissertation, the low-index and low-Δ waveguides refer to waveguides (both core and cladding) made from low-index materials, such as silica, or polymer, compared with silicon or GaAs. Their refractive index contrast, given as $\Delta = {(n_1 - n_0)}/{n_0} \times 100\%$, is low compared with waveguides composed from, such as silicon-air, silicon-silica, or GaAs-air. The arrangement of each chapter is organized as follows.

Following the introduction in Chapter1, Chapter 2 gives some literature background about waveguides, waveguide bends, and some tools and methods used in this dissertation.

Chapter 3 focuses on the detailed designs of single air-interface waveguide bends. Different approaches on improving bend efficiency have been explored based on understanding the waveguide plane wave expansion theory in a panoramic view. Some of the bends have been fabricated successfully. Chapter 4 presents multiple-layer bend structures, and the concept is originative and the designs are all very compact, on the order of tens of microns.

Inspired by the waveguide bend structures shown in Chapters 3 and 4, Chapter 5 presents another kind of basic and useful waveguide component, beamsplitters, with one or multiple-layer structures. Two kinds of beamsplitters based on different principles, amplitude and polarization beamsplitters, are presented.

A system-level device, a waveguide depolarizer, has been proposed in Chapter 6 based on compact waveguide bends and polarization beamsplitters. The device scheme, component designs, and lab testing in its bulk version are presented. Finally, summary and conclusions given in Chapter 7 end up this dissertation.

1.3 New contributions

Major new contributions in this dissertation are:

1. All bends are simple, compact, highly efficient, and for low-index and low-Δ waveguides.
2. Multi-layer structures work as waveguide bends with optimized Quasi-Bragg structures and analytically designed Bragg-mirror structures.
3. The waveguide mode plane-wave expansion theory is applied in bend designs based on the mode's angular spectrum with its critical line.
4. A waveguide depolarizer is proposed and components, waveguide bends and polarization beamsplitters, are designed.

CHAPTER 2

BACKGROUND

Optical integrated circuits (OICs) are a developing technology for high-demanding optical communications [4]. Compact, reliable, lower-power-consumption optical waveguide components, both active and passive, are in the commercial need. However, it is now still in its major development stage and various problems remain to be solved both in theory and fabrication. Many famous laboratories around the world are pursuing this technology, including the NTT Optoelectronics Laboratory, Hitachi Cable, BT Laboratories and Lucent Technologies Bell Laboratories. In this chapter, an overview about this technology is given, starting from waveguide materials, mainly silica and polymers. Detailed review is given to waveguide bend approaches available in the literature and their pros and cons. At last, a brief introduction is given to some numerical simulation tools, especially the finite-difference-in-time-domain (FDTD) method. Other important methods used in this dissertation, such as the bend efficiency (BE) calculation using mode overlap integral (MOI) method, and the 3D-to-2D waveguide transformation by effective index method (EIM) are presented at the end of this chapter.

2.1 Waveguide materials

The basic optical guiding mediums for integrated optics circuits are waveguides. To realize these waveguides and all other waveguide-based components and devices, including an optical source, usually the mature waveguide material choice is some optically active materials, such as GaAs, AlGaAs, [6], which can generate light. However, these materials involve some complicated fabrication techniques and are hard to connect with fibers for packaging. Passive materials like silicon, silica (glass), and polymer generally need an external light source to accomplish some source-related functions. However, recently significant progress has been made in producing light emitters and amplifiers by incorporating erbium and other atoms into passive materials such as glasses and polymers. This suggests that it maybe practical in the future to make fully functional monolithic optical integrated circuits (OICs) in inexpensive glasses or polymers.

Silica glasses and polymers are also the two kinds of low-index and low-Δ waveguides with matched optical refractive indexes with fibers, thus inducing low-insertion loss for packaging. Therefore these two materials are showing excellent future promise for practical integrated devices and systems, and more detailed information about their progress in PLCs will be given in the following.

2.1.1 Silica and silicon oxynitride

Among all the materials, silica is the most extensively used material built on the silicon optical bench (SiOB). It involves growing silica layers on silicon substrates by chemical vapor deposition (CVD) or flame hydrolysis (FHD) and patterning or etching by reactive ion etching (RIE). Silica is also the building material for low-loss optical fibers, and the most commonly used singlemode fibers for 1.3 μm and 1.55 μm communication wavelengths have a Δ of ~0.4% and a core diameter of ~8 μm. Waveguides made from silica can be easily made to have very low loss and a well matched geometric shape to optical fibers. The improved fabrication techniques have led to a low loss of 0.017 dB/cm with Δ= 0.45% [7]. The silica waveguides and optical fibers are also matched in thermal expansion coefficient, thus they can be fused together if necessary. However, the highest contrast available for silica waveguides to date under commercial use is only 1.5%, which limits its applications.

Silicon oxynitride is a silica-based material, and waveguides made from this material use SiO_2 as a cladding, and its core can be tunable between SiO_2 and Si_3N_4 (silicon nitride), of index range from 1.45-1.96 [1,8]. The adjustable index contrast (which can be as high as 30%) by changing the nitrogen content is the main attraction of this material. It uses low-pressure CVD (LPCVD) or plasma-enhanced CVD (PECVD) requiring growth time on the order of days.

A variety of planar lightwave circuits have already been developed on silica-based waveguides on silicon substrates, such as splitters, Mach-Zehnder (MZ) interferometer used as switches, and even complicated arrayed waveguide grating (AWG) multiplexers used in dense wavelength division multiplexing (DWDM) telecommunication [9].

2.1.2 Polymer

Although silica waveguide technology is relatively mature, there are some problems, such as fabrication related high cost, high switching power needed in silica-based switching devices, and temperature dependence of the central wavelength of silica-based AWGs [10]. One alternative to silica glass is polymer material. The driving force behind this development is cost reduction. As the size and complexity of fiber optic systems growing, the demand for large quantities of inexpensive integrated optic devices has increased. Polymer material fits right in the tight budget mainly from its low-cost low-temperature high-output fabrication. In addition, the advanced technology for polymer material is in rapid development especially that the transmission losses in multi-mode and single-mode polymer waveguides have decreased rapidly (now at order of tenths of dB/cm at telecommunication wavelength); this hard-won achievement has led to growing interest in the application of polymer waveguide circuits [11].

Optical polymers have been engineered in many laboratories worldwide and some are already available commercially [12]. Classes of polymers for use in integrated optics include acrylates, polyimides, and olefins. By blending and copolymerizing selected miscible monomers, the synthetic scheme allows for precise tailoring of the refractive index over a very broad range of 1.4 ~ 1.7. A larger thermo-optic coefficient (10^{-4}/^{o}C, one order of magnitude larger than that of silica) makes polymers an excellent candidate for power-efficient thermal-optical (T-O) switches. The synthetic scheme allows other physical properties of the materials such as flexibility and toughness as well as such important properties as surface energy and adhesion to be tailored to meet the needs of specific applications. Shortcomings of polymers are thermal mismatch with the widely-used silicon substrate, which can induce stress-induced scattering and undesired guide birefringence.

Waveguides made from polymer materials and waveguide devices built on polymer waveguides are in the phase of development. Polyimide channel waveguides using direct laser writing as interconnections have been fabricated [13]. A similar application is a high-density interconnecting cable for two-dimensional vertical cavity surface emitting laser (VCSEL) arrays [14]. Some passive and even active polymer waveguide device examples are nonlinear optical devices [15], 3 dB (50/50) splitters [16], branching waveguide structures [17,18]. A tapered mode expander for connecting a rectangular waveguide to a cylindrical optical fiber is another fabricated device example [19]. Complicated AWG multiplexers have also been fabricated using polymer materials in different groups [20,21,22]. Some active components, such as phase modulators and switches have been fabricated [23] using some polymer materials with electro-optic effect. Even light emission has been observed [24], and a planar small-size ring laser made from polymers and suitable for applications in integrated optics has been reported [25].

2.2 Waveguide bends

Waveguides are the basic connection “wires” in planar optical circuits, to implement functions by waveguide components, such as couplers, splitters, switches, and so on, most of the time, the light needs to change directions. Waveguide bends are the basic structures for changing directions; in fact, bends are such very basic components that they are looked as part of the waveguides themselves for the waveguide devices. However, to have compact and efficient waveguide bends is not trivial because of the inherent loss existing in the conventional curved waveguide bends.

Three factors contribute to the propagation characteristics of a bent waveguide [26]: pure radiation loss, transition loss between the straight and the bent waveguide, and the phase constant of the propagating field. The radiation loss is the most important factor, and in practice they are ultimately determined by the bending radius curvature and several practical aspects such as the roughness of the waveguide, and the technological process itself. The radiation loss is introduced inherently when the field comes to the bend area since the phase front of the optical field needs to make some turns, and this will bring up distortion to the guided modes. In fact, the minimum allowable radius of curvature of a waveguide is generally limited by the radiation loss rather than by fabrication tolerances [6].

For commercially used silica waveguides with different index contrast Δ as listed in Table 2.1, different bending radii are required to achieve low loss. Note that the meaning of relatively high or low Δ for silica waveguides in Table 2.1 is not the same as what is referred to as low-index and low-Δ waveguides for the whole dissertation. Table 2.1 shows that high-Δ silica waveguides require a smaller bend radius while low-Δ waveguides need a bigger radius, although low-Δ silica waveguides have advantages on the propagation loss and fiber coupling loss. However, the dimension of the bend radius for all the silica waveguides is in the measure of multiple mms, which is really not compatible with the waveguide dimension that is on the order of multiple microns. To achieve compactness for the waveguide bends, some extra methods have to be applied.

Table 2.1 Silica waveguide classification [7]

Characteristics	Low-Δ	Middle-Δ	High-Δ	Super High-Δ
Refractive Index Difference Δ (%)	0.25	0.45	0.75	1.5
Core size (μm)	8 × 8	7 × 7	6 × 6	4.5 × 4.5
Propagation Loss (dB/cm)	< 0. 01	0. 02	0. 04	0. 07
Fiber Coupling Loss (dB/point)	< 0. 1	0. 1	0. 5	2.0 (SMF) ** 0.4 (DSF)
Minimum Bending Radius (mm)	25	10	5	2
Application Field	Small-Scale PLC	Medium-scale PLC	Large-Scale PLC	Very Large-Scale & High-Density PLC

** SMF----single-mode fiber, DSF--- Dispersion shifted fiber

Research on the waveguide bends both in theory and applicable methods has been investigated and reported although most of them are focusing on the high-index waveguides, such as silicon or GaAs waveguides. Several approaches proposed are conventional circular bends, waveguide mirrors, resonator cavities, photonics crystals, and phase compensation methods, which will be reviewed in the following.

2.2.1 Circular bends

A conventional waveguide bend approach is a circular bend as in Figure 2.1(a). As explained above, a circular bend requires the radius of curvature be big enough to make the bend smooth and efficient, which, however, makes the bend less compact, especially for low-Δ waveguides.

It is noticed that the field in the bend section tends to move outwards [27], so lateral offsets have been introduced at the two junctions to maximum the bend performance as shown in Figure 2.1(b). The offset approach has been experimentally verified by some fabricated S-shaped waveguides and 2×2 directional couplers on silica-based waveguides [27].

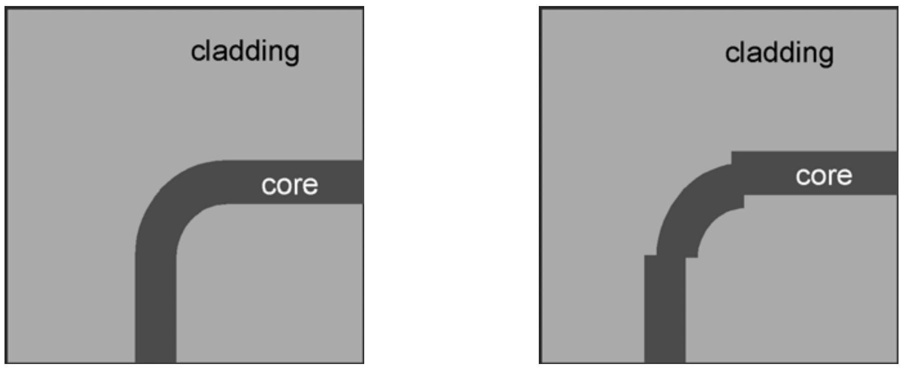

(a) conventional (b) with offset [27]

Figure 2.1 Circular bends

2.2.2 Circular waveguide 90^{o} bends with air-trenches

To improve the power transmission, at the same time, and to shrink the bend radius for circular bends, an isolation air-trench is introduced at the outside of the bend guide [28] as shown in Figure 2.2(a). The isolation trench is shown to reduce the radiation loss considerably by some numerical simulation. The introduction of the air trench forms a high-Δ zone at the high-loss bend area for a low-Δ GaAs waveguide, and the trench works as an obstruction wall to prevent the radiation field going outwards. This air-trench approach has been further improved with the combination of the lateral offset method [29] and other optimized parameters, such as the rib heights and sidewall slopes.

A more rigorous circular waveguide 90° bend with air-trenches on both inside and outside of the bend area is proposed [30] as shown in Figure 2.2(b), and FDTD simulation result shows it can achieve very high bend efficiency. Notice that two set of tapers are added to help the mode transform smoothly, and those tapers are rigorously designed to have special angles.

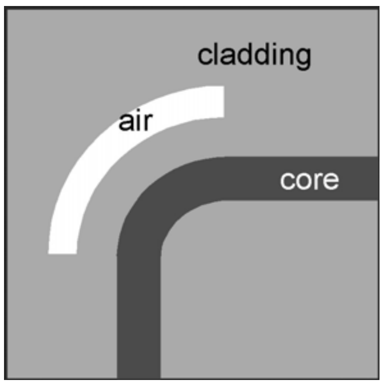

(a) with isolation air-trench outside [28]

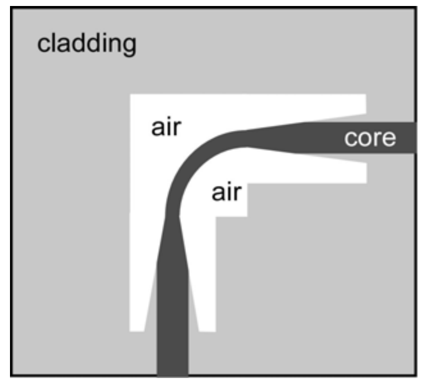

(b) with air-trenches on both sides [30]

Figure 2.2 Circular bends with air-trenches

Another curved GaAs waveguide bend with a deeply etched air-trench square window feature covering the whole bend area has been reported [31] and experimental results show a radiation loss of 0.2 dB/90° for a bending radius of 30 μm.

2.2.3 Mirror bend

Compared with a circular bend which changes directions smoothly, a corner mirror bend can realize abrupt 90° bends in very compact form. The corner mirror can be formed in two ways as shown in Figure 2.3(a) and (b).

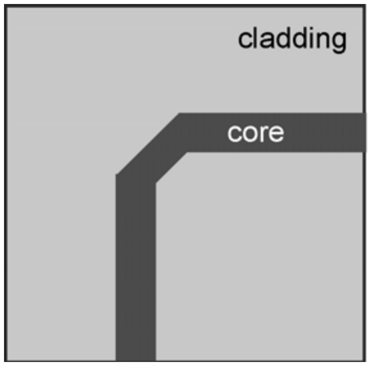

(a) natural 45°-cut mirror [32]

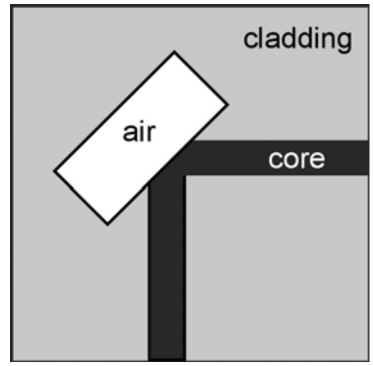

(b) air-trench mirror [36]

Figure 2.3 Mirror bends

For waveguides with high-index core material such as silicon, a natural total internal reflection (TIR) mirror can be formed with a 45°-cut etching surface at the bend area [32]. To form the TIR mirror as in Figure 2.3(a), the cladding material should be chosen to give high Δ between the core and cladding, such as Si-SiO_2 or Si-air. These high-index and high-Δ waveguides usually have a waveguide core width of less than 1 μm to maintain singlemode waveguides. Several groups have successfully fabricated ultracompact corner mirrors with a bend size in the measure of μms in silicon-on-insulator (SOI) material [33,34,35].

The mirror approach shown as in Figure 2.3(b) has an etched single-interface air trench at the outside of the bend to create a high-Δ facet as the mirror either having TIR or large partial reflection. This approach works for both high-index and low-index waveguides, but mostly the core and cladding has low Δ, and the air zone is necessary to help increase the index Δ, thus increase the reflection.

An air-trench mirror for GaAs low-Δ single-mode rib waveguides has been fabricated with different waveguide width 4, 6.4, or 8 μm [36]. An experimental bend efficiency 60 to 90% has been measured for the latter two 90° waveguide bends. The loss is attributed to fabrication tolerance, the surface sidewall roughness, verticality, displacement, rotation of the etched mirror surface. Applying the self-aligned fabrication techniques can improve bend efficiency up to 90% [37]. Two loss mechanisms, tilting and surface roughness, have been numerically analyzed for GaAs waveguide bends [38]. A 45° mirror bend is fabricated for the GaAs waveguide with a higher experimental bend efficiency of 93.3% [39].

Single-interface air-trench 90° bends have also been successfully fabricated for silica-based low-Δ waveguides [40,41]. Experimental results agree well with analytical or simulated results for both TE and TM polarization. Mirror insertion loss has been mostly attributed to the mismatch between the reflected wave and the output waveguide due to the Goos-Hanchen shift effect. Another loss mechanism is described as diffraction to the air medium due to the lateral numerical aperture of the mode. Surface roughness and perpendicularity are accounted as other loss factors from fabrication. Both authors in [40,41] use the waveguide mode plane wave expansion theory to calculate the transmission at the mirror interface.

Another theory of explaining the propagating mechanism at the waveguide bend is called mode expansion. The wave propagation in a perturbed (bent) waveguide can be approximated by a linear combination of the unperturbed (straight) eigenmodes, including the modes under cutoff [42,43]. For a single-mode waveguide bend, only two modes, the fundamental mode and the first leaky mode are enough to give an accurate explanation.

2.2.4 Resonator cavities

A resonator cavity is another waveguide bend approach working for high-Δ waveguides such as Si-air waveguides [44]. Shown in Figure 2.4(a), a high-index material is added at the inside corner of the 90° bend. The cavity can be the same material as the core material of the waveguide. This design is inspired by the principle of weakly coupled resonators, which predicts that a symmetric resonator with four ports can couple an incoming channel to an outgoing channel without reflection. Here the input and output waveguides correspond to the four ports (forward and backward traveling modes in each of the two arms) with the enlarged cavity being the resonator having a square side. The resonator method has also been applied to the mm-wave regime [45].

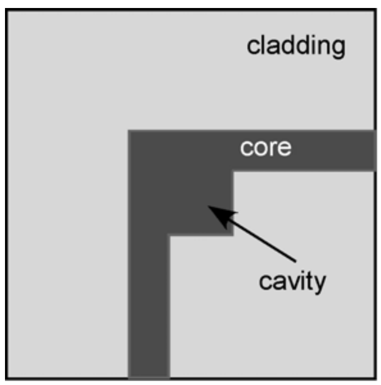

(a) cavity at the inside corner

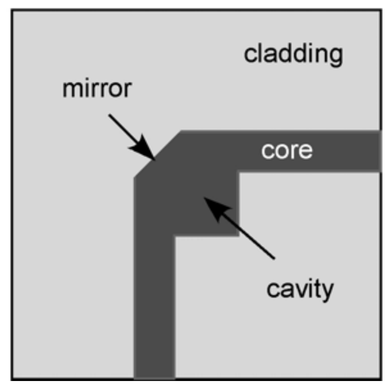

(b) improved resonator (with a mirror)

Figure 2.4 Resonator cavities [44]

The bend performance in Figure 2.4(a) can be further improved by adding a 45°-cut at the outside to remove some more radiation loss as shown in Figure 2.4(b) [44]. This configuration can be looked as a combination of resonator cavity and mirror structures. The strongly guided waveguide mode undergoes total internal reflection at the 45°-cut outside wall and is also guided by the resonator cavity inside the corner.

Although the authors of [44] explain Figure 2.4 based on cavity resonance principle, the authors of [32] explain it as index-guiding, that is, judiciously placing dielectric features can greatly enhance guiding of a waveguide mode when it encounters a bend. This explanation is similar to the prism coupling. A German group [46] has done a 90° bend 2D-FDTD numerical simulation for this approach showing a bend transmission of 95% for a waveguide with core and cladding indices of 2.0 and 1.0.

2.2.5 Photonic Crystal bends

Photonic Crystals (PhCs) are periodic dielectric arrays scattering in homogeneous dielectric matrices [47]. By this periodic property, photonic crystals provide a means to control and manipulate the propagation of the light.

Traditional PhC 90° bends as shown in Figure 2.5(a) are formed by inserting a line of defects that can support a localized mode having a frequency located within the photonic band-gap (PBG) [48]. A 60° PhC waveguide bend has been successfully fabricated with measured bend efficiency near 100% at certain frequency near the valence band edge [49].

Using the self-collimation effect of PhC [50] and combining single-interface 45° air-trench mirror, a non-channel PhC 90° waveguide bend is proposed and fabricated as shown in Figure 2.5(b). The measured bend efficiency is about 80%, which matches the 3D-FDTD simulation result very well.

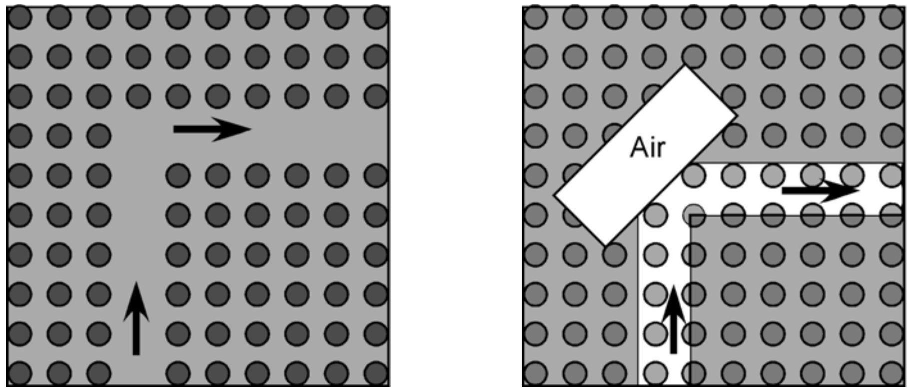

(a) traditional [48]

(b) hybrid with non-channel planar PhC waveguide and air-trench [50]

Figure 2.5 PhC waveguide bends

Another approach under investigation by Seung Kim in our group is using periodic PhC itself as a reflector by hybrid with the conventional waveguide to accomplish a 90° bend [51].

However, the insertion loss as well as the scattering into the third dimension are still concerns for the photonic crystal approach.

2.2.6 Phase compensation methods

The approaches stated so far are mostly focusing on dramatic direction change, such as a sharp 90°. For a mild and shallow direction change in several degrees, phase compensation methods have been proposed in several ways by adjusting the refractive index at the corner to bring a smooth transition of the modal field shape, or the phase front.

One way is to induce a lower-than-cladding refractive index material at the outside of the corner to accelerate the phase front at the outside, which is called phase-front accelerator [52]. Another way is to insert a higher-index triangular-shape microprism in the bend junction as the phase compensator for a silica waveguide [53], which has simulation transmission 95% for a bend angle of 10°.

One novel phase compensator has a shape of apexes-linked circle grating [54], which works on the principle of not only compensating the phase-difference in the bend corner, but also avoiding distorting the eigenmode for the straight waveguide. Power bend efficiency 89% is predicted from numerical simulation.

Based on the same phase compensation principle, another structure called bulged and chamfered (BC) bend [55] is essentially flattening the one-corner bend to two corners with the core material. Simulation predicts transmission 99% or 92% for a bend angle of 5° or 7° while the former 99% (5°) has been verified experimentally.

2.3 Tools and methods used in this dissertation

As the demand for photonic devices getting higher, the need for efficient design tools is becoming urgent. Like any other computer-aided design (CAD) tools used in other fields, such as AutoCAD for mechanical designs, and Max Plus II for large-scaled electronic circuit designs, CAD tools are needed in the photonics field. Using a CAD tool can design, predict and optimize the device's performance before fabricating the photonics devices, and so lower the whole cost. The difference here for photonics designs is that the photonics device dimension is extremely small, in the measure of multiple microns, and the electromagnetic field involved is in the optical frequency domain. There are some commercial softwares available, such as *BeamPROP* from *Rsoft* [56], and *Fimmwave* from *Photo Design* [57]. The numerical methods widely used by these softwares are the Beam Propagation Method (BPM), and Finite-Difference Time-Domain (FDTD). There are others, such as Coupled Mode Theory (CMT), Transfer Matrix Method (TMM), Finite Element Method (FEM), Eigenmode Expansion Method (EEM).

Our group has developed our own FDTD tool, and its unique feature is that it combines optimization and simulation at the same time by combining micro-generic algorithm (μGA) and FDTD together. With this unique feature, the device is really being designed and not only just being simulated. The main design and simulation work of this dissertation is accomplished by using the FDTD tools developed by our own group. In the following, more information about these numerical methods and their applications are given.

2.3.1 Introduction to FDTD, μGA-FDTD, and others

The finite-difference time-domain method (FDTD) is one of the mostly used numerical methods to solve electromagnetic problems. The FDTD method uses the Yee algorithm developed by Yee in 1966 [58]. The Yee algorithm solves for both the electric and magnetic field in time and space domains rigorously using the coupled Maxwell's curl equations, rather than solving for one field using the wave equation. Incorporating a time-dependent incident filed, time-marching is accomplished by repeatedly implementing the finite difference equations at each cell of the simulated area [59]. After a steady state is reached, the near field information can be extracted. Through an appropriate near-to-far transformation algorithm, the far field response can also be generated. Because of the time-dependent nature of FDTD, both the transient and steady-state of the device can be obtained. By employing pulse incident sources, the spectrum response of the device can be obtained within a single run. The perfectly matched layer (PML) absorbing boundary condition (ABC) [60] can match the impedance of free space and absorbs electromagnetic energy at any frequency and incidence angles.

The rigorousness of FDTD method allows that it can model light propagation, scattering, and diffraction, reflection, and polarization effects. It can also model material anisotropy, dispersion and nonlinearities without any pre-assumptions. The only drawback of this method is that it requires typically at least $\lambda/20$ grid size to minimize the numerical dispersion, which requires higher memory for the computer [61].

Analogous to natural genetics, a genetic algorithm (GA) is developed mainly for optimization in all kinds of fields. The GA has been intensively used in electromagnetics and antennas in the last ten years. Recently it has been borrowed for the waveguide-based photonics device designs by combining with some of the numerical methods mentioned above [62]. The micro-GA (μGA) has applied some more efficient optimization algorithms, thus it can find solutions faster in a more efficient way. The combination of μGA and FDTD is the unique and powerful feature of our FDTD tool, and it has been used successfully to design some diffractive optical elements (DOE's) [63].

Besides the FDTD method, the beam propagation method (BPM) is another mostly used numerical technique for modeling integrated and fiber photonic devices [64]. The most significant feature of BPM is that it is straightforward and allows rapid implementation of the device simulation. The BPM is essentially a numerical solution with paraxial approximations, which, however, places restrictions on the index contrast for the waveguide material and eliminates the backward propagation, like from the reflection surface. The finite-difference BPM (FD-BPM) method is propagating the field in a stepwise manner through slices of a known waveguide structure. The polarization effect can be considered in BPM through full-vectorial BPM, or semi-vectorial BPM. Incorporating a wide-angle and bi-directional techniques, wide-angle BPM and bi-directional BPM methods can relax the paraxial and single-direction approximations and so extend its applications [65].

The eigenmode expansion method (EEM) can give exact analytical solutions in principle by using an infinite number of modes in doing expansion [66]. Because the guided and radiation modes from a waveguide together form a complete basis set, so any solution of Maxwell's Equations in the region of the waveguide can be expressed as a superposition of this basis set. This basis set is called eigenmodes, and each eigenmode is characterized by its specific field distribution and propagation constant. The expression for any other solution using this basis set is doing an eigenmode expansion. It uses an efficient scattering matrix (S-matrix) technique, so it takes almost the same time for a beam to propagate 1 μm or 1mm. However, structures with large cross-section take longer computational time, and it is difficult to find and include all the modes in some cases.

The above methods can be used alone, or can be combined together to extend the application regime.

2.3.2 Bend efficiency calculation using mode overlap integral method

Since the main work for this dissertation is to design waveguide bends, an effective method to measure bend performance is needed. Several papers have mentioned using the mode overlap integral (MOI) method to calculate the bend efficiency (BE) [40,41,67,68]. Using the MOI method, the modal coefficient included in an arbitrary field in terms of waveguide modes can be first derived [69], and then the power ratio included in the reflected field as the output waveguide mode can be derived. This power ratio will stand for a ratio of output power to the incident power, and that output power is the power settled down in the output waveguide as the waveguide mode part after some leaking process for those non-mode parts. This power ratio calculated by the MOI method does not change along the propagation of the output waveguide. Therefore, the simulation size can be just big enough to cover the bend feature and the input and output arms do not need to be very long, which can dramatically decrease the computer requirement. In the following, this method is reviewed and developed in detail.

(1) Mode overlap integral (MOI) method

As shown in Figure 2.6, a field having an arbitrary shape is launched into a 2D single-mode slab waveguide, and the power percentage included in this field as the mode for the output waveguide is wanted, which is also the power that will eventually settle down in the output waveguide. This part of power should not change along the propagation of the waveguide if no other loss mechanism is introduced.

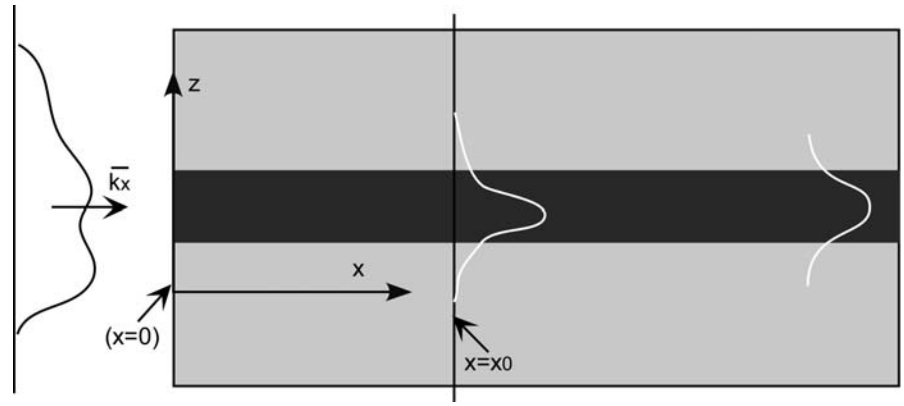

Figure 2.6 Illustration of mode overlap integral (MOI)

First, let's start field propagation from $x=0$. Because of the orthogonal property for the waveguide modes, mathematically, an arbitrary electro-magnetic field can be expressed both its $E(z)$ and $H(z)$ components individually as follows:

$$E(z)=\sum_m a_m E_m(z) \ , \tag{2.1}$$

$$H(z)=\sum_m a_m H_m(z) \ , \tag{2.2}$$

where $E_m(z)$, $H_m(z)$ stand for waveguide modes, and a_m represents the modal coefficient. Then, taking vector products on both sides of Equation 2.1 with the complex conjugate of the transverse magnetic and Equation 2.2 with the complex conjugate of the transverse electric field of one particular mode (say, the nth mode), H_n^* and E_n^* respectively, integrating over a cross section for its power, the following two equations are received:

$$\int [E \times H_n^*] \bullet \hat{k}_x dz = \int \sum_m a_m [E_m \times H_n^*] \bullet \hat{k}_x dz \quad , \tag{2.3}$$

$$\int \left[E_n^* \times H\right] \bullet \hat{k}_x dz = \int \sum_m a_m \left[E_n^* \times H_m\right] \bullet \hat{k}_x dz \quad . \tag{2.4}$$

Adding Equations 2.3 and 2.4 together gives

$$\begin{aligned} \int [E \times H_n^* + E_n^* \times H] \bullet \hat{k}_x dz &= \int \sum_m a_m [E_m \times H_n^* + E_n^* \times H_m] \bullet \hat{k}_x dz \\ &= \sum_m a_m \int [E_m \times H_n^* + E_n^* \times H_m] \bullet \hat{k}_x dz \end{aligned} \quad . \tag{2.5}$$

From the orthogonal condition for the waveguide modes, the right-hand side of Equation 2.5 will be zero for all terms except $m = n$, thus

$$\int [E \times H_n^* + E_n^* \times H] \bullet \hat{k}_x dz = a_n \int [E_n \times H_n^* + E_n^* \times H_n] \bullet \hat{k}_x dz \quad . \tag{2.6}$$

Then, the modal coefficient a_n for the nth mode can be written as

$$a_n = \int [E \times H_n^* + E_n^* \times H] \bullet \hat{k}_x dz \, / \int [E_n \times H_n^* + E_n^* \times H_n] \bullet \hat{k}_x dz \quad . \tag{2.7}$$

Assuming launched EM field is propagating in $\hat{k}_x$ direction, and expressing H_n and H as E_n and E with $H_n = E_n / \eta = E_n \bullet n_{eff} / \eta_0$ and $H = E / \eta = E \bullet n_{eff} / \eta_0$, Equation 2.7 can be rewritten in a short form as

$$a_n = \int E \bullet E_n^* dz \Big/ \int |E_n|^2 dz \ . \tag{2.8}$$

Note that the integral in the denominator of Equation 2.8 really represents a normalization factor, and the integral in the numerator is more important. It is often called mode overlap integral (MOI) because it represents the overlap of the input field $E(z)$ with one particular mode $E_n(z)$. This is really a measure of how similar the input field is to the n^{th} mode. Clearly, if the two fields are actually identical, the modal coefficient $a_n = 1$. It should be noticed that this coefficient a_n is measured at position $x = 0$ with field $E(z)$. Equation 2.8 can be further expressed in inner product form as

$$a_n = \langle E, E_n \rangle \Big/ \langle E_n, E_n \rangle \ , \tag{2.9}$$

with $\langle E, E_n \rangle = \int E \bullet E_n^* dz$, and $\langle E_n, E_n \rangle = \int |E_n|^2 dz$.

Most of the time people are interested in knowing how much percentage (r_p) of power settled down to the n^{th} mode from the incident power, instead of modal coefficient a_n for the field. To get the power percentage, both the in and out power can be written as

$$p_{out} = \frac{1}{2\eta} |a_n|^2 \langle E_n, E_n \rangle \ , \tag{2.10}$$

$$p_{in} = \frac{\beta}{2\omega\mu_0} \langle E, E \rangle = \frac{1}{2\eta} \langle E, E \rangle \ . \tag{2.11}$$

Substituting Equation 2.9 in 2.10, the power ratio r_p expressed using MOI is

$$r_p = \frac{p_{out}}{p_{in}} = \frac{\left|\langle E, E_n \rangle\right|^2}{\langle E_n, E_n \rangle \bullet \langle E, E \rangle} \quad . \tag{2.12}$$

Second, let's derive the power ratio r_p expressed with field $E_{x0}(z)$ at position $\mathrm{x} = \mathrm{x}_0$ (an arbitrary position). Shown in Figure 2.6, along the propagation x direction, if no any other loss mechanism is introduced, the input field $E(z)$ will settle down to the mode $E_n(z)$, the waveguide supported mode, with amplitude a_n. This process is a leaking process and the field will gradually shed all the other modes included in it except the waveguide supported mode. The power ratio r_p included in the field for the waveguide supported mode shouldn't change whether it is measured at $x = 0$ or some other position.

In analogy with Equation 2.1 and 2.9, the field $E_{x0}(z)$ and its modal coefficient b_n for the n^{th} mode can be written as

$$E_{x0}(z) = \sum_m b_m E_m(z) \quad , \tag{2.13}$$

$$b_n = \langle E_{x0}, E_n \rangle \big/ \langle E_n, E_n \rangle \quad . \tag{2.14}$$

In analogy with Equation 2.10, the output power should be

$$p_{out} = \frac{\beta}{2\omega\mu_0} \left|b_n\right|^2 \langle E_n, E_n \rangle \quad . \tag{2.15}$$

Substituting Equation 2.14 in 2.15, Equation 2.15 will become

$$p_{out} = \frac{\beta}{2\omega\mu_0} \bullet \frac{\left|\left\langle E_{x0}, E_n \right\rangle\right|^2}{\left\langle E_n, E_n \right\rangle} \quad . \tag{2.16}$$

Now the power ratio r_p between output and input (at $x=0$) is calculated by dividing Equation 2.16 by Equation 2.11 as

$$r_p = \frac{p_{out}}{p_{in}} = \frac{\left|\left\langle E_{x0}, E_n \right\rangle\right|^2}{\left\langle E_n, E_n \right\rangle \bullet \left\langle E, E \right\rangle} \quad . \tag{2.17}$$

Equation 2.17 expresses the power ratio using field $E_{x0}(z)$ at $\mathrm{x} = \mathrm{x}_0$, while Equation 2.12 uses field $E(z)$ at $\mathrm{x} = \mathrm{x}_0$. Equation 2.17 and 2.12 has the same denominator, and the only difference is in the numerator MOI term. Theoretically, the power ratio calculated using Equation 2.17 should be the same as using Equation 2.12 for situations without loss mechanism introduced from $x=0$ to $\mathrm{x} = \mathrm{x}_0$. The modal coefficient b_n should be equal to a_n; however, b_n would be less than a_n if there is loss introduced between them. Then this power ratio calculated using Equation 2.17 will express a measurement of the power loss. This is the basis for using MOI to calculate bend efficiency for waveguide bends.

(2) Bend efficiency calculation using MOI method

In this dissertation, all waveguides are single-mode and the source for the input waveguide in the FDTD simulation is the fundamental mode of the waveguide. For bend structures, output waveguides are assumed to be the same as input ones. Therefore, for a perfect bend, this mode should get reflected at 100%, both in amplitude and phase, and the BE would be 1. However, a perfect bend is never a reality; after the bend, the waveguide mode will get distorted and become an arbitrary field. This field would shed off some power and gradually settle down to the output waveguide mode but with a modal coefficient less than 1. This is a case with loss introduced between the input and output.

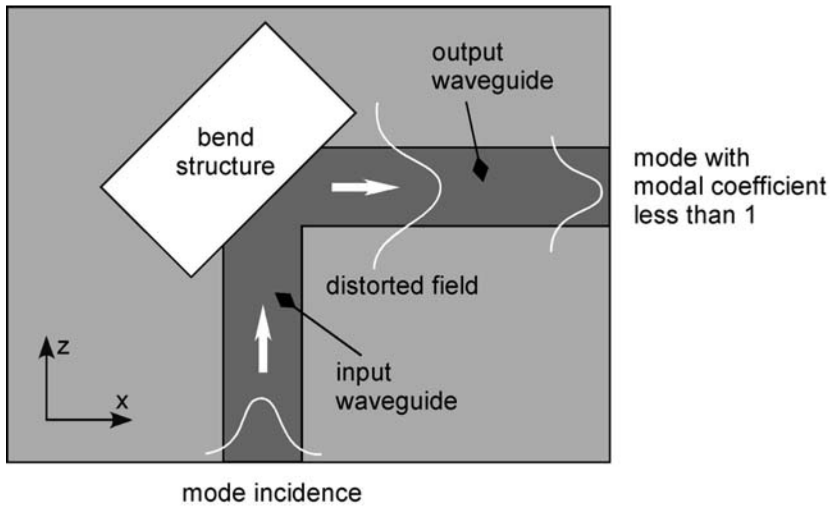

Figure 2.7 Illustration of BE calculation using MOI

When calculating bend efficiency (BE) using the MOI method, as shown in Figure 2.7, a position should be chosen at the output waveguide side to do the MOI. Theoretically as explained before, along the output waveguide, choosing where to do the MOI should not make the result different. This situation is similar to calculating the power ratio at some propagation distance $x = x_0$ with Equation 2.17.

A special extension here to Equation 2.17 is that the incident field E is the supported fundamental mode, which is the same as the output waveguide mode, E_n, here, using E_0 representing the fundamental mode. Thus, Equation 2.17 can be written as

$$BE = \frac{p_{out}}{p_{in}} = \frac{\left|\left\langle E_{x0}, E_0 \right\rangle\right|^2}{\left|\left\langle E_0, E_0 \right\rangle\right|^2} \ . \tag{2.18}$$

The BE calculated by Equation 2.18 uses field information, and a special note is that both field E_0 and E_{x0} are complex, which means both amplitude and phase should be included. The actual form of E_0 and E_{x0} should be $E_0 e^{j\varphi_0}$ and $E_{x0}(z)e^{j\varphi(z)}$, while φ_0 is a constant for the fundamental mode incidence, and both $E_{x0}(z)$ and $\varphi(z)$ can be variables of z coordinate as in Figure 2.7. Considering the complex characteristics for both fields as in Equation 2.18, a more explicit expansion for Equation 2.18 can be done as follows. First,

$$\int E_{x0} e^{j\varphi} \bullet E_0 e^{-j\varphi_0} dz = e^{-i\varphi_0} \int E_{x0} E_0 e^{j\varphi} dz \ , \tag{2.19}$$

knowing $e^{j\varphi} = \cos\varphi + j\sin\varphi$, Equation 2.19 can be separated to two terms as

$$e^{-i\varphi_0} \int E_{x0} E_0 e^{j\varphi} dz = e^{-j\varphi_0} \left(\int (E_{x0} E_0 \cos\varphi) dz + j \int (E_{x0} E_0 \sin\varphi) dz \right) \ . \tag{2.20}$$

Taking the absolute value and then squaring for both sides of Equation 2.20 gives

$$\left| \int E_{x0} E_0 e^{j\varphi} dz \right|^2 = \left| \int E_{x0} E_0 \cos\varphi dz \right|^2 + \left| \int E_{x0} E_0 \sin\varphi dz \right|^2 \ . \tag{2.21}$$

Thus the BE as in Equation 2.18 can be expanded as

$$BE = \frac{p_{out}}{p_{in}} = \frac{\left|\left\langle E_{x0}, E_0 \right\rangle\right|^2}{\left|\left\langle E_0, E_0 \right\rangle\right|^2} = \frac{\left| \int E_{x0} E_0 \cos\varphi dz \right|^2 + \left| \int E_{x0} E_0 \sin\varphi dz \right|^2}{\left| \int \left(E_0 e^{j\varphi_0}\right) \bullet \left(E_0 e^{-j\varphi_0}\right) dz \right|^2} \ . \tag{2.22}$$

In this dissertation, Equation 2.22 will be applied to FDTD numerical calculation, thus all the integrals would change to summations, that is,

$$BE = \frac{\left(\sum E_{x0} E_0 \cos\varphi\right)^2 + \left(\sum E_{x0} E_0 \sin\varphi\right)^2}{\left(\sum |E_0|^2\right)^2} \quad . \tag{2.23}$$

When calculating BE for FDTD simulations using Equation 2.23, the amplitude and phase of the fields can be directly derived from the FDTD outputs. The summation in Equation 2.23 is taken along a monitor line which needs to be long enough to cover 100% of the power and is in a normal direction of and centering at the input or output waveguide. Equation 2.23 is the expression used in this dissertation to calculate the bend efficiency for most cases if no special declaration.

At some cases, a simple power ratio expressed as in Equation 2.24 is used,

$$BE = r_p = \frac{P_{out}}{P_{in}} = \frac{\sum\limits_{x=x_0} p_{zz}}{\sum\limits_{z=0} p_{xx}} \ , \tag{2.24}$$

where p_{xx}, p_{zz} stands for the power distribution along x or z direction, which are direct outputs from our 2D-FDTD tool. The summation is taken along a power monitor line as shown in Figure .2.8.

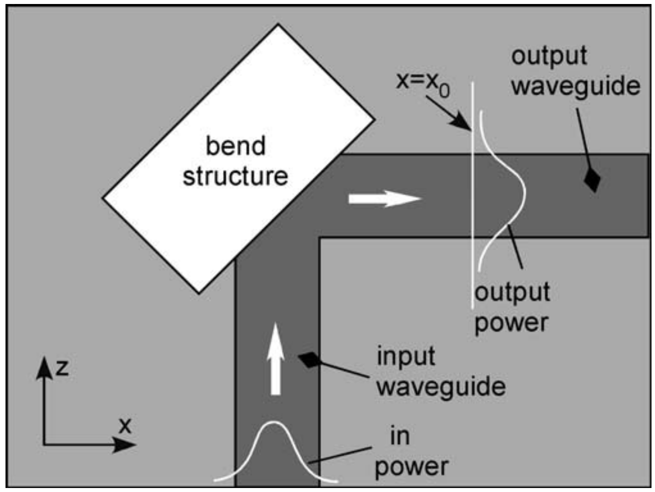

Figure 2.8 Illustration of BE calculation by power ratio

In Equation 2.24, the incident power P_{in} is taken at the very beginning of the input waveguide while the output power P_{out} is taken at some position $x = x_0$ along the output waveguide. Without MOI, bend efficiency calculated by Equation 2.24 varies along the output waveguide, especially at close to bend area. Generally it decreases for increasing x positions along the output waveguide. The reason is the leaking process for the nonmode part. However, at positions far away from the bend, this number will stand for the power left for the mode and it will match the result using MOI. At close to bend area, the number calculated using Equation 2.24 is generally bigger than using Equation 2.23. Using Equation 2.24 requires simulating a long output waveguide to get the power ratio for the mode, which puts high demand for the computer and takes longer time. However, initially some of our results use this method and also there is limitation by our FDTD code, some of the results in this dissertation still use this method. However, this will be declared clearly as “by power ratio” when applied to distinguish from “MOI” method as Equation 2.23.

2.3.3 3D-to-2D waveguide transformation using effective index method

Actual waveguides have 3D configurations; however, most waveguide component designs start from simple 2D models. This will involve one important process, transferring a 3D waveguide to an equivalent 2D slab waveguide. The effective index method (EIM) is one of the effective approximation methods, especially for 3D ridge waveguides.

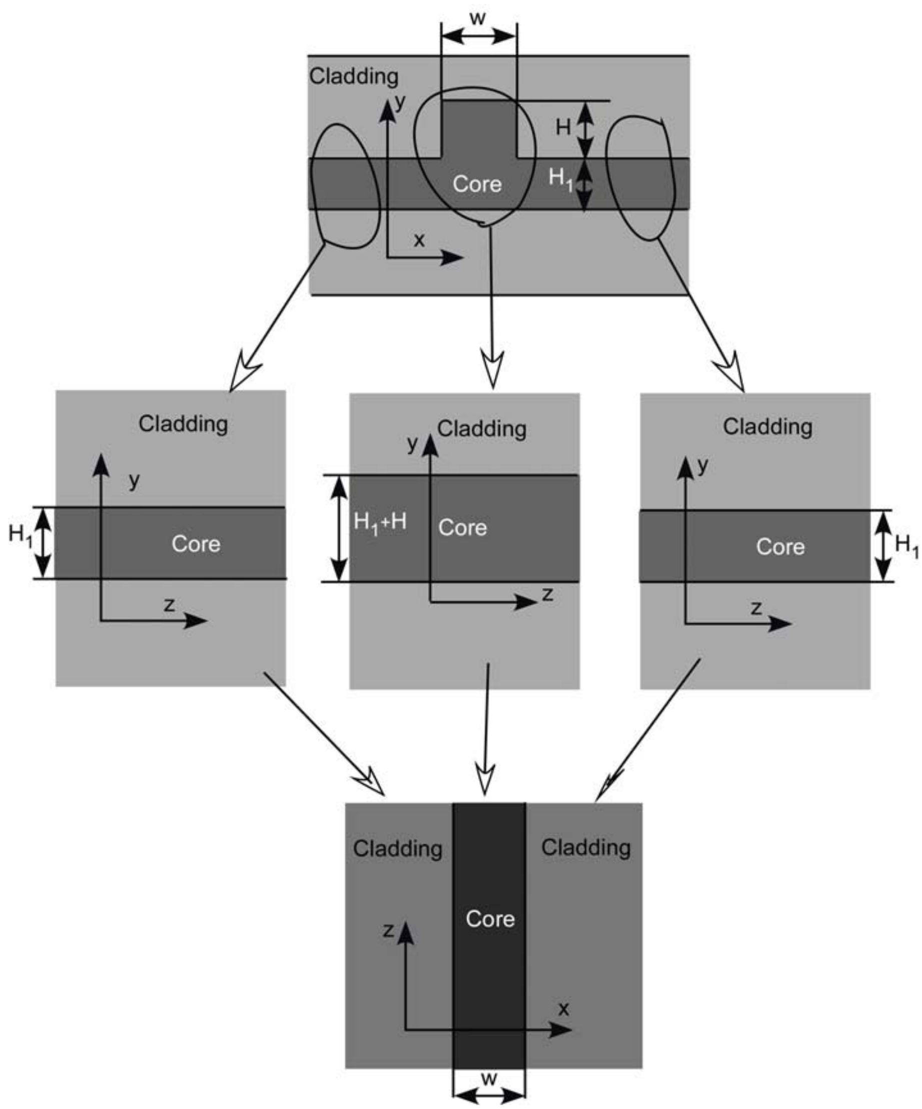

Figure 2.9 3D-to-2D transformation using Effective Index Method

The procedure of transforming a ridge 3D waveguide to an equivalent 2D slab waveguide by the effective index method is shown in Figure 2.9. The basic concept is collapsing the y geometry by two steps. First the 3D cross-section has been transformed to three 2D slab waveguides in which x is looked as homogeneous. Then the three effective indexes analytically calculated from these three 2D waveguides are taken and used as core and cladding indices for the final 2D waveguide in which y can be taken as homogeneous.

Special attention should be paid to the polarization. For example, for a TE-like 3D mode with H_y and E_x dominated, the electric field is polarized in the x direction. This polarization is TE for the three intermediate 2D waveguides, while it is TM for the final 2D waveguide. Contrarily, the other polarization, TM-like 3D mode with E_y and H_x dominated, will become TE for the final 2D waveguide.

However, for convenience, this dissertation calls TM-like polarization in a 3D case as TM for a 2D cases, which refers to the electric field polarized in the y direction; TE for both 3D and 2D cases will refer to the electric field polarized in the x direction.

The following is an example to show how to do the transformation using EIM. The waveguide used here is called Gyro waveguide for convenience because it is specially used for a Gyro project, and details about the Gyro project and designing a Gyro waveguide depolarizer are given in Chapter 6.

Table 2.2 Gyro material system

Material	**TE-like (E^x) (in plane)**	**TM-like (E^y) (out of plane)**
PI2525 (core for 3D)	1.656	1.640
NOA 71 (cladding for 3D)	1.548	1.547
Index contrast Δ	7.0%	6.0%

Table 2.2 shows the measured refractive indices for the Gyro waveguide material and it shows big birefringence.

It is required that this waveguide works at single-mode condition at $\lambda_0 = 1.33$ μm and has a 3D ridge cross-section shape. The waveguide design is accomplished by Jaime Cardenas using *Fimmwave* [57], and the 3D cross-section geometry has come up as Figure 2.10 with W=3.5μm, H=0.7 μm, H_1=2.3 μm.

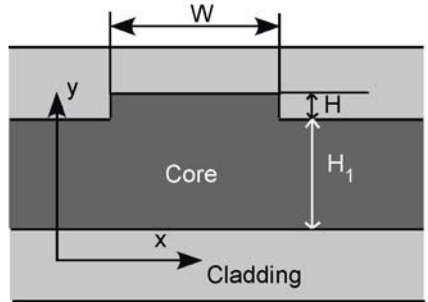

Figure 2.10 A 3D cross-section of the Gyro waveguide

The final transformed 2D slab waveguide using EIM has width 3.5 μm and refractive indexes shown in Table 2.3. It is seen that the index contrast has dramatically dropped to about 0.3% for both TM and TE light. The validity of this transformation by EIM can be evaluated by comparing the final effective index calculated for this final 2D slab waveguide and a direct 3D simulation for the 3D waveguide using *Fimmwave* software. From the numbers in the last two rows of Table 2.3, the effective index calculated from these two approaches matches extremely well.

Table 2.3 Properties of the transformed 2D Gyro waveguide

<table>
<tr><th colspan="2">Final 2D slab waveguide</th><th>TE-like (E_x) (in plane)</th><th>TM-like (E_y) (out of plane)</th></tr>
<tr><td colspan="2">Core</td><td>1.6464</td><td>1.6302</td></tr>
<tr><td colspan="2">Cladding</td><td>1.6414</td><td>1.6251</td></tr>
<tr><td colspan="2">Index contrast Δ</td><td>0.3%</td><td>0.31%</td></tr>
<tr><td rowspan="2">Final effective index</td><td>Effective index method</td><td>1.6438</td><td>1.6276</td></tr>
<tr><td>Direct 3D simulation</td><td>1.6435</td><td>1.6273</td></tr>
</table>

CHAPTER 3

SINGLE AIR-INTERFACE WAVEGUIDE BENDS

Section 2.2 of Chapter 2 has given an overall view of the waveguide bend structures available from the literature, and the approaches mostly focus on high-index waveguides. Most people accept that it is hard to bend low-index and low-Δ waveguides in a compact form. Traditional circular bends require big radius to achieve low loss for low-index and low-Δ waveguides. The photonic crystal approach is investigated by another graduate student in our group. The phase compensation method can only give a mild bend in several degrees and is not applicable for an efficient sharp bend.

The single-interface trench mirror approach has been suggested for low-index and low-Δ waveguides, such as silica-based waveguides [40,41]. People have actually fabricated these bends with different bend angles. The reflectivity has been calculated based on waveguide-mode plane-wave expansion (PWE) theory and compared with the experimental results. The loss mechanism has been attributed to the Goos-Hanchen (G-H) shift and the diffraction effect besides some fabrication factors, such as surface roughness and verticality. However, that explanation is not complete and not necessarily true at some cases.

In this chapter, one single air-interface 90° waveguide bend for a specific low-index and low-Δ waveguide has been first simulated using rigorous FDTD method. It turns out that the bend efficiency is not high even with compensation of the G-H shift. Quantitative explanation and calculation about the loss has been given based on waveguide-mode plane-wave expansion (PWE) theory. The loss comes from some transmission from the waveguide mode nature, and it is not the diffraction effect as explained by other papers.

Following the FDTD simulation of single air-interface 90° waveguide bend and waveguide PWE theory, several ways of achieving high-efficiency bends have been proposed and designed based on taking a panoramic view of the angular spectrum of the waveguide mode. The high-efficiency waveguide bends all have a single air-interface mirror configuration and are designed for low-index and low-Δ waveguides.

Finally to verify the way we understand the PWE theory and to get fabricated waveguide bends on polymer waveguides, a set of single air-interface waveguide bends has been designed and fabricated. To the best of our knowledge, it is at first time that single-interface air-trench bends are fabricated on polymer waveguides.

3.1 Single air-interface 90º bends

A single air-interface trench has been successfully etched for different materials from several groups as stated in Section 2.2. In this section, this single air-interface trench mirror will be applied to a low-index and low-Δ waveguide with its core and cladding refractive indices of 1.5 and 1.465 and width 2 μm to support its only fundamental mode at λ_0=1.55 μm.

Figure 3.1(a) is a schematic illustration for this single air-interface 90° bend and Figure 3.1(b) is a plane-wave approximation of Figure 3.1(a). The approximation replaces the waveguide with an infinite medium with refractive index n=1.485, which is the effective index of the waveguide. Then for a plane wave incidence from a medium n=1.485 to the air medium, it has an incident angle 45° that is greater than the critical angle θ_c=42.3°, thus total internal reflection (TIR) should be expected based on the approximation model.

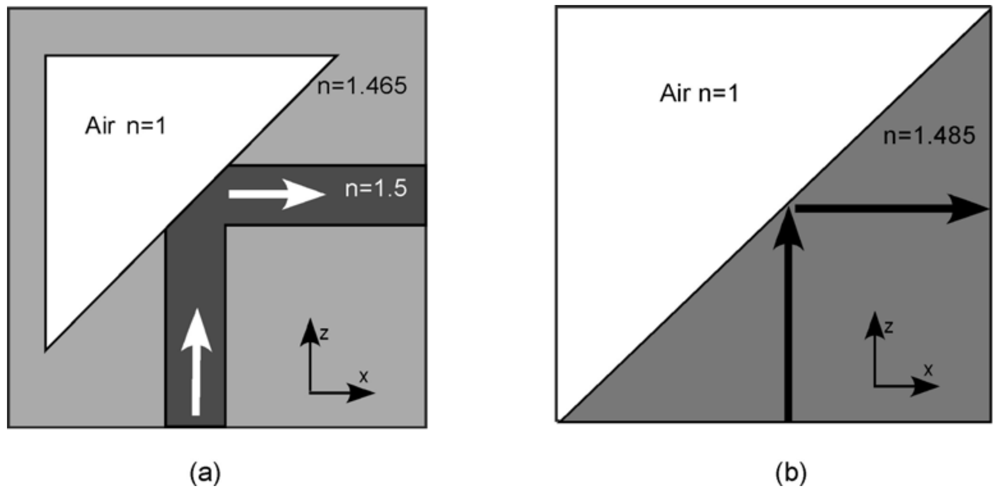

Figure 3.1 Air-trench mirror approach for a 90^o waveguide bend
(a) actual model (b) approximate model

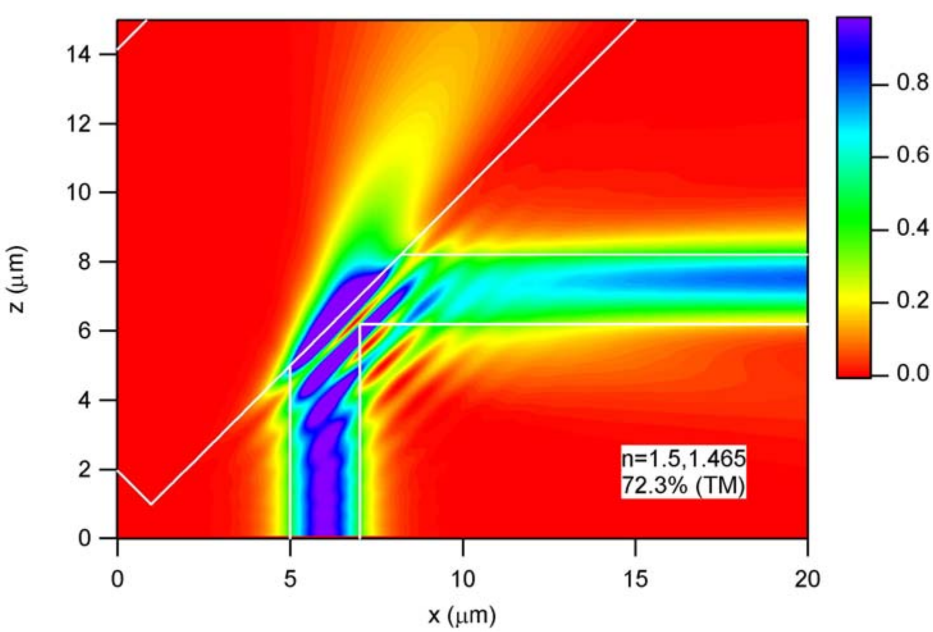

Figure 3.2 FDTD simulation of a 90^o waveguide bend (TM)

Figure 3.2 shows an image plot of the squared magnitude of time averaged electric field (this applies to all the FDTD figures in this dissertation). The simulation size is 20 μm ×15 μm, FDTD grid size is $\lambda_0/80$ at wavelength λ_0=1.55μm, and the incident source is the waveguide fundamental TM mode. The 45° slanted line is the air and waveguide interface, and at its top and left side is the air zone which is input in FDTD input file as an slanted air rectangular shape. For an efficient simulation area, a small part of the rectangular has been truncated. However, this will not affect the simulation result because of the PML boundary. Figure 3.2 has been designed to compensate the Goos-Hanchen shift with an optimal position of output waveguide for TM light. The bend efficiency is 72.3% (by MOI) or 78.4% (by power ratio). Notice that most of the light is reflected by the air interface into the output waveguide but obviously some of the light is transmitted through the air interface and lost.

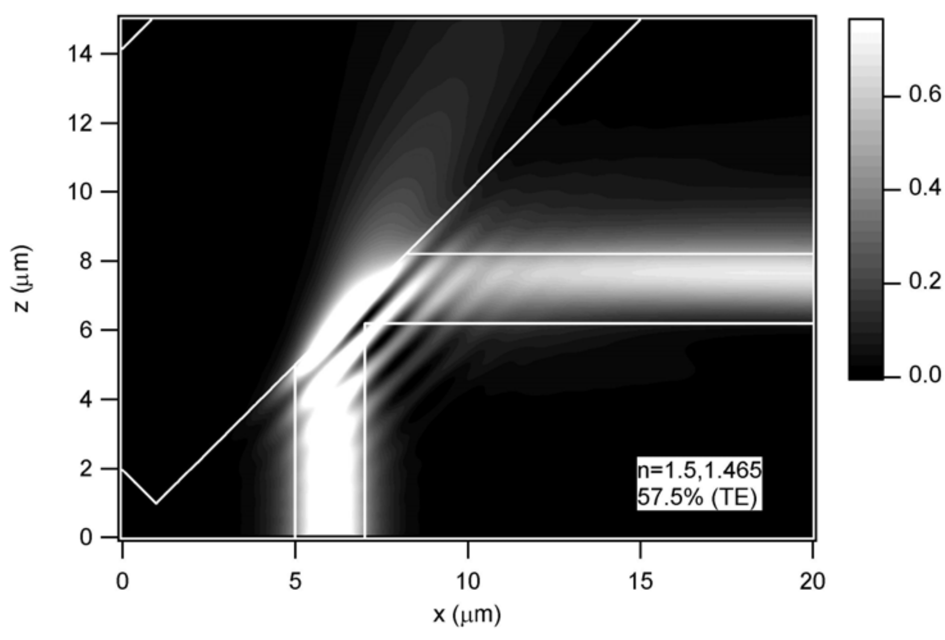

Figure 3.3 FDTD simulation of a 90° waveguide bend (TE)

Figure 3.3 is the same configuration as in Figure 3.2 with TE mode as an incident source. It is seen that more light transmits through the waveguide-air interface, and bend efficiency is even lower, 57.5% (by MOI) or 67.8% (by power ratio). Compared with Figure 3.2 using TM source, the reflected light in Figure 3.3 has shifted up slightly in the output waveguide, which is the signature of different Goos-Hanchen shifts for TM and TE light.

The FDTD simulation of both Figure 3.2 and 3.3 shows that total internal reflection did not occur at the air interface as the plane-wave approximation (Figure 3.1(b)) expects. What does happen at the air-waveguide interface which makes bend efficiency only 72.3% and 57.5% for TM and TE light? The following section will address this in detail based on waveguide-mode plane-wave expansion theory.

3.2 Waveguide mode plane wave expansion theory

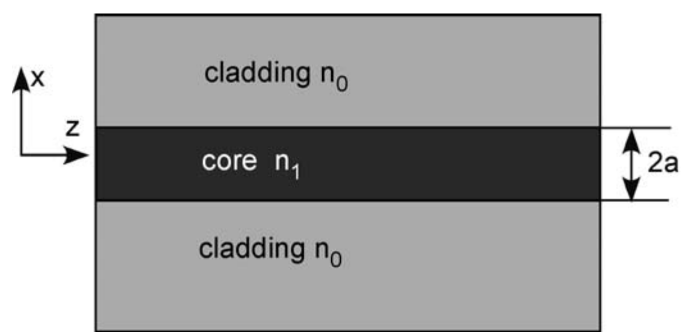

Figure 3.4 A symmetrical 2D slab waveguide

Figure 3.4 shows a symmetrical 2D slab waveguide with width $2a$ and core and cladding indexes of n_1 and n_0. Solving Maxwell's equations and satisfying the waveguide boundary conditions, the analytical waveguide mode has the well-known cosine-exponential electric field distribution solution [70] expressed for TM light as

$$E(x) = \begin{cases} A\cos(\kappa a)e^{-\sigma(x-a)} & x \rangle a \\ A\cos(\kappa x) & |x| \le a \\ A\cos(\kappa a)e^{\sigma(x+a)} & x \langle -a \end{cases} , \tag{3.1}$$

where κ and σ are wavenumbers along x-axis. They have a relationship with β, the propagation constant relative to the guided mode, and k_0, the wavevector in vacuum, as

$$\begin{aligned} \kappa^2 + \beta^2 &= k_0{}^2 n_1{}^2 \\ \sigma^2 + \beta^2 &= k_0{}^2 n_0{}^2 \end{aligned} . \tag{3.2}$$

The two quantities β and k_0 are related as $\beta = k_0 / n_{eff}$, where n_{eff} represents the effective index of a waveguide.

Based on the waveguide mode plane-wave expansion (PWE) theory [67], the waveguide mode field can be considered as a superposition of plane waves propagating in their equivalent infinite mediums with different refractive index n for each plane wave. The mode field $E(x)$ and its spatial spectral amplitude $E(k_x)$ are a Fourier transform pair given as

$$E(x) = \frac{1}{\sqrt{2\pi}} \int_{-\infty}^{+\infty} E(k_x) e^{jk_x x} dk_x \ , \tag{3.3}$$

and

$$E(k_x) = \frac{1}{\sqrt{2\pi}} \int_{-\infty}^{+\infty} E(x) e^{-jk_x x} dx \ , \tag{3.4}$$

where k_x is the wavevector component along x axis and related to propagation constant β and wavevector k_0 as

$$k_x{}^2 + \beta^2 = n^2 k_0{}^2 \ . \tag{3.5}$$

For the waveguide used in Section 3.1, the propagation constant β is $\beta = k_0 \bullet n_{eff} = \dfrac{2\pi}{1.55} \bullet 1.485 = 6.02 \mu m^{-1}$.

With $k_x = 0$, $\beta = nk_0 = n_{eff} k_0$ from Equation 3.5, this represents the main plane wave propagating in a medium n_{eff} at an incident angle θ_0 relative to the normal of the air-interface, which is identical to the incident angle of the waveguide mode. For the single air-interface 90° bend, $\theta_0 = 45^\circ$.

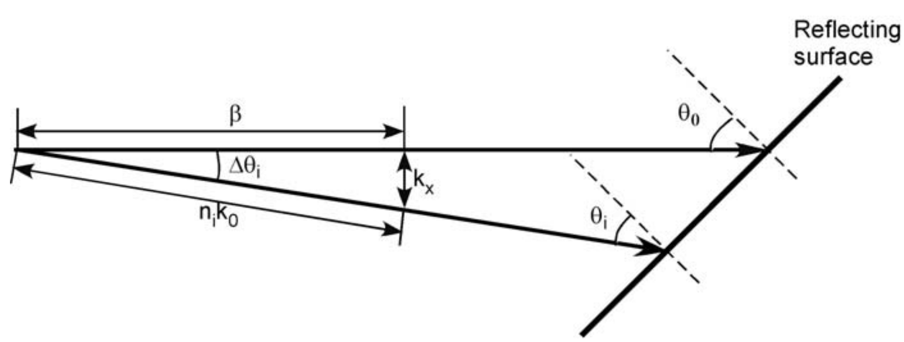

Figure 3.5 Illustration of plane wave expansion theory in Fourier space

For any plane-wave component with $k_{xi} \neq 0$, it will propagate in a medium with refractive index $n_i = \sqrt{(k_x^2 + \beta^2) / k_0}$ at an incident angle θ_i as shown in Figure 3.5. The angle difference $\Delta\theta_i = \theta_i - \theta_0$ can be defined by Equation 3.6 as

$$\tan(\Delta\theta_i) = \frac{k_{xi}}{\beta} \quad . \tag{3.6}$$

Equation 3.6 is very important for understanding the approaches proposed in the following sections. The angle difference $\Delta\theta_i$ can have a sign of plus or minus depending on the sign of k_x.

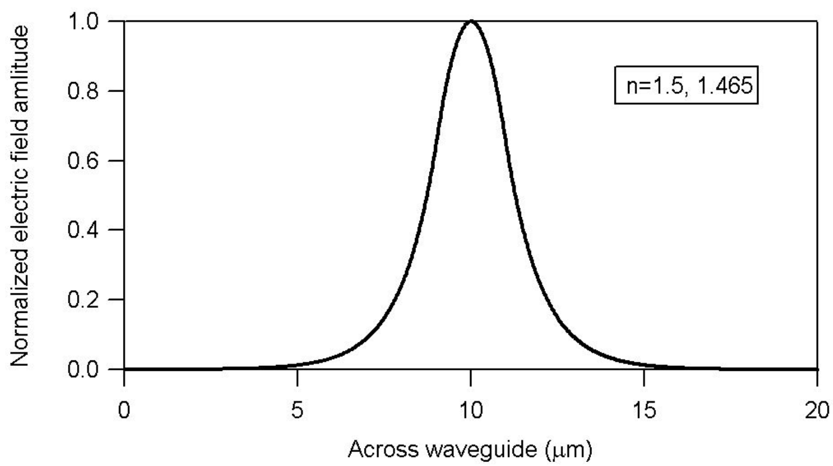

(a)

Figure 3.6 Waveguide (a) mode profile (b) angular spectrum (TM)

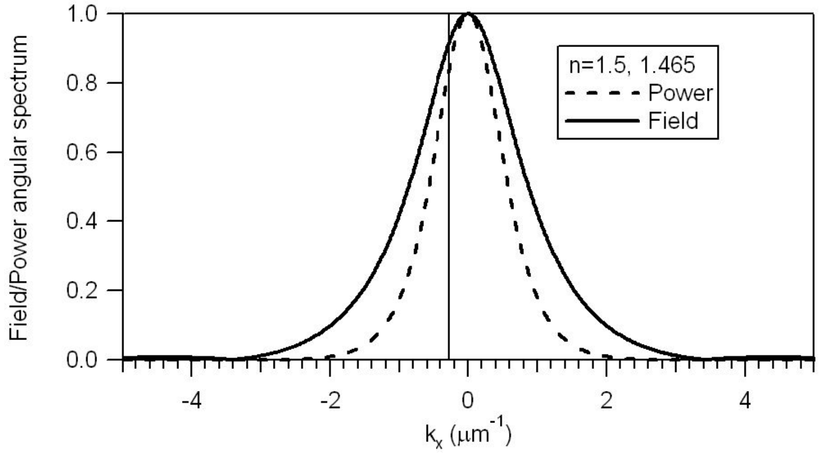

(b)

Figure 3.6 Waveguide (a) mode profile (b) angular spectrum (TM) (cont)

The normalized electric field $E(x)$ and its Fourier transform $E(k_x)$ for the waveguide in Section 3.1 are shown in Figure 3.6(a) and (b). Also appended in Figure 3.6(b) is the square of $E(k_x)$, which reflects the power distribution along k_x, thus called power angular spectrum in this dissertation.

From Figure 3.6(b), it can be seen that most of the power are concentrated within $k_x = \pm 2\ \mu\text{m}^{-1}$, which corresponds to an approximate maximum angle difference $\Delta\theta_{\max} = \pm 18.4^\circ$. Notice that in Figure 3.6(b) there is a line (called critical line) at approximate $k_{xc} = -0.28\ \mu\text{m}^{-1}$, which corresponds to the specific plane wave with a critical incidence 42.3$^\text{o}$. The calculated critical angle difference is $\Delta\theta_c = -2.7^\circ$ from $\theta_0 = 45^\circ$ with $k_x = 0$. Based on the PWE theory as just explained, all the plane-wave components at the right side of the critical line will have incident angles greater than the critical angle, and they will have TIR at the air interface. Those components at the left side will have incident angles less than the critical angle, thus this portion of plane wave components will go through only partial reflection. The light transmitted through the air interface as observed in Figure 3.2 and 3.3 is the transmission part for this portion of light.

The above PWE theory explains very well the propagation of the mode to the mirror, and the mode can be considered as a combination of a continuous spectrum of plane waves propagating at slightly different directions and mediums. Furthermore, this PWE theory can be applied to the analysis and design of mirror-type waveguide bends. When doing so, the reflected field right after reflection at the mirror surface needs first to be derived. The reflected field is a synthetical result from all the reflected plane-wave components, which include both amplitude and phase change from the Fresnel's reflection theory. In general, this reflected field has been distorted as a whole by the mirror interface because some plane waves may have TIR and some may have only partial reflection. This complicated reflection going on at the interface will also bring up phase distortion to the waveguide mode, which is another factor affecting the overall coupling to the output waveguide.

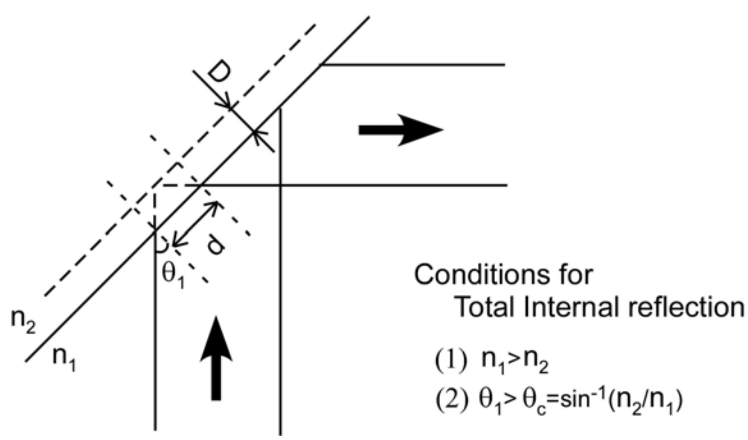

Figure 3.7 Goos-Hanchen shift at total internal reflection

One important phenomenon related is Goos-Hanchen (G-H) shift which occurs when TIR happens at the interface. Physically G-H shift comes from the phase change of electromagnetic field for cases with incident angles greater than critical incidence. This has been observed by other researchers [40,41,67,71] and it has also been observed when designing waveguide bends in this dissertation. Different incident angles and different polarizations will make different Goos-Hanchen shifts, which can be expressed clearly with Figure 3.7 and the following formulas.

Figure 3.7 assumes a finite-sized wave coming to an interface from medium n_1 to n_2, and Goos-Hanchen shift refers to either vertical shift D or lateral shift d, which has expressions for TM (s) and TE light (p) as

$$D_s = \frac{1}{q} \ , \qquad D_p = \frac{1}{qa} = D_s \big/ a \ ,$$

and $$d_s = \frac{2}{q} \tan\theta_1 = 2\tan\theta_1 D_s \ , \qquad d_p = 2\tan\theta_1 \frac{1}{qa} = 2\tan\theta_1 D_p \ ,$$

where q and a are defined as $q = k_i \sqrt{\sin^2\theta_1 - \sin^2\theta_c} = \frac{2\pi}{\lambda_0} n_1 \sqrt{\sin^2\theta_1 - \left(\frac{n_2}{n_1}\right)^2}$,

and $a = \left(\frac{\sin\theta_1}{\sin\theta_c}\right)^2 - \cos^2\theta_1 = \left(\frac{n_1}{n_2}\right)^2 \sin^2\theta_1 - \cos^2\theta_1$.

The following group of figures (Figure 3.8) shows how to get the reflected field at the 90° bend (TM) for the same waveguide as in Section 3.1 based on the waveguide mode plane wave expansion theory as just explained. It should be pointed out again that each plane wave propagates in a slightly different medium with an effective refractive index n_i at a slightly different incident angle θ_i. Thus the reflected field in Fourier domain, $E_R(k_x)$ in k_x space, can be first generated by multiplying $E_0(k_x)$ with the Fresnel's reflection coefficient $r_s(k_x)$, that is,

$$E_R(k_x) = r_s \bullet E_0(k_x) = \frac{\cos\theta_i - \sqrt{\left(\frac{n_i}{n_1}\right)^2 - \sin^2\theta_i}}{\cos\theta_i + \sqrt{\left(\frac{n_i}{n_1}\right)^2 - \sin^2\theta_i}} \bullet E_0(k_x) \ .$$

The incident mode $E_0(k_x)$ has constant phase, assuming zero for Figure 3.8; however, r_s is complex for TIR conditions. As a result, $E_R(k_x)$ can be complex, and its normalized magnitude of angular spectrum and phase are shown in Figure 3.8(a) and (b) relative to the incident mode.

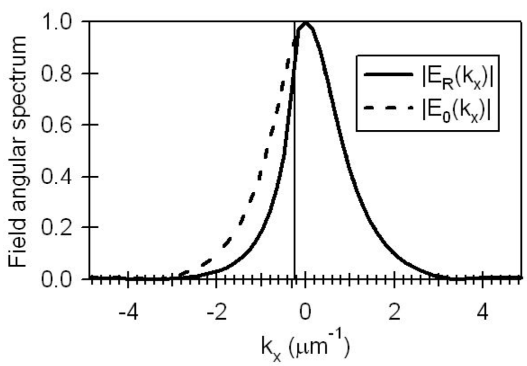

(a) angular spectrum of incident mode and reflected field

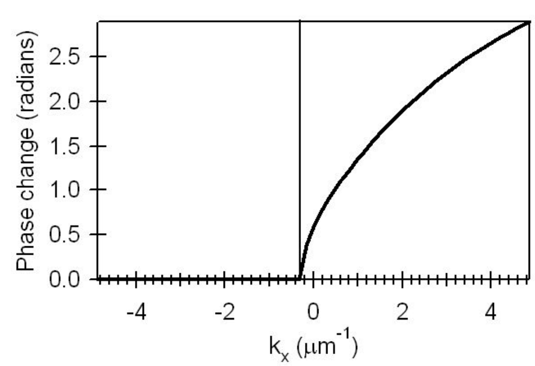

(b) phase change when reflecting for different plane wave components

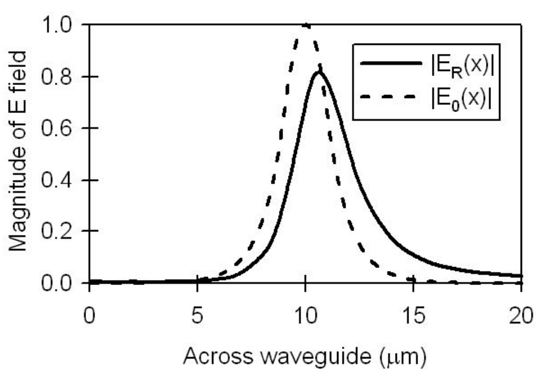

(c) magnitude of reflected field

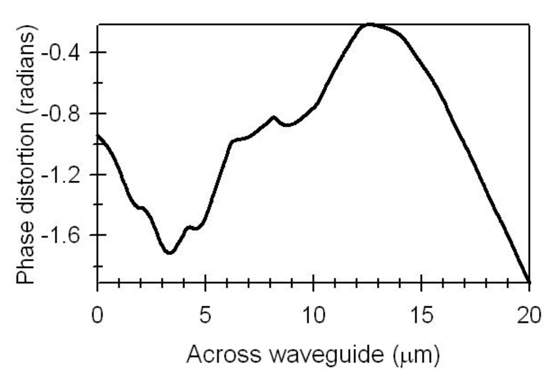

(d) phase distortion of reflected field

Figure 3.8 Generation of the reflected field based on PWE theory

Figure 3.8(a) shows clearly that it is partial reflection for the components at the left side of the critical incidence while TIR for the right-side components. Figure 3.8(b) is actually the phase change of the reflection coefficient r_s, which is also the phase distribution of $E_R(k_x)$ in k_x space.

The reflected field in real space, $E_R(x)$, is then attained by taking an inverse Fourier transform of $E_R(k_x)$. The complex field $E_R(x)$ has its normalized magnitude of amplitude and phasefront shown in Figure 3.8(c) and (d) relative to the incident mode. Two obvious features shown from Figure 3.8(c) are the decreased amplitude and the G-H shift (approximately 0.7 μm). Figure 3.8(d) shows an overall phasefront distortion compared with constant phase for incident mode (not shown).

For TE light incidence, the same procedure as above can be followed but using the following reflection coefficient r_p from Fresnel's equations as

$$r_p = \frac{\cos\theta_i - \dfrac{n_1}{n_i}\sqrt{1-\left(n_1/n_i\right)^2 \sin^2\theta_i}}{\cos\theta_i + \dfrac{n_1}{n_i}\sqrt{1-\left(n_1/n_i\right)^2 \sin^2\theta_i}} .$$

After getting the reflected field $E_R(x)$, the bend efficiency can be analytically calculated using Equation 2.23 with MOI method. However, it is very critical at this point to consider the G-H shift. For optimal waveguide bend designs, the output waveguides have to be placed at a position to compensate the G-H shift to attain maximum reflection, which has been done for the FDTD design and simulation in this dissertation with an optimal preference given to TM light. The calculations of bend efficiency for the 90° bend in Section 3.1 with the same amount of G-H shift as compensated in FDTD designs are 74.8% and 56.7% for TM and TE light, which matches FDTD results, 72.5% and 57.6%, extremely well.

Figure 3.6 (in page 43) is a graphic expression of the waveguide-mode plane-wave expansion theory, which is the core for this chapter and this dissertation. The power angular spectrum in Figure 3.6(b) is crucial, and four points based on Figure 3.6(b) will be used as the basis for designing high-efficiency bends in this and the next chapter. They are (1) the central position of $k_x = 0$ in Figure 3.6 (b) is related to the incident angle θ_0 of the waveguide mode; (2) the spectrum width $\Delta\theta_{\max}$ is related to the waveguide contrast Δ; (3) the critical line position k_{xc} reflects the relative index difference of waveguide material and air, and the angle difference $\Delta\theta_c$ depends on both the incident angle θ_0 and the waveguide material; (4) TIR occurs for components at the right side while partial reflection for the left-side of the critical line.

To improve bend efficiency, one way is to move more plane-wave components to the right side of the critical line, so it will be TIR for the entire waveguide mode, a continuous spectrum of plane-wave components, not just one single plane wave. This concept is equivalent to have $-\Delta\theta_c > \Delta\theta_{\max}$, which is the design rule for high-efficiency bends in this chapter.

3.3 Improving BE by using smaller bend angles

From the FDTD simulation in Section 3.1, for the 2 μm-width waveguide with core and cladding indexes 1.5 and 1.465, a 90° bend has bend efficiency (BE) 72.3% and 57.5% for TM and TE incidence at λ_0=1.55 μm. The BE is not high because of the partial reflection for the plane-wave components at the left side of the critical line based on PWE theory.

From the power angular spectrum in Figure 3.6(b) and Equation 3.6, for the same waveguide, one way to have more plane-wave components at the right side of the critical line is to increase the mode's incident angle θ_0. By doing so, the $\Delta\theta_c$ gets increased, thus the critical line will move to the left. More plane-wave components at the right side of the critical line means that more components will have TIR, and further means that the overall BE will improve.

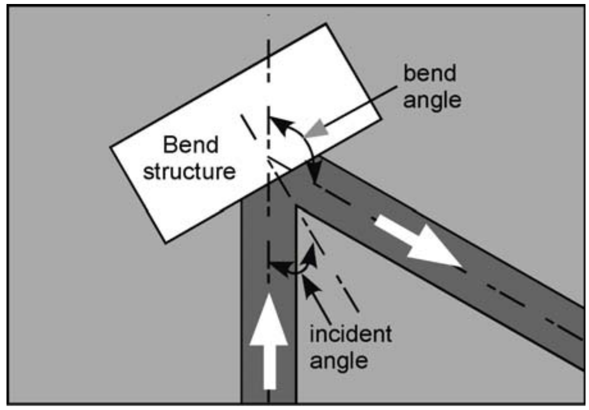

Figure 3.9 Definition of bend angle

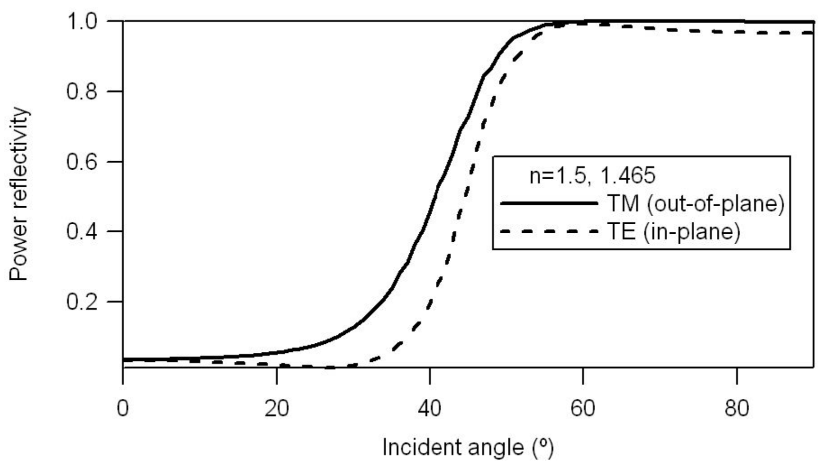

Figure 3.10 Power reflectivity calculated by plane wave expansion theory

Increasing incident angle is the same as decreasing bend angle as the definition shown in Figure 3.9. The power reflectivity (or Bend Efficiency) can be calculated analytically using MOI method as explained in Section 3.2. Shown in Figure 3.10 is BE as a function of incident angle for the same waveguide as in Section 3.1. It is seen that in Figure 3.10 the analytical expectance from PWE would be close to 100% for both TM and TE when the incident angle is increased to 60° (corresponding to a bend angle 60°).

To evaluate the analytical calculations by rigorous FDTD simulations, a set of waveguide bends with bend angles of 80°, 60°, and 45° (corresponding incident angles 50°, 60°, 67.5°) is designed and simulated for the same waveguide at same wavelength 1.55 μm and for both TM and TE polarizations.

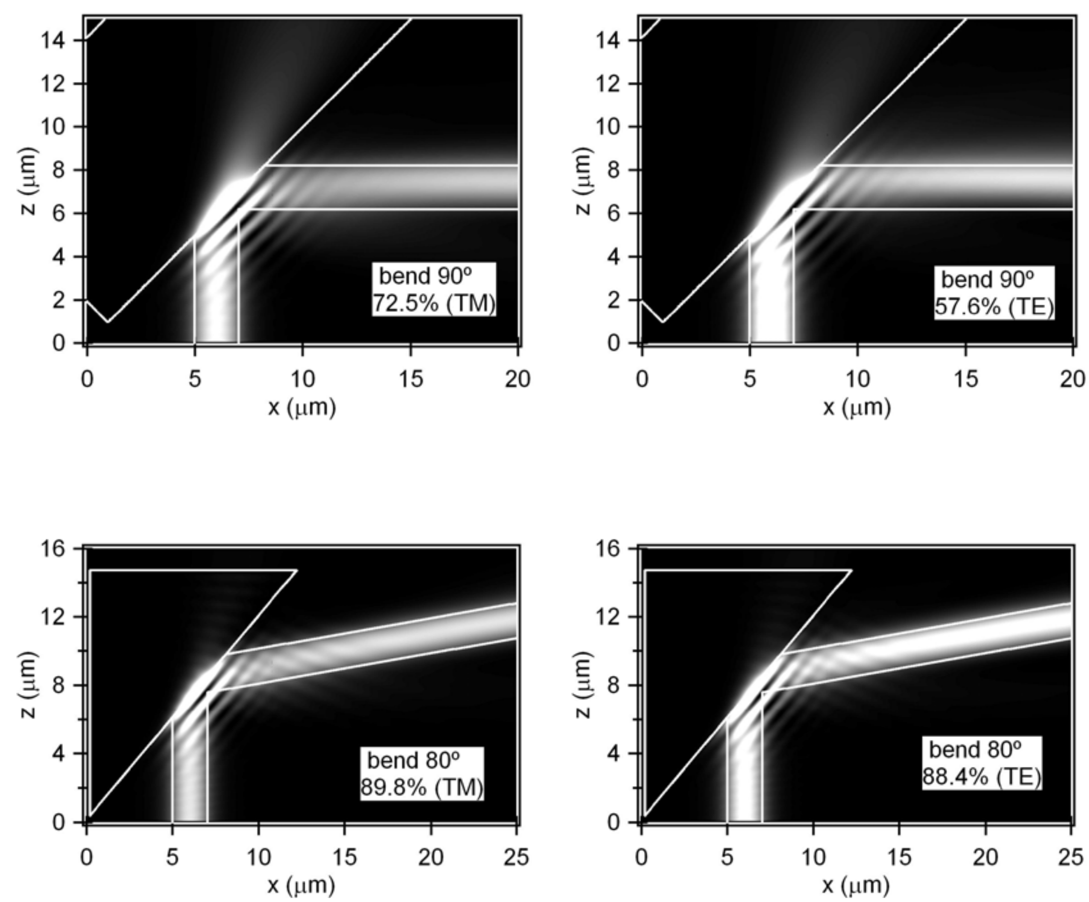

Figure 3.11 FDTD simulation for waveguide 90°, 80°, 60°, 45° bends

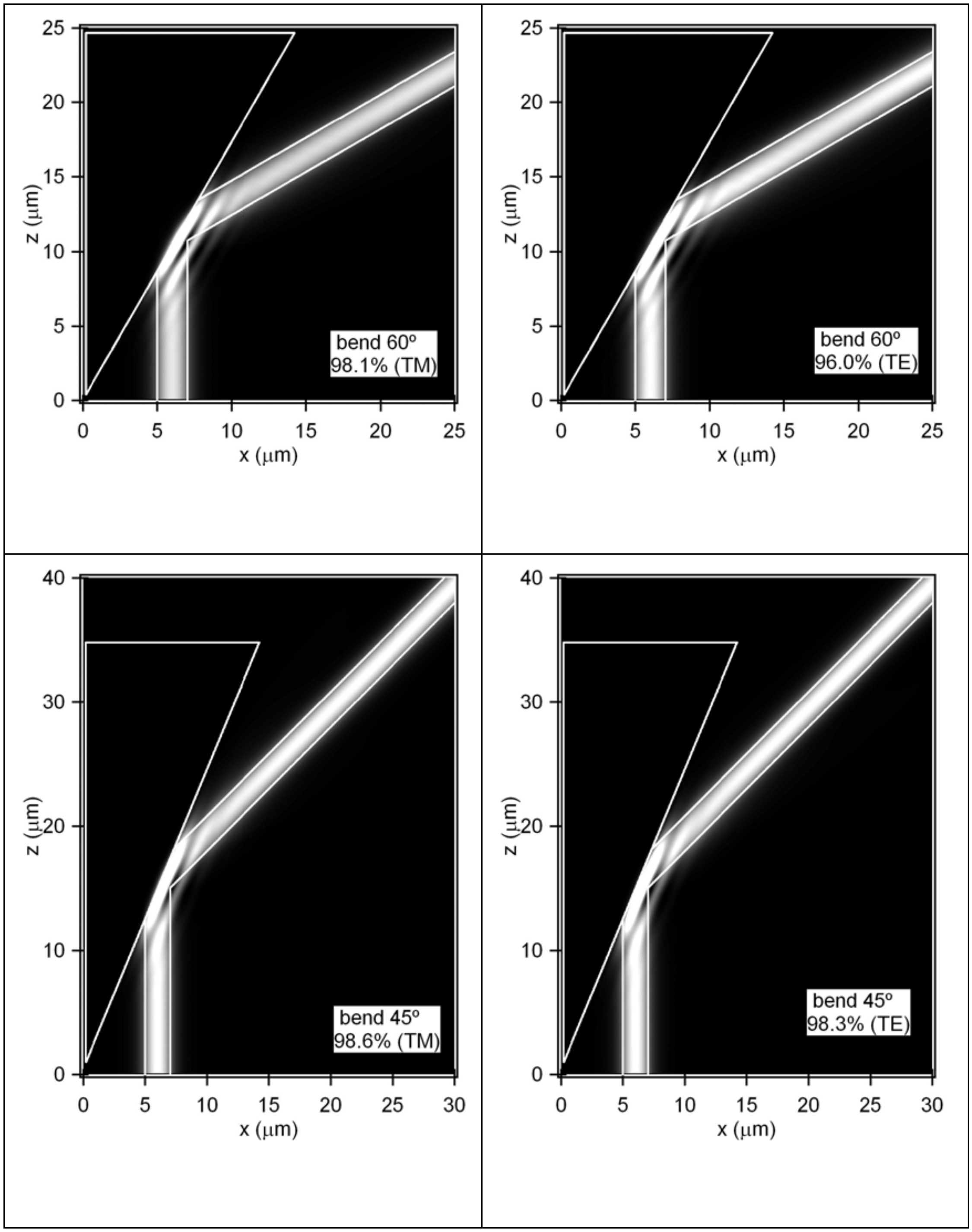

Figure 3.11 FDTD simulation for waveguide 90°, 80°, 60°, 45° bends (cont)

Figure 3.11 are the FDTD simulations with FDTD grid size $\lambda_0/60$. Notice that the simulation size is different for different bend cases, and smaller-bend angles require bigger simulation size to give space to put a power monitor in the normal direction of the output waveguide. The width of the power monitor for all the figures is 10 μm to account for 100% of the incident power. Big simulation size will require big computer memory. Limited by our computer capacity for the big-size 45° bend, the highest the resolution can be is $\lambda_0/60$. To keep the uniformity for all these waveguide bend structures, this set of waveguide bends all uses $\lambda_0/60$ resolution. The 90° bend has been simulated again with $\lambda_0/60$ instead of $\lambda_0/80$ as in Section 3.1, and it can be seen that the simulation results from different FDTD resolution for the 90° bend are essentially the same.

As mentioned before, the waveguide bend designs for an optimal output waveguide position have given preference to TM illumination. Therefore it can be seen that the field in the right column (TE) is a little more offset from the center of the output waveguide compared with its left partner due to different G-H shift for TM and TE polarizations. Attention should be paid to the dimensions for different figures, and they are in scale for the x and z dimensions for each figure itself, but not in the whole group.

In Figure 3.11, for the bends of 80°, 60°, and 45°, the air zone has been input as a triangular shape with the slanted surface tiling at different angles as the working reflecting surface. The 90° bend, however, uses a slanted air rectangular shape. This is because that the top straight surface for a triangular shape will reflect some transmitted light from the slanted surface back to the waveguide side, and this reflected light will interfere with the light going to the output waveguide. This is more severe for the 90° bend than other bend angles because of its low reflectance at the first air interface. A triangular shape has been used before for the 90° bend and severe interference has been observed, thus a rectangular shape for the air zone has been used instead to remove the reflection from the top surface to the output waveguide side. This does not affect the overall performance of the 90° bend.

Table 3.1 BE from FDTD simulation and PWE theory for different bends

Bend angles		90°	80°	60°	45°
Incident angle θ_0 corresponding to k_x=0		45°	50°	60°	67.5°
k_x value corresponding to critical angle 42.3°		-0.28	-0.81	-1.92	-2.83
Bend efficiency	**Theory (TM)**	74.8%	94.6%	99.9%	99.8%
	FDTD (TM)	72.5%	89.8%	98.1%	98.6%
	Theory (TE)	56.7%	88.1%	99.2%	99.3%
	FDTD (TE)	57.6%	88.4%	96.0%	98.3%

Table 3.1 shows the BE calculations from the rigorous FDTD simulations and PWE theory. It is seen that they match extremely well. Note that the BE calculations from both FDTD and PWE theory have considered and compensated the G-H shift, and both use the MOI method.

The relationship of power reflectivity as a function of incident angles (or bend angles) has been roughly observed and reported [40,41]. However, the authors explain the loss mechanism mainly from the Goos-Hanchen (G-H) shift effect, which is true for the cases having most of the plane-wave components at the right side of the critical line, such as 60° and 45° bends. For the 90° and 80° bends, even if considering the G-H shift and having optimal output waveguide positions, the loss is still there. The explanation for the loss in this dissertation is based on the plane wave expansion theory, and the loss is due to the transmission for those plane-wave components at the left side of the critical line.

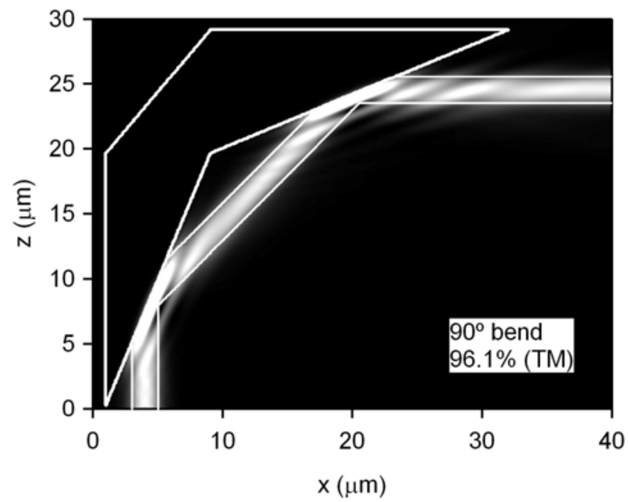

(a) TM light

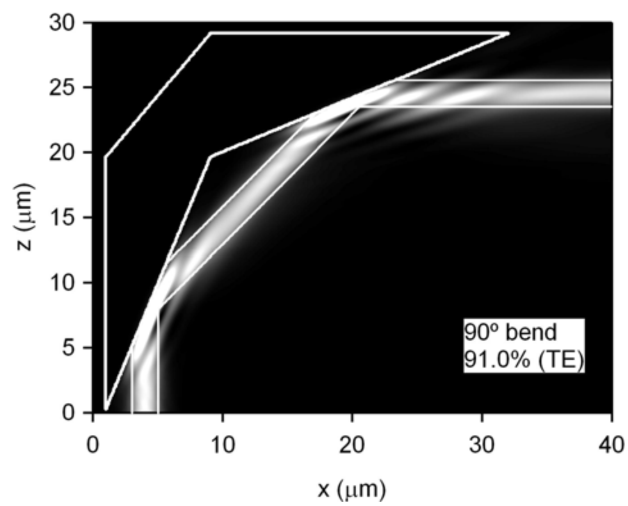

(b) TE light

Figure 3.12 FDTD simulation of a composed 90° bend with two 45° bends

Comparing 90° and 45° bends from Table 3.1, the bend efficiency has been improved from 72.5% and 57.6% to more than 98% for TM and TE light. This suggests a new 90° bend configuration with the addition of two 45° bends. Figure 3.12 is the initial FDTD simulation of this composed 90° bend for both TM and TE light. Although this composed 90° bend configuration has a relatively bigger size, its bend performance gets improved considerably. Further improvement may be achieved with an optimal length of the intermediate waveguide because severe interference has been observed at the second bend for smaller intermediate length.

3.4 Improving BE for 90° bends by using lower-Δ waveguides

Using smaller bend angles can improve the bend efficiency significantly, but the bend angle is decreased and so the bend area gets expanded. If it is still wanted for a sharp 90° bend to keep the bend as compact as possible, an alternate approach is proposed here by varying the waveguide material based on Figure 3.6 (b). For low-Δ waveguides, their fields will not be very well confined, but their angular spectrum will be quite concentrated from the properties of Fourier pair. Therefore decreasing the waveguide contrast Δ can shrink the angular spectrum, if the relative position of the critical line can be kept approximately unmoved, then more components will move to the right side of the critical line and the overall BE gets improved. The critical line reflects the index difference between the waveguide material and air, to keep it approximately unmoved means that the waveguide material should be kept basically the same.

To get a quantitative relationship of BE as a function of waveguide index contrast Δ, the following set of 90° waveguide bends has been simulated with the FDTD method. The waveguides have the same cladding n=1.465 but slightly different index contrasts of Δn= 2.4%, 1.5%, 0.75%, 0.45%, 0.25%.

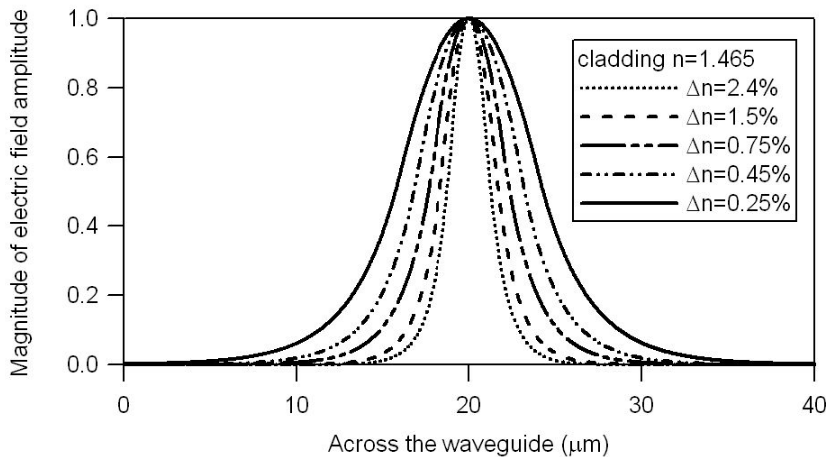

Figure 3.13 Single-mode profiles for waveguides with cladding index n=1.465

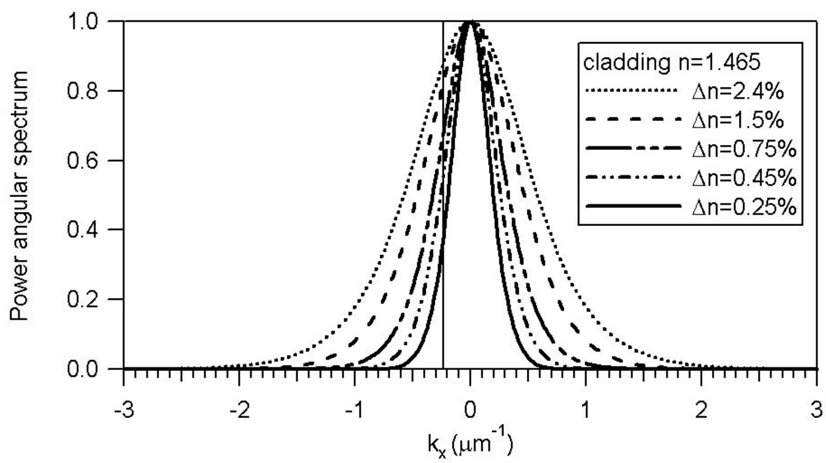

Figure 3.14 Power angular spectrums for waveguides with cladding index n=1.465

Because this set of simulations uses different waveguides and they have different mode profiles and angular spectrum. To see how exactly the angular spectrum gets narrower, the fields and angular spectrums for all these waveguides have been plotted and shown in Figures 3.13 and 3.14. The waveguide width for different Δ waveguides has been chosen properly to support only one single-mode at wavelength λ_0=1.55 μm, and they are 2 μm, 3 μm, 4 μm, 6 μm, and 8 μm respectively for Δn= 2.4%, 1.5%, 0.75%, 0.45%, 0.25%.

It is noticed in Figure 3.13 that the field profile changes from slim to fat in the Δn order from 2.4% to 0.25%, which means the mode gets less confined for lower-Δ waveguide. Their corresponding power angular spectrum in Figure 3.14 shows an opposite shrinking pattern in the order from 2.4% to 0.25%. This conforms to our analysis of the waveguide plane wave expansion theory.

Also drawn in Figure 3.14 is the approximate critical line $k_{xc} = -0.21\mu m^{-1}$ corresponding to roughly $n_{eff} = 1.465$ considering all different waveguides. It can be seen that more components move to the right side of k_{xc} when the power angular spectrum gets narrower. This is just what we expect and the bend efficiency should improve.

Figure 3.15 is a group of FDTD simulations for this set of waveguide 90° bends and in the order from 2.4% to 0.25% with both TM and TE illuminations. The incidence for each case is the analytical mode for the specified waveguide either TM or TE corresponding to the left or right column of this group of figures. The vacuum wavelength for all these figures is the same λ_0=1.55 μm and the FDTD grid sized is the same λ_0/60 as before. The BE calculations for different waveguides use different power computation window widths covering 100%of the mode power, and they are 10 μm, 15 μm, 20 μm, 25 μm, and 30 μm respectively.

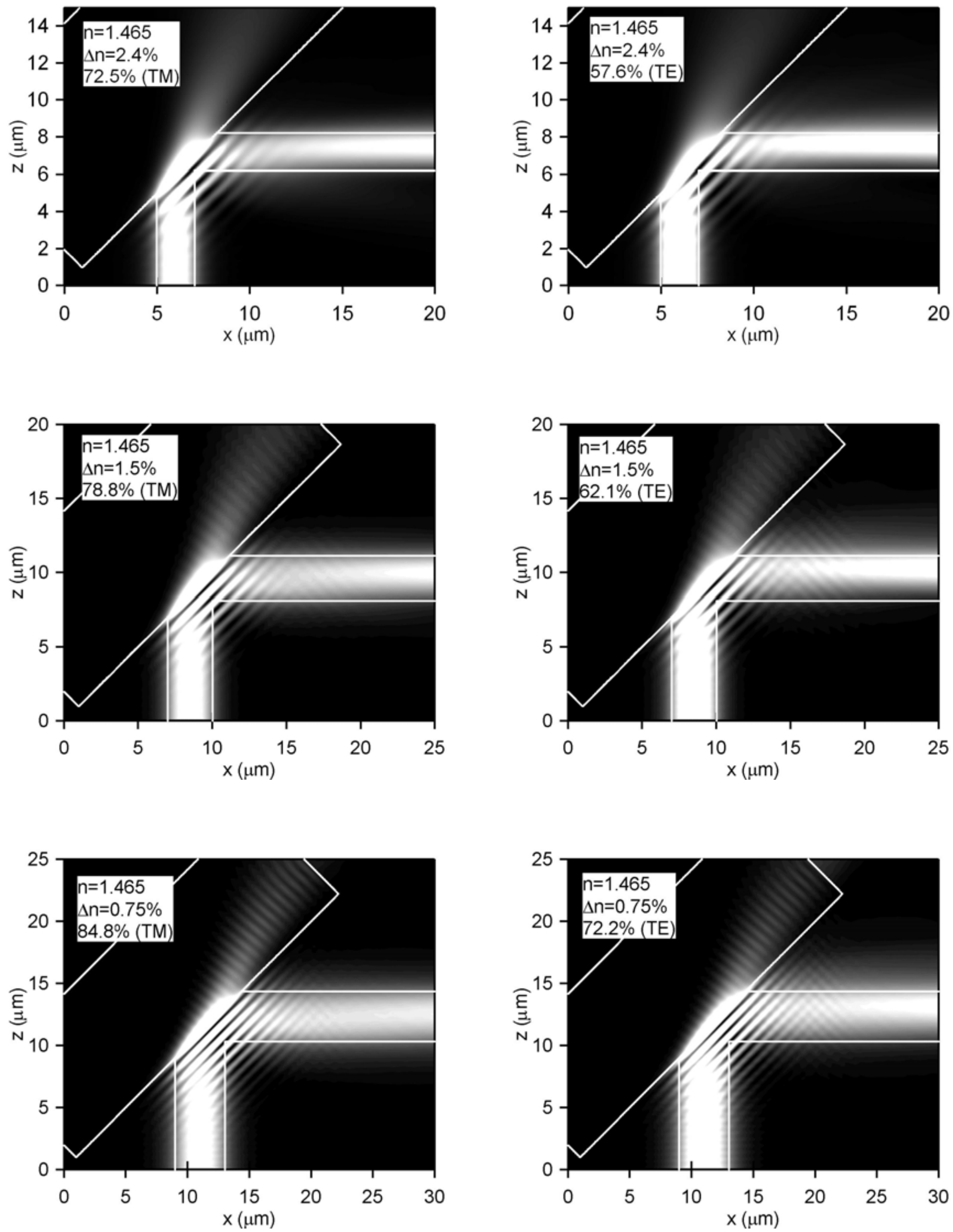

Figure 3.15 FDTD simulations for waveguide 90° bends with cladding index n=1.465

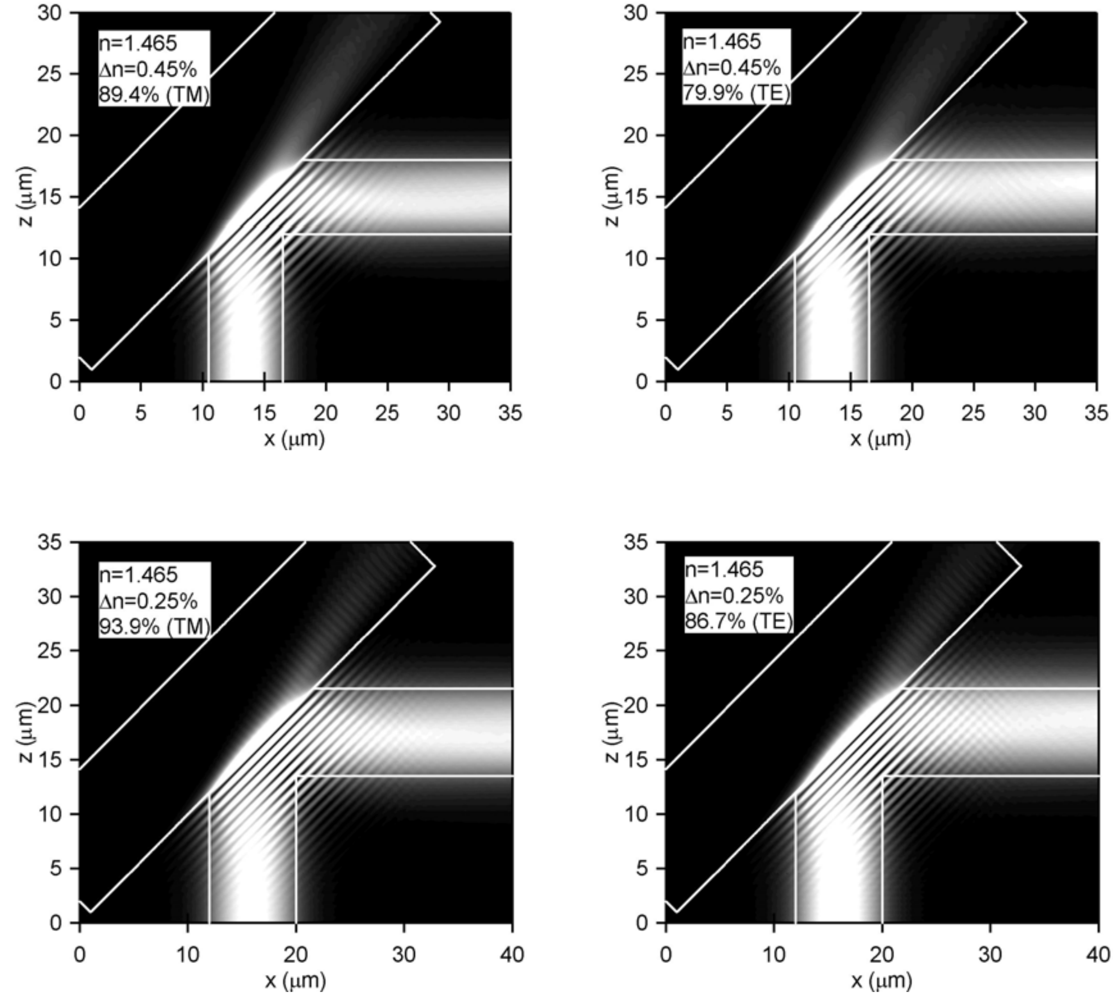

Figure 3.15 FDTD simulations for waveguide 90° bends with cladding index n=1.465 (cont)

It is noticed in Figure 3.15 that the BE improves from 72.5% to 93.9% (TM) and 57.6% to 86.7% (TE) with the MOI method for this set of waveguides with index contrast from Δn = 2.4% to 0.25%. This improvement conforms to what we expected. As mentioned before, the preference of the waveguide bend designs has given to TM illumination for an optimal output waveguide position due to different G-H shift for TM and TE polarizations. Therefore it can be seen that the fields in the right column (TE) have a little more offset from the center of the output waveguide compared with their left partners. Also attention should be paid to the dimensions for different figures, and they are in scale for x and z dimensions for each figure itself, but not in the whole group.

Shown in Figure 3.16 is the overall BE calculations from both FDTD simulations and PWE theory with MOI, and again they match extremely well. Both PWE theory and FDTD simulations expect that BE values are greater for TM light than for TE for each waveguide bend case; this is however from the Fresnel's electromagnetic theory of reflection and transmission.

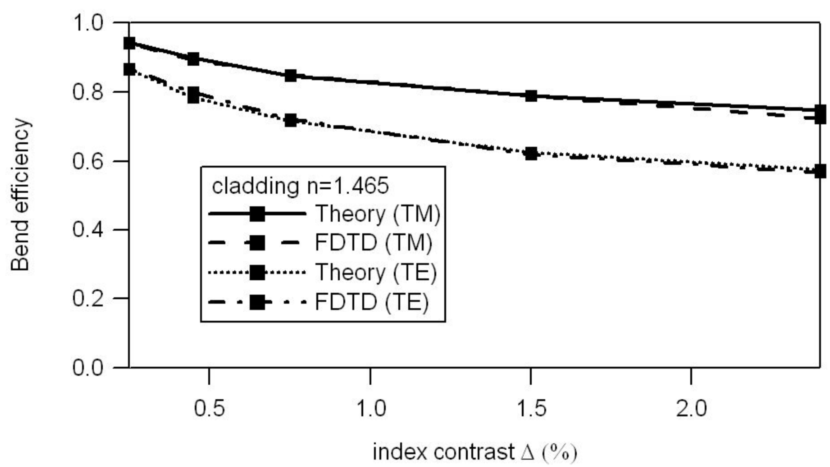

Figure 3.16 BE for 90° waveguide bends with cladding index n=1.465

3.5 Improving BE for 90° bends by using higher-index and lower-Δ waveguides

Section 3.4 shows an effective method to improve bend efficiency; however, the bend efficiency is still not very high (93.9%/86.7%) even for waveguides with minimum index contrast 0.25%. This can be explained by the angular spectrum of this set of waveguides as shown in Figure 3.14, and there still having components at the left side of the critical line even for

Δ=0.25% because the separation between $k_x = 0$ and k_{xc} is not big enough. To increase this separation and keep the bend angle 90°, the critical line has to move to the left further, and this can be achieved by increasing the cladding index. To verify this is the case, another set of simulations for waveguides with cladding index n=1.6 and the same set of index contrast Δn = 2.4%, 1.5%, 0.75%, 0.45%, 0.25% has been done in this section.

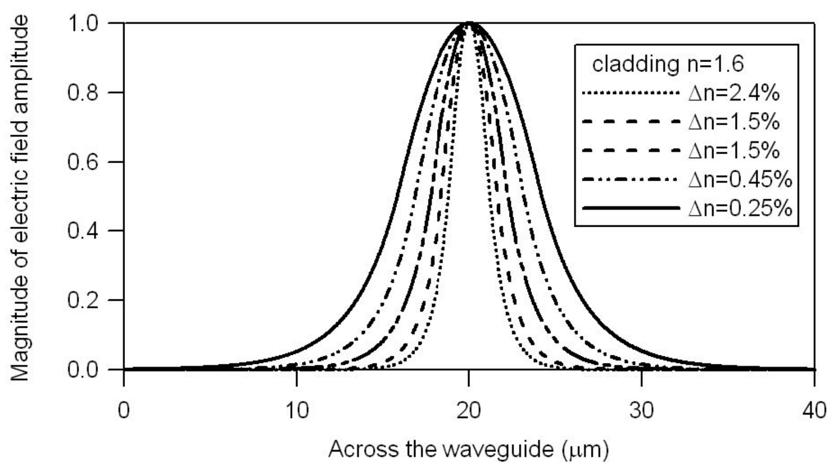

Figure 3.17 Single-mode profiles for waveguides with cladding index n=1.6

Shown in Figure 3.17 are the single-mode profiles (electric fields) for this set of waveguides. Again the waveguide widths for different Δ waveguides have been chosen properly to support only one single mode at wavelength λ_0=1.55 μm, and they are 2 μm, 3 μm, 4 μm, 6 μm, and 8 μm respectively for Δn= 2.4%, 1.5%, 0.75%, 0.45%, 0.25%. The power computation window widths for these waveguides are 10 μm, 15 μm, 20 μm, 25 μm, and 30 μm respectively as in Section 3.4. Besides the similar features for both field profiles and angular spectrums between this section and Section 3.4, it is important to notice the comparison between

Figure 3.18 and Figure 3.14. The critical line in Figure 3.18 is at approximately -0.72 μm^{-1} for this set of waveguides with cladding index 1.6 while it is at -0.21 μm^{-1} for Figure 3.14. Because of this, it is seen that waveguides with Δ=0.45% and 0.25% have almost of all their components at the right side of the critical line, and those waveguide bends are expected to have BE very high.

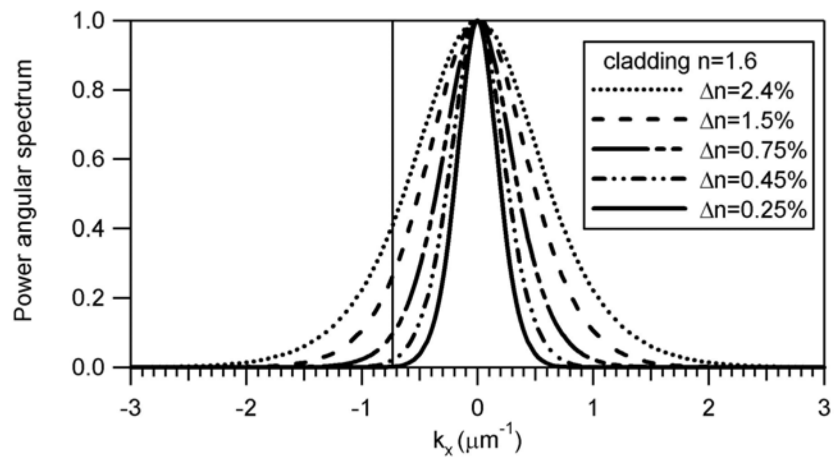

Figure 3.18 Power angular spectrums for waveguides with cladding index n=1.6

Shown in Figure 3.19 are a group of FDTD simulations for this set of waveguide 90° bends and in the order from 2.4% to 0.25% with both TM and TE illuminations. The incidence for each figure is the analytical mode for the specified waveguide either TM or TE for the left or right column of the group of figures. The vacuum wavelength for all these figures is the same λ_0=1.55 μm and the FDTD grid size is the same $\lambda_0/60$ as before.

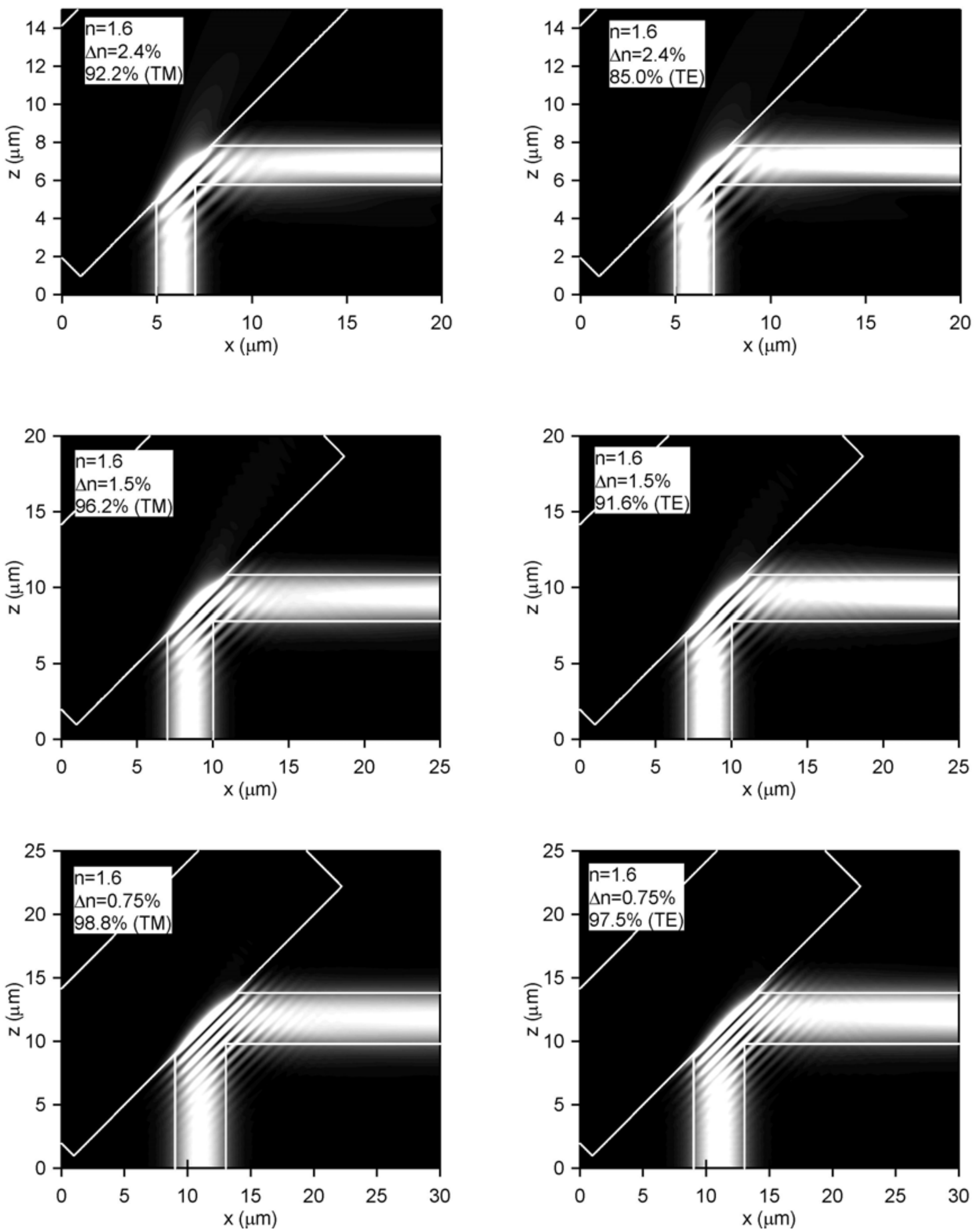

Figure 3.19 FDTD simulations for waveguide 90° bends with cladding n=1.6

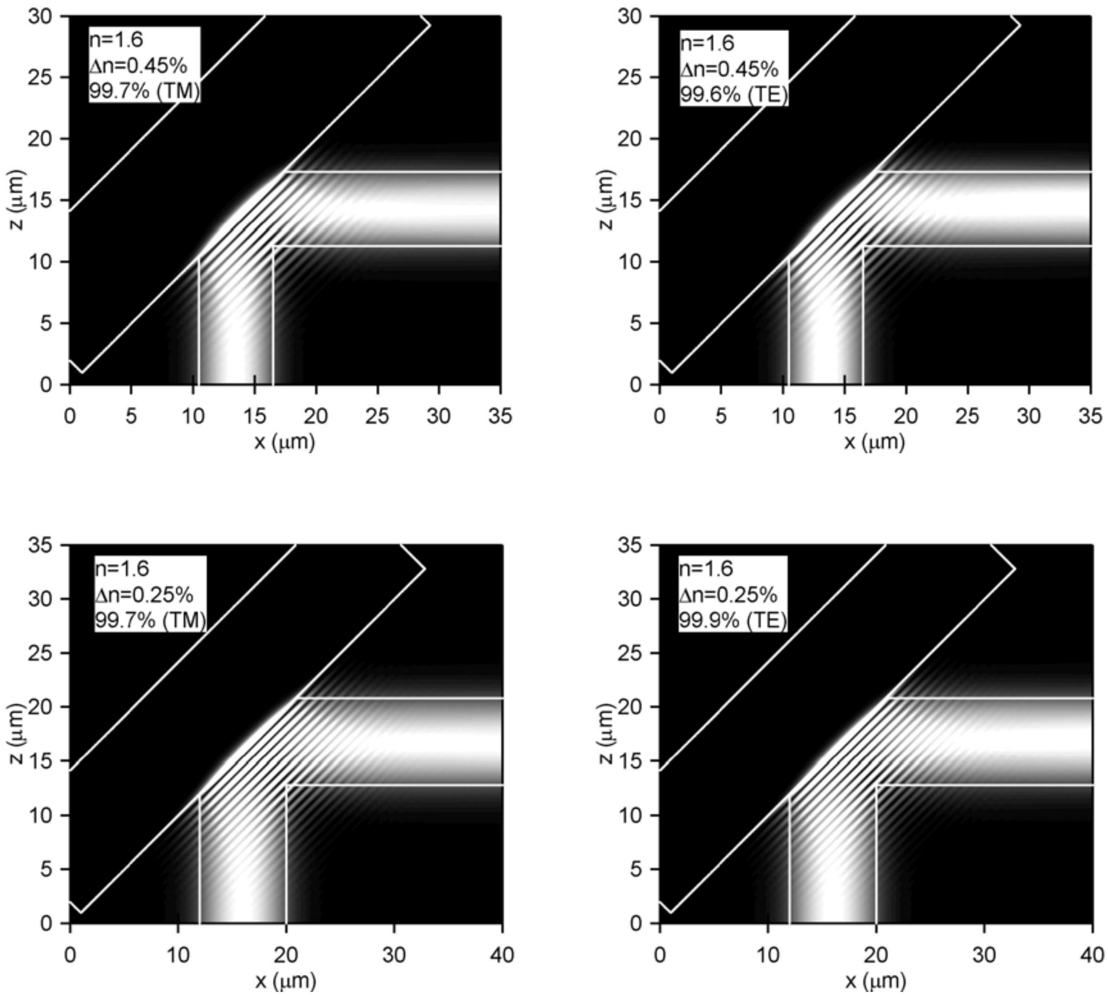

Figure 3.19 FDTD simulations for waveguide 90° bends with cladding n=1.6 (cont)

Just as we expected, the BE for this waveguide set is relatively much higher than the n=1.465 waveguide set, and it improves from 92.2% to 99.7% (TM) and 85.0% to 99.9% (TE) for index contrast Δ from Δn= 2.4% to 0.25%.

Shown in Figure 3.20 is the overall BE calculation results from both FDTD simulations and waveguide plane wave expansion theory. Comparing with Figure 3.16, BEs in Figure 3.20 are much higher, especially for waveguides with n=1.6 and Δn=0.45%, 0.25%, the BE is higher than 99% for both TE and TM illuminations. This conforms to the analysis as stated at the beginning of this section that the BE will improve with higher- index and lower-Δ waveguides.

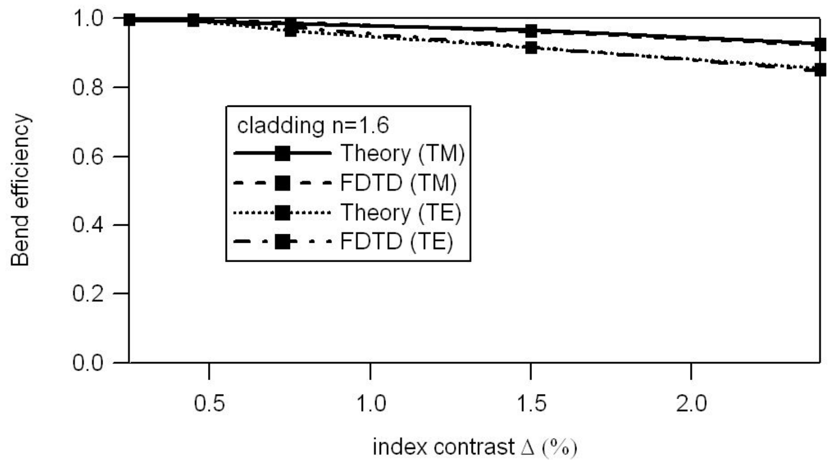

Figure 3.20 BE for 90° waveguide bends with cladding index n=1.6

3.6 Example of single air-interface polymer waveguide bends for fabrication

The purpose of the project presented in this section is to experimentally validate the approach proposed in Section 3.3: the smaller the bend angle is, the higher the bend efficiency should be. For this purpose and also considering the actual mask size, seven bend angles have been designed based on a polymer waveguide with 2D core and cladding index 1.486 and 1.477. The seven bend angles are 100º, 90º, 80º, 75.45º, 70º, 60º, and 45º corresponding to incident angles of 40°, 45°, 50°, 52.275°, 55°, 60°, and 67.5°. Special bend angle 75.45º is a calculated angle with equal Goos-Hanchen shift for both TM and TE polarizations based on a plane-wave approximation.

In this experiment, perfluorocyclobutyl (PFCB) polymer material from *Tetramer Technologies* is used to make a 3D channel waveguide with its core and cladding index 1.4901 and 1.4766 respectively at wavelength 1.55 μm. *Fimmwave* [57] is used to design this channel waveguide and it turns out to have a cross-section 4 μm × 4 μm to support its only single mode. The 3D waveguide can be further transformed to a 2D slab waveguide by effective index method (EIM) as explained in Section 2.3.3. The transformed equivalent 2D slab waveguide has width 4 μm and core and cladding refractive index 1.486 and 1.477 respectively at wavelength λ_0=1.55 μm. The effective index is 1.482 and index contrast is about 0.6%. Waveguide bends in this section are designed based on this 2D PFCB waveguide.

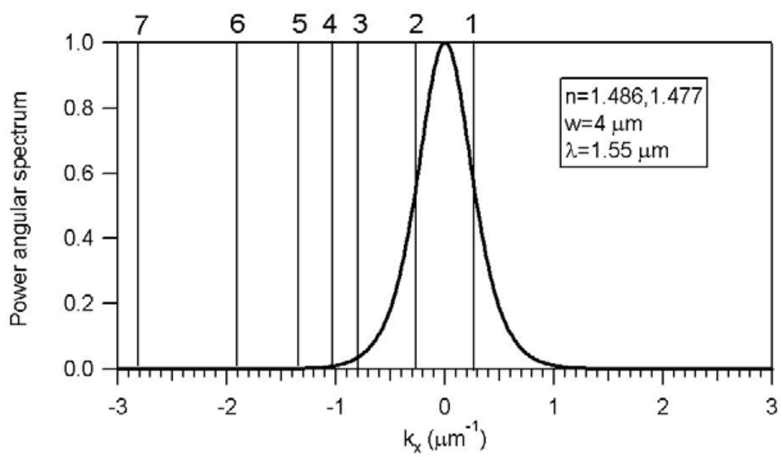

Figure 3.21 An overlap of power angular spectrums

For a single air-interface bend with this PFCB polymer waveguide, the critical angle θ_c is about 42.4°. This critical angle will give different angle difference $\Delta\theta_c = \theta_c - \theta_0$ between θ_c and θ_0 for different waveguide mode incident angle θ_0. A bigger incident angle makes $|\Delta\theta_c|$

bigger, for example, $\left|\Delta\theta_c\right| = 25.1^\circ$ for $\theta_0 = 67.5^\circ$, which corresponds to a 45° bend. Expressing this relative critical position in the power angular spectrum as before for all seven bend angles with a overlap of k_x=0 representing the mode incident angle for all the seven bends from 100° to 45°, Figure 3.21 is attained.

Numbers 1 to 7 on the top of the figure correspond to relative critical positions for bend angles from 100° to 45°. It is noticed that from 4 (75.45° bend) to 7 (45° bend), almost all the plane wave components have fallen at the right side of the critical line, thus the bend efficiency should be very high and close to 100%.

Figure 3.22 is the theoretical expectance of the power reflectivity as a function of incident angle based on PWE theory and Fresnel's equations. It is seen that for incident angles greater than 50°, the power reflectivity gets close to 1. Figure 3.22 expects the same as Figure 3.21 but from different views.

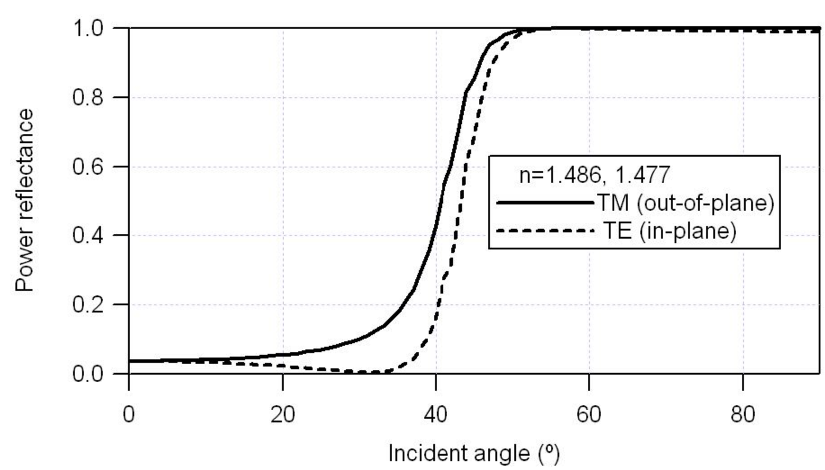

Figure 3.22 Power reflectance calculated by plane wave expansion theory

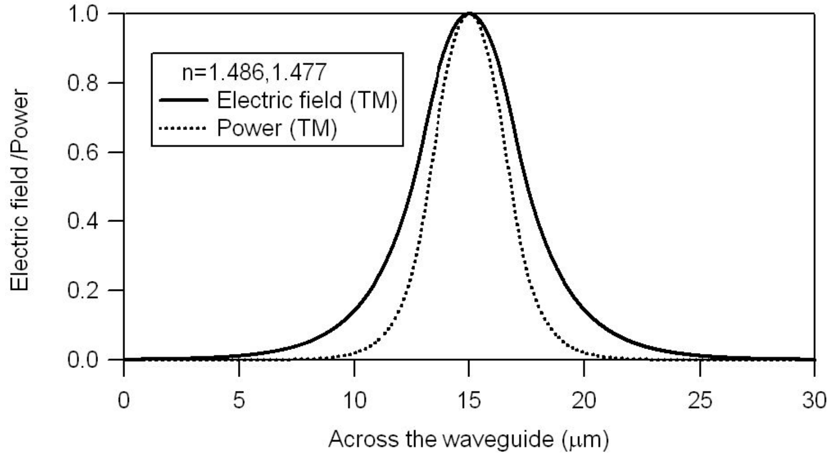

Figure 3.23 Electric field and power profiles for PFCB waveguide

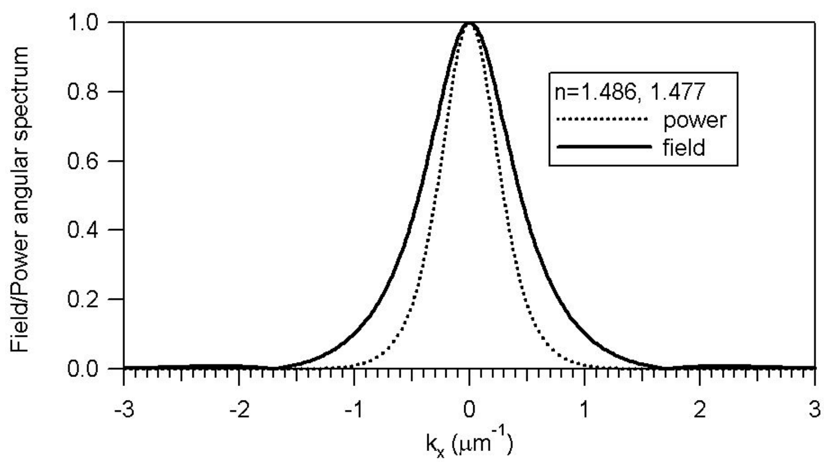

Figure 3.24 Field and power angular spectrums for PFCB waveguide

Figure 3.23 is the fundamental mode profile (electric field) and its power distribution (normalized magnitude of time-averaged Poynting vector) for this 2D slab polymer waveguide. It is seen the field extends approximately 30 μm while the power takes about 20 μm. This power width provides us one basic parameter for the computation monitor width to calculate the bend efficiency (BE). Figure 3.24 is its field and power angular spectrum. It can be seen that this PFCB waveguide has a narrower angular spectrum compared with Figure 3.6 (b) (page 43) for the waveguide in Section 3.1 with core and cladding index of n=1.5 and 1.465.

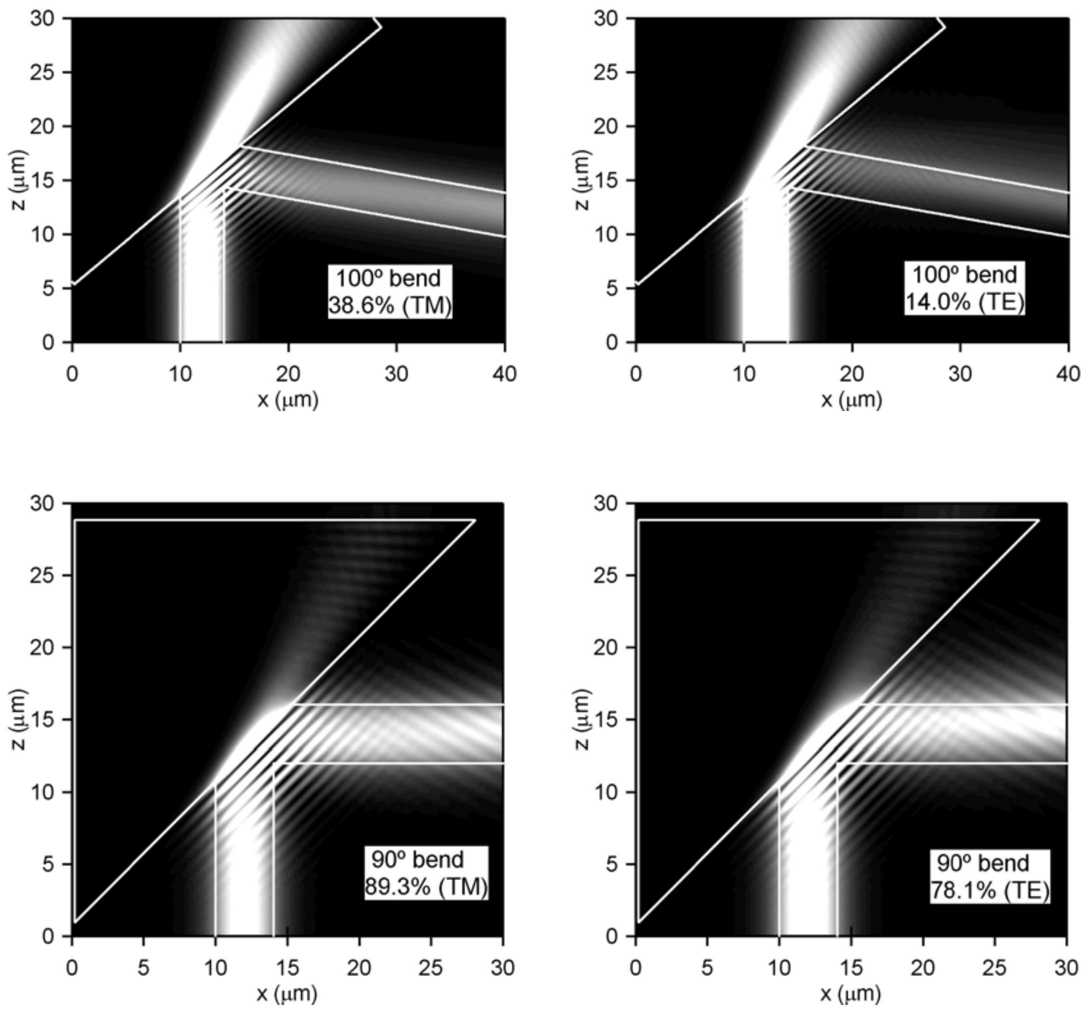

Figure 3.25 FDTD simulations of different bends for PFCB waveguide

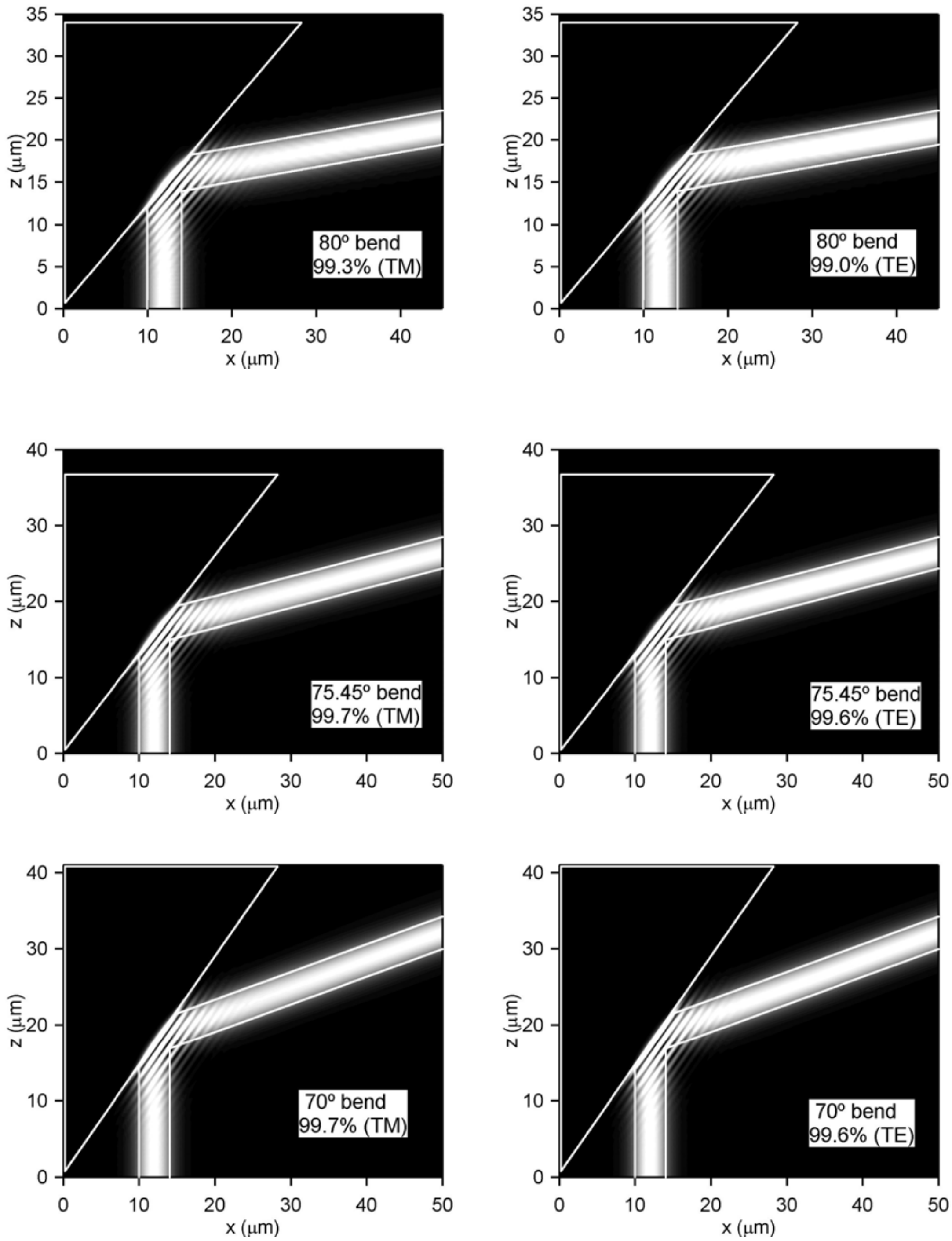

Figure 3.25 FDTD simulations of different bends for PFCB waveguide (cont)

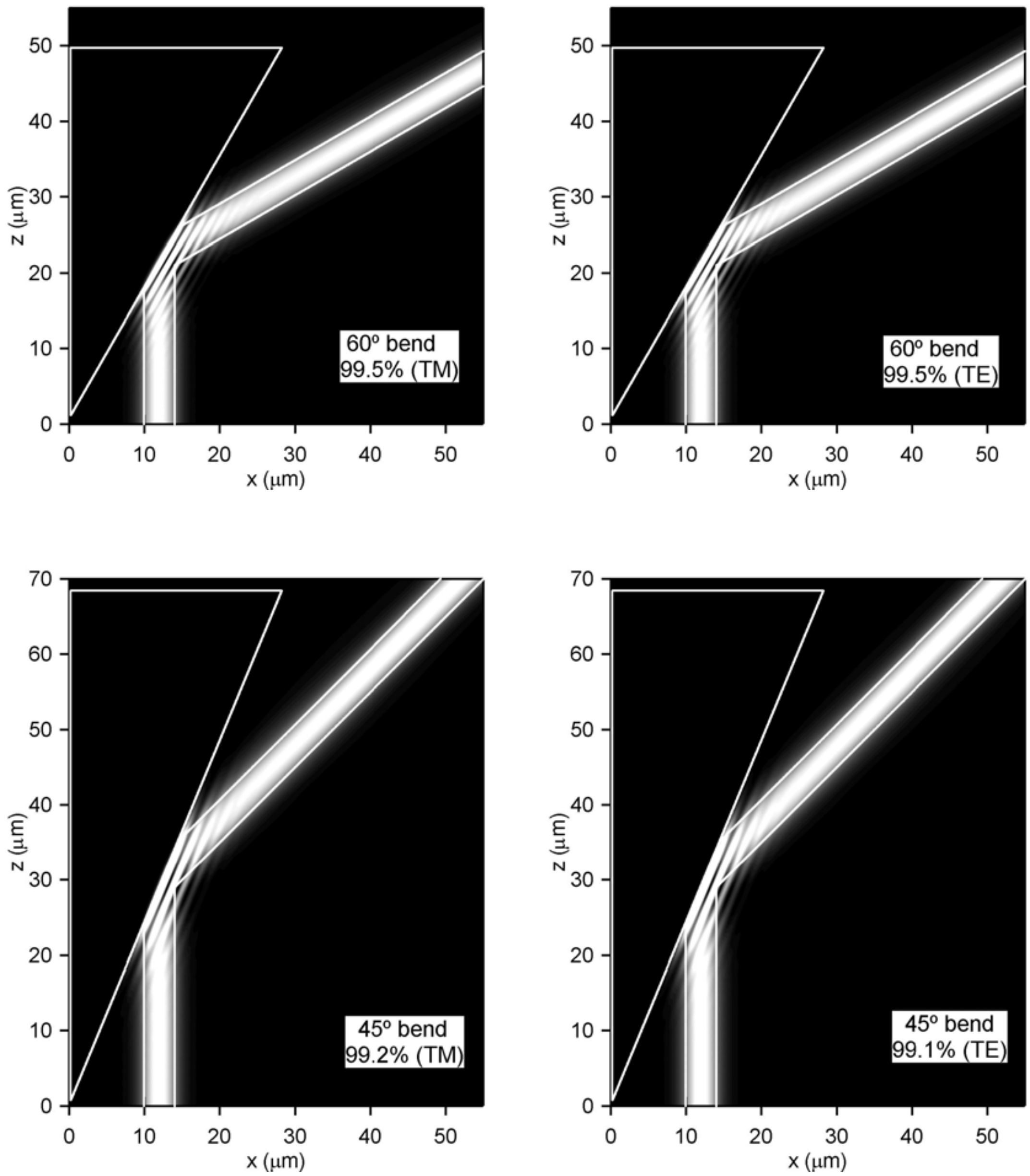

Figure 3.25 FDTD simulations of different bends for PFCB waveguide (cont)

FDTD simulations for this set of waveguide bends are given in Figure 3.25 with FDTD grid size $\lambda_0/60$ at λ_0=1.55 μm. The left column of this group of figures is for TM illumination while the right column is for TE. Because of the Goos-Hanchen difference for different bend angles and different polarizations, again the output waveguide position for each bend case has been optimized differently and given preference to TM illumination. Therefore it is seen that the light is well centered at the output waveguide for the left column while having some different offset for the right column. It is shown in Figure 3.25 that the bend performance is very poor for bend angles of 100° and 90° and also they have big G-H shift difference for TM and TE illuminations. All the other bend angles beyond 100° and 90° do not show obvious G-H shift difference for TM and TE polarizations.

Figure 3.26 shows the BE calculations from FDTD simulation and PWE theory with MOI for both. Again they match extremely well. Figure 3.26 agrees well with Figure 3.22.

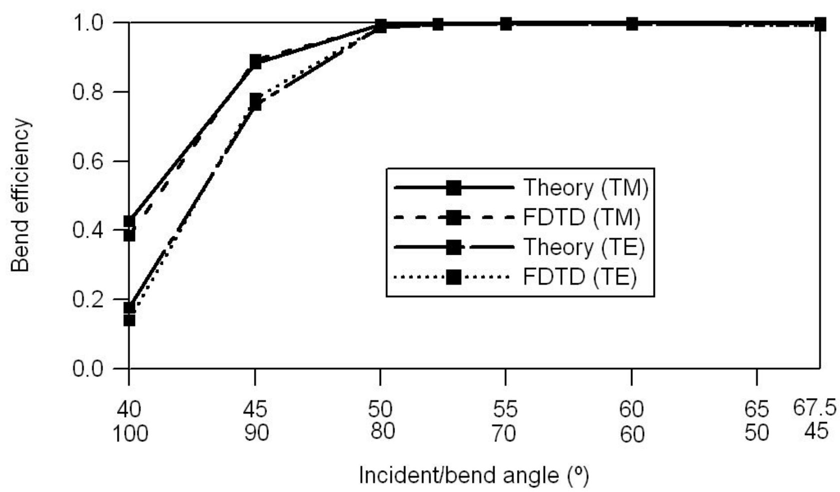

Figure 3.26 BE calculation for PFCB waveguide bends

The following figures are the tolerance analysis from a series of FDTD runs with bend efficiency as a function of the z coordinate of the lowest air triangular vertex. This tolerance analysis is also one of the design processes of finding the best geometry to have the highest BE. By changing the z coordinate of the lowest air triangular vertex, the relative position between air and output waveguide has been changed, and then the optimum position having the highest BE has been picked for each bend angle. The FDTD simulations in Figure 3.25 all have optimized z coordinates as 0.5, 0.7, 0.5, 0.8, 1.0, and 0.8, respectively, in unit of μm, for bends from 90° to 45°. However, as stated before about G-H shift for different polarizations, preference is given to TM for each bend case. Note that bend 100° has very low BE, and its purpose to be designed is for comparison and showing the concept with the allowance of the mask size, thus no tolerance analysis is done for this case.

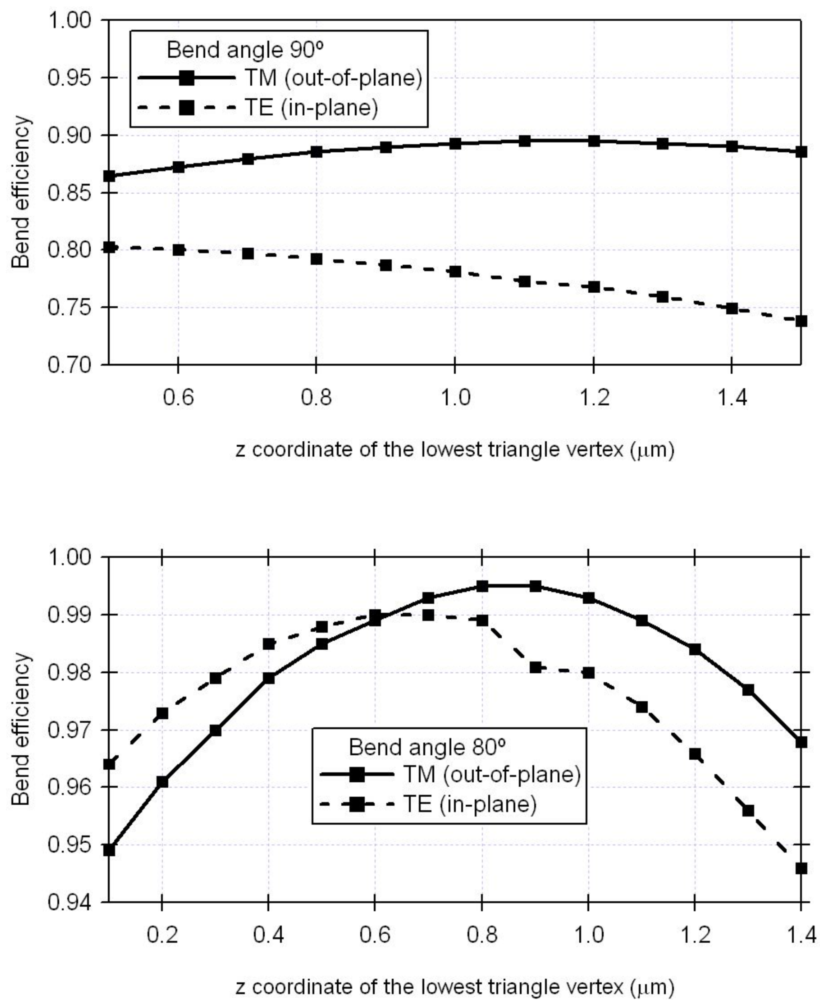

Figure 3.27 Tolerance analysis for different bends

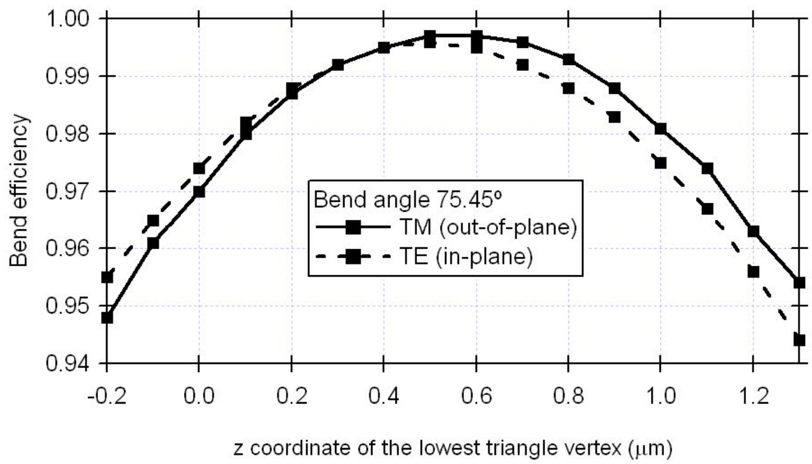

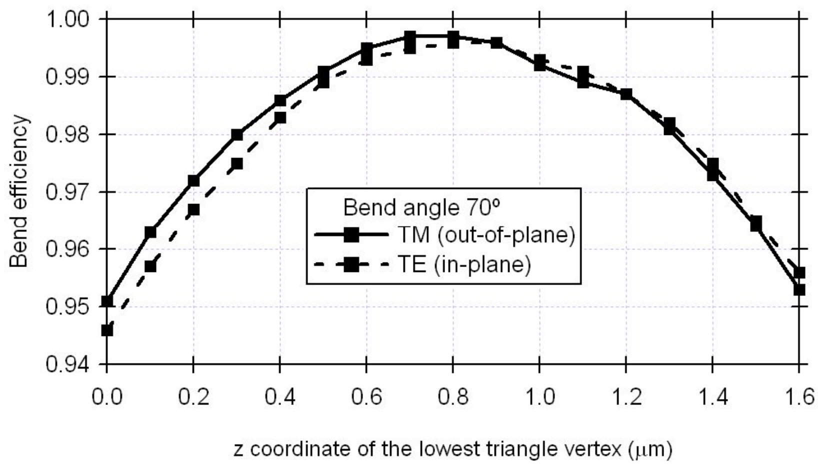

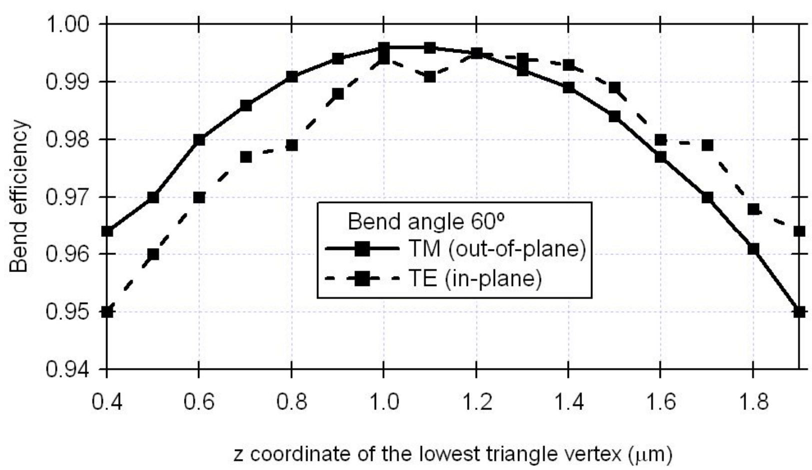

Figure 3.27 Tolerance analysis for different bends (cont)

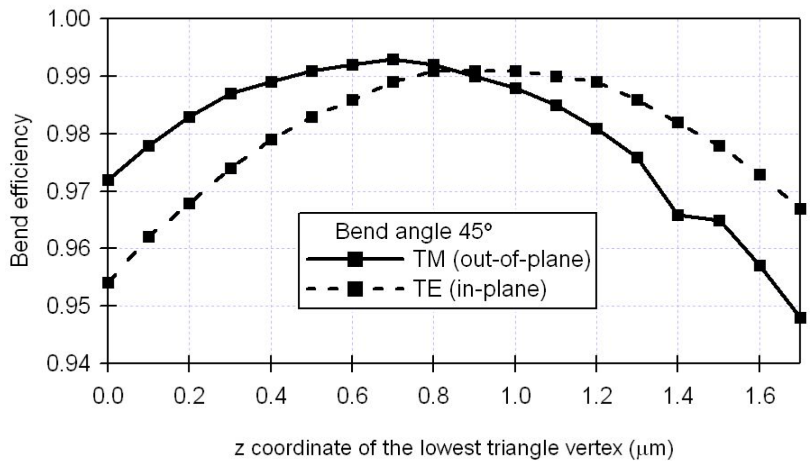

Figure 3.27 Tolerance analysis for different bends (cont)

Shown in Figure 3.27, it is very obvious that the bend 90° has a bigger G-H shift difference for TM and TE light and lower BE. All other figures have a BE range from 0.94 to 1 with slightly different z allowable coordinate range, approximately about ±0.7 μm from the center position.

It is interesting to compare tolerance curves for the bend 75.45° and 70°. First of all, these two figures have the smallest G-H shift difference between TM and TE (1% or 0.7%) compared with other figures. Individually, the G-H shift shows opposite change patterns for these two bend cases. The bend 75.45° starts with a slightly bigger BE value for TE than for TM, with increasing z coordinate, and then TM starts to pick up and gradually is bigger than TE after going through an equal point. The bend 70° has change pattern for TM and TE curves opposite to the bend 75.45°. For bend angles bigger than 75.45°, it is seen from Figure 3.27 that they follow the pattern of bend 75.45° although with bigger difference between TM and TE for bigger bend angles. For bend angles smaller than 70°, they follow the bend 70° pattern although with bigger difference between TM and TE for smaller bend angles. This indicates that at some middle position between 75.45° and 70° it will be the bend angle with actual equal G-H shift, which will have overlapping TM and TE curves.

Table 3.2 shows an overall performance for each bend case with tabulated numbers listed compared with curves in Figure 3.26 with MOI method. Also listed in the table is the tolerance range having BE greater than 95% based on Figure 3.27, and it is seen a range of about ± 0.7 μm for the z coordinate change and for bend angles smaller than 80°. This is a relatively relaxed fabrication tolerance.

Table 3.2 Overall performance of different bends

Bd_angle (°)	**Inc_angle (°)**	**Bend Efficiency**				**Tolerance (μm)**
		Theory (TM)	**FDTD (TM)**	**Theory (TE)**	**FDTD (TE)**	
100	40	0.428	0.386	0.176	0.14	NA
90	45	0.882	0.893	0.764	0.781	(-0.3,0.5)
80	50	0.994	0.993	0.988	0.99	(-0.5,0.7)
75.45	52.275	0.998	0.997	0.996	0.996	(-0.7,0.7)
70	55	0.999	0.997	0.997	0.996	(-0.8,0.8)
60	60	0.999	0.995	0.996	0.995	(-0.7,0.7)
45	67.5	0.999	0.992	0.999	0.991	(-0.7,0.7)

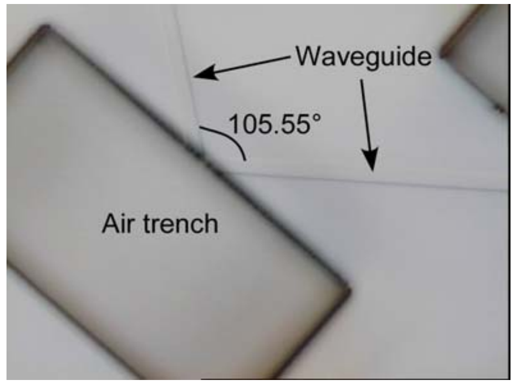

(a) a single 75.45° bend

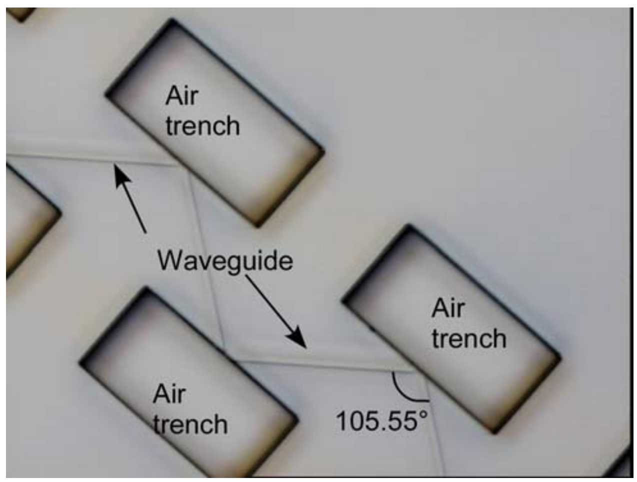

(b) three 75.45° bends

Figure 3.28 SEM image of fabricated PFCB waveguide bends

Shown in Figure 3.28 are two SEM images of PFCB waveguide bends fabricated by graduate students, Jaime Cardenas and Nazli Rahmanian, with a single and three bends of 75.45°. Testing and measurements are under way, and an initial experimental result for a bend 45° has bend efficiency of about 85%.

CHAPTER 4

MULTIPLE-LAYER AIR-TRENCH WAVEGUIDE BENDS

Chapter 3 concentrates on single-air-interface waveguide bend designs and simulations, and three approaches of improving bend efficiency have been proposed. However those approaches require either changing bend angles or material system; for some situations with strict fixed requirements for these two parameters, this chapter proposes one more alternate method, using multi-layer structures to improve the bend efficiency. This can be understood from the angular spectrum shown in Figure 3.6 (b) (page 43), the plane-wave components at the left side of the critical line have only partial reflection, and adding more layers can directly increase the power reflectance for those components.

The high reflectivity for the multi-layer bend structures is close to the performance of traditional periodic Bragg mirror. It is well-known that traditional Bragg mirrors can give high reflectivity with properly-designed quarterwave-thickness alternate layers. These mirrors usually work at normal incidence as filters or reflectors for the laser cavity [72]. However, to the best of our knowledge, Bragg mirrors have not been introduced into the waveguide regime as waveguide bend structures yet. In this chapter, this originative application will be explored, including quasi-Bragg (optimized by a combination of micro-GA and FDTD) and Bragg (periodic) mirrors as the waveguide bends.

4.1 Quasi-Bragg/Bragg air-trench 90° bend

The single air-interface 90° waveguide bend in Section 3.1 has bend efficiency only 72.3% and 57.5% for TM and TE light. The low BE is due to the waveguide mode incidence, and those decomposed plane-wave components having partial reflection referring to the angular spectrum shown in Figure 4.1 (same as Figure 3.6(b) on page 43). Therefore transmission occurs for those components at the left side of the critical line.

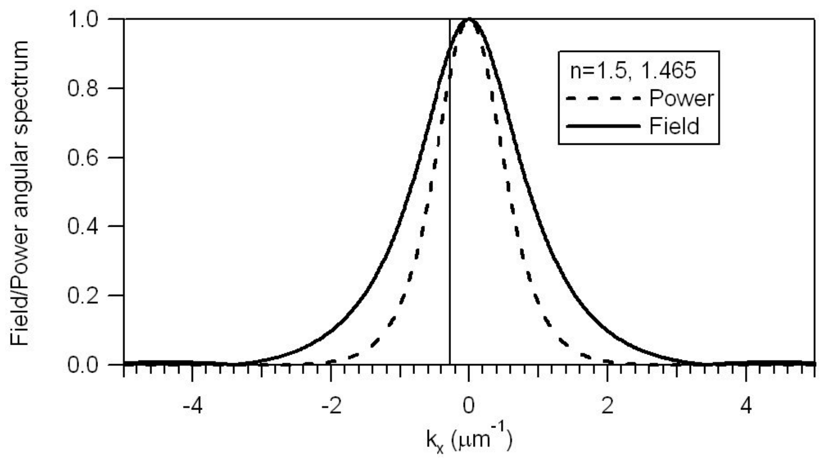

Figure 4.1 Angular spectrum of the waveguide as in Section 3.1

A novel approach with multi-layer structures has been gradually formed by adding more interfaces one by one after seeing the gradual improvement of bend effect. The approach starts from first decreasing the big thickness of the rectangular air-trench as shown in Figure 3.2 (page 37) and bringing the second interface closer to add more reflection for those transmitted components. Immediate improvement has been observed by having an air trench layer with some reasonable thickness. However there is still some light transmitted and lost. This can be understood as follows. The addition of the second air interface increases the reflection of angular spectrum plane wave components that do not undergo TIR, but at the cost of permitting frustrated TIR to occur for the TIR components.

To reflect back those transmitted part, the same logic of adding more interfaces is followed to increase the reflectance. It turns out that two or three air-trench layers can improve the bend effect with some reasonable thickness and separations, and further addition of layers does not significantly improve the bend efficiency any more.

To achieve an optimal performance, with the help of a combination of micro-genetic algorithm (μGA) and FDTD [63], the air-trench layer thickness, length and the z coordinate of the lowest vertex point of the air-trench have been set to be variables for the μGA-FDTD application.

Shown in Figure 4.2 is the FDTD simulations with FDTD grid size $\lambda_0/80$ at $\lambda_0=1.55$ μm for these multi-layer structures with optimal dimensions for TM illumination. It is seen that the bend efficiency has been improved to 81.7% and further to more than 93% with one or more-layer air-trenches from 72.3% with single air-interface bend for TM light. Both two and three air-layer structures improve bend efficiency 20% (with MOI) from the single air-interface mirror.

The working principle for the multi-layer air-trench mirrors can be understood as that the first air interface reflects much of the incident energy through TIR and the rest of the interfaces in the stack act similarly as a Bragg mirror to reflect that portion of the angular spectrum that does not undergo TIR. However, the finite trench thickness of the first layer will result frustrated TIR [73], and the multi-layer structures have to operate over the entire range of angular spectrum to improve reflectance for the left-side components while compensating for the TIR part. The work in this section has been published in *Optics Express* [74].

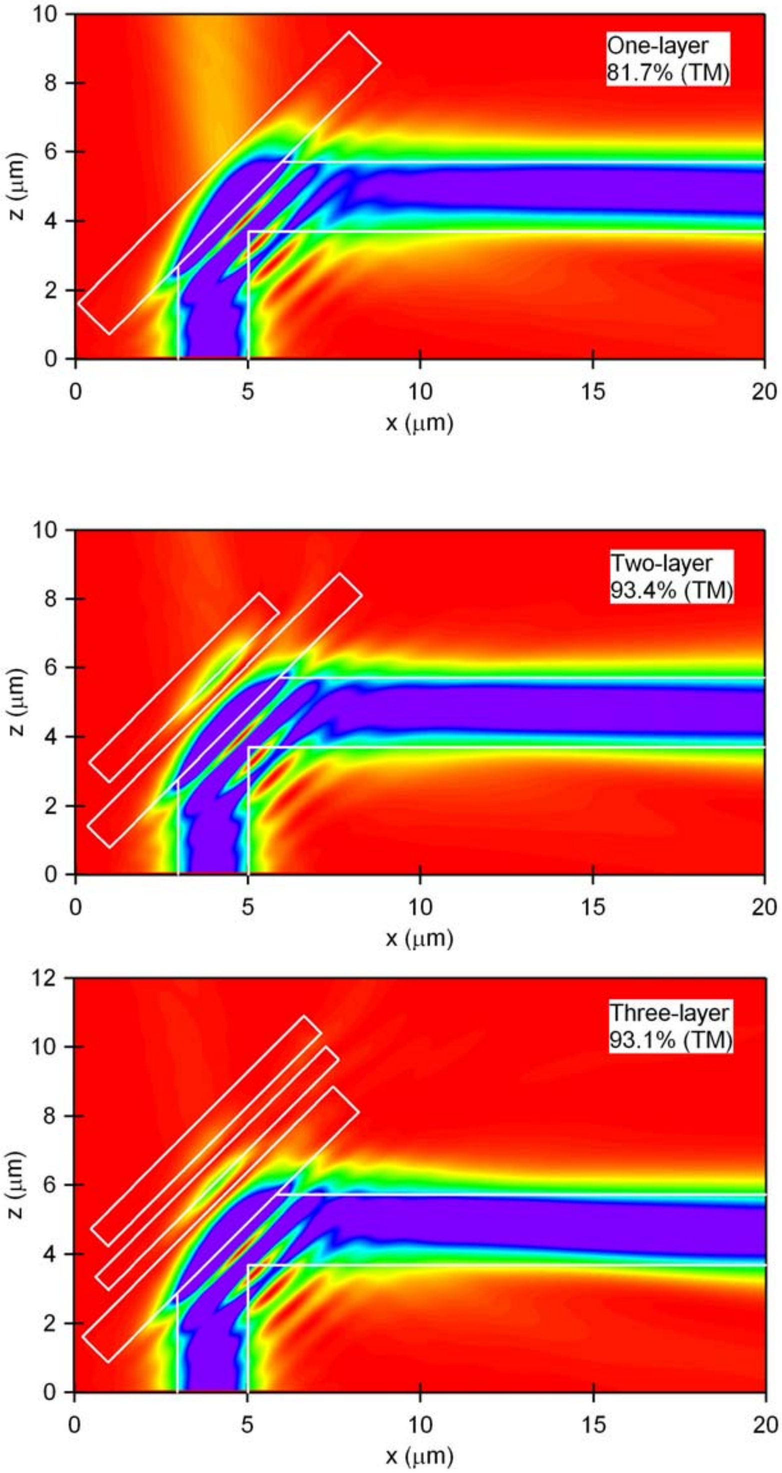

Figure 4.2 FDTD simulation of optimized multi-layer air-trench mirrors (TM)

Since this waveguide has index contrast 2.3%, which is not very low, its angular spectrum is relatively wide compared with other lower-Δ waveguides in Chapter 3. Therefore the multi-layer mirrors here didn't give very high efficiency, and it is expected that higher efficiency can be achieved for lower-Δ waveguides with narrower angular spectrum. The narrower the angular spectrum is, it is more close to a plane-wave approximation, for which the multi-layer can better force a constructive reflection.

Although the layer's length in Figure 4.2 is also set to be one variable when doing optimization, it is found that it doesn't affect the performance very much as long as it is not very short. The layer's thickness and separations between air-trenchs are critical parameters for achieving an optimal performance. Table 4.1 shows the detailed optimal geometry dimensions for each case of Figure 4.2.

Table 4.1 Geometry and performance of waveguide 90° bends with multi-layer structures

Structure (# of air trenches)	**Trench Dimensions (μm)**	**Trench Separation (μm)**	**Bending Efficiency (TM)**	
			By MOI	**By Power ratio**
1 Layer	11.10×1.28	—	81.7%	85.7%
2 Layers	10.35×0.90 6.95×0.81	0.44	93. 4%	94.8%
3 Layers	10.05×1.05 9.42×0.52 8.70×0.70	0.44 0.38	93.1%	97.2%

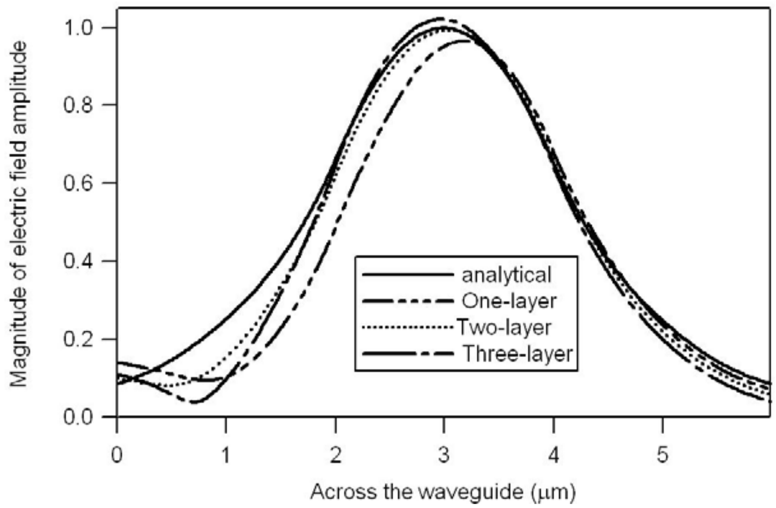

Figure 4.3 Comparison of electrical field amplitude for 90° bends of Figure 4.2

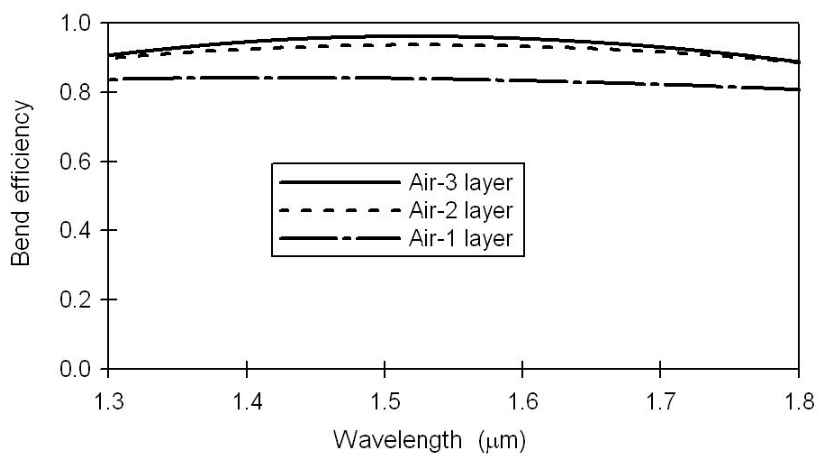

Figure 4.4 BE dependence on wavelength for 90° bends of Figure 4.2

Shown in Figure 4.3 is an electric field amplitude profile comparison among the input mode and the actual reflected field profiles across the output waveguide for the cases in Figure 4.2. In general, the profiles match the input profile better at the center position than the sides. The two and three-layer mirrors match better than the one-layer configuration.

An additional attractive feature of multiple air-trench 90° bends is illustrated in Figure 4.4 in which the bend efficiency (calculated by power ratio, not MOI, limited by the FDTD code) is shown as a function of wavelength. In each case, the bend efficiency is only weakly dependent on wavelength. However, it is seen that the more-layer mirrors are a little more sensitive to the wavelength than the one-layer mirror.

Although neither of the optimal geometry has a rigorous periodic structure as shown in Table 4.1, the multi-layer air-trench structures do work like Bragg mirrors having high reflectance. They are called Quasi-Bragg mirrors in this dissertation. This leads us to investigate how a periodic Bragg mirror works as a 90° waveguide bend. However due to the TIR situation from a plane wave approximation, no analytical layer thickness can be available. By experience and with some judicious choice based on the geometry in Figure 4.2, a 3-layer periodic mirror with air-trench layer thickness 0.8 μm and separation 0.4 μm is simulated for the TM case.

Figure 4.5 is the FDTD simulation for this 3-layer Bragg mirror, which has surprisingly high-efficiency 93.6%, even a little better than the optimized two and three-layer air-trench mirrors. Figure 4.6 is the bend efficiency (calculated by power ratio) curve as a function of wavelength for the two 3-layer Bragg and Quasi-Bragg mirrors. It is seen that this Bragg mirror has similar performance as the Quasi-Bragg mirror has.

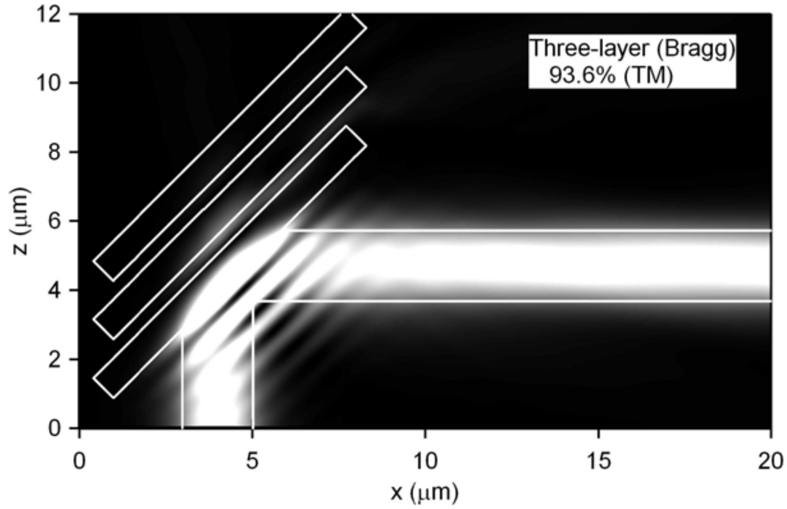

Figure 4.5 FDTD simulation for 3-layer air-trench Bragg mirror (TM)

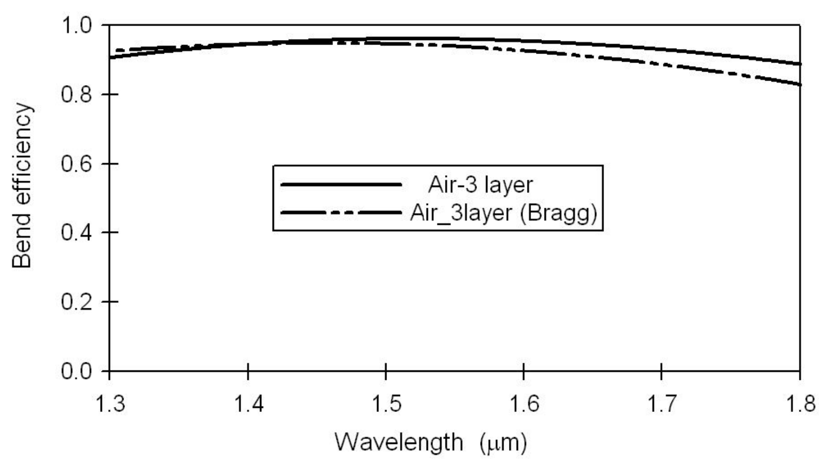

Figure 4.6 BE dependence on wavelength for 3-layer mirrors

This infers that a wide latitude of geometries may exist giving high efficiency for this 90° waveguide bend. An indirect support for this inference is the property of Figure 4.6, that is, BE is weekly dependent on wavelength. For multi-layer structures to have high reflectance, the fundamental reason comes from the constructive phase difference between layers. As we know, the phase difference between the neighboring interfaces is a function of wavelength, layer thickness and propagating directions. If the BE is weakly dependent on wavelength, it will also have relaxed tolerance on the layer thickness. A direct proof for this inference is a relationship of BE and layer thickness change. However, from another point of view, it is seen that μGA-FDTD is very helpful in quickly finding one good solution although the solutions may be not limited to only one.

Shown in Figure 4.7 are the FDTD simulations for TE light with the same geometry as in Figures 4.2 and 4.5. It is seen that there is not much improvement with the application of multi-layer mirrors, and the bend efficiency stays essentially the same except that the 3-layer Bragg mirror has about 10% lower BE. The reason for this low TE reflectivity may be related with the unique Brewster phenomena especially for TE light, and the Brewster angle here is about 34.0° based on a plane wave approximation with n=1.485 and n=1. This Brewster angle incidence is still in the left range of ±18° around $\theta_0 = 45^\circ$ from the angular spectrum shown in Figure 4.1. This means the TE reflectance will be zero for those plane-wave components having incidence at neighbor of 34.0°, and these components will transmit through any interfaces and lost. Adding more layers will not improve the reflectance for these components.

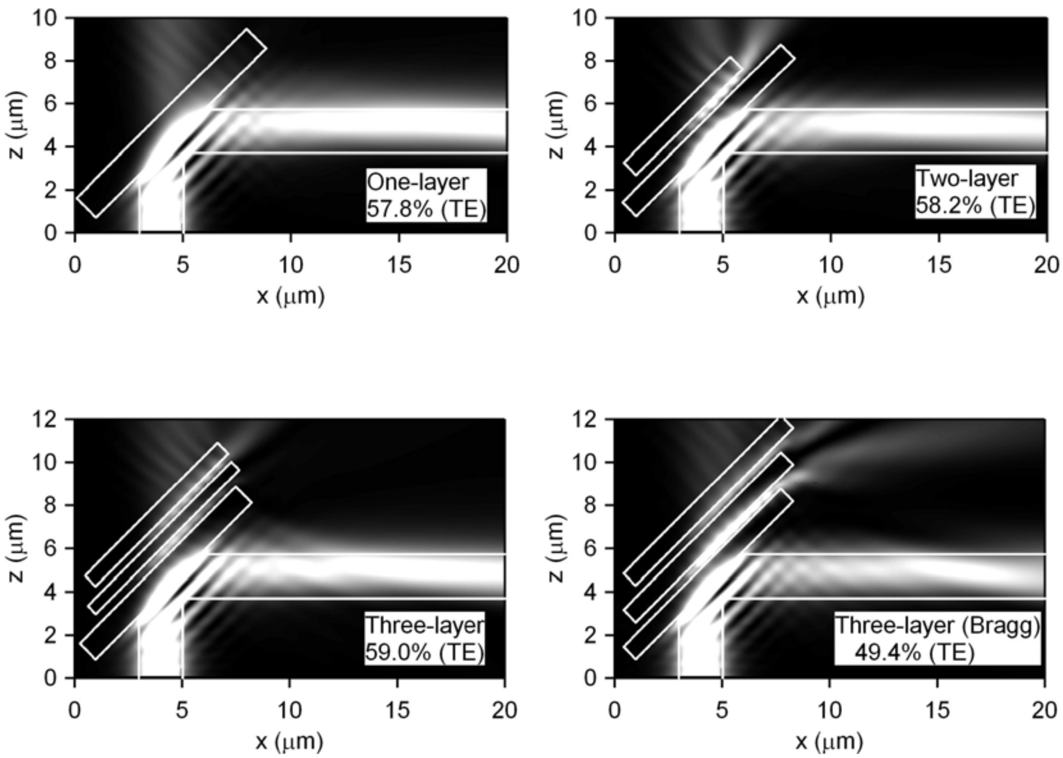

Figure 4.7 FDTD simulation of the multiple-layer mirrors (TE)

4.2 Bragg air-trench waveguide bends

The following example is to design a waveguide bend for a Gyro project using the Gyro waveguide as stated in Section 2.3.3. This waveguide has a 2D transformed slab waveguide core and cladding indices of 1.6302 and 1.6251 respectively, index contrast 0.3%, and width 3.5 μm to support its only TM fundamental mode at wavelength of λ_0=1.33 μm. Figure 4.8 is the normalized field and power space profiles.

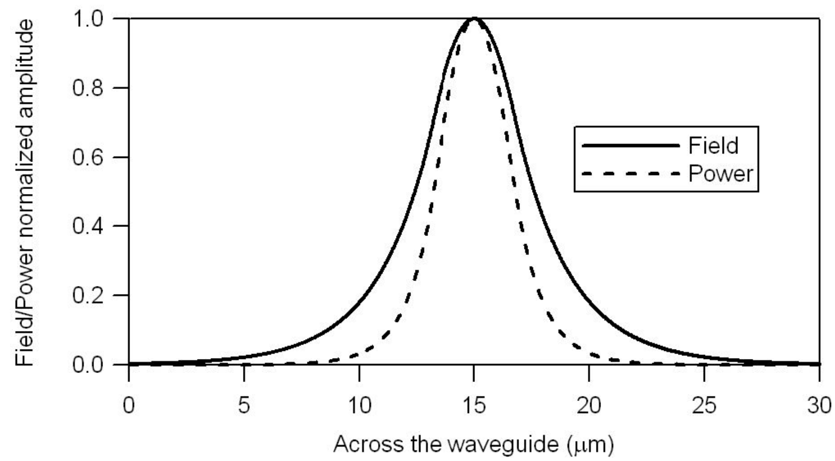

Figure 4.8 Electric field and power profile for Gyro waveguide

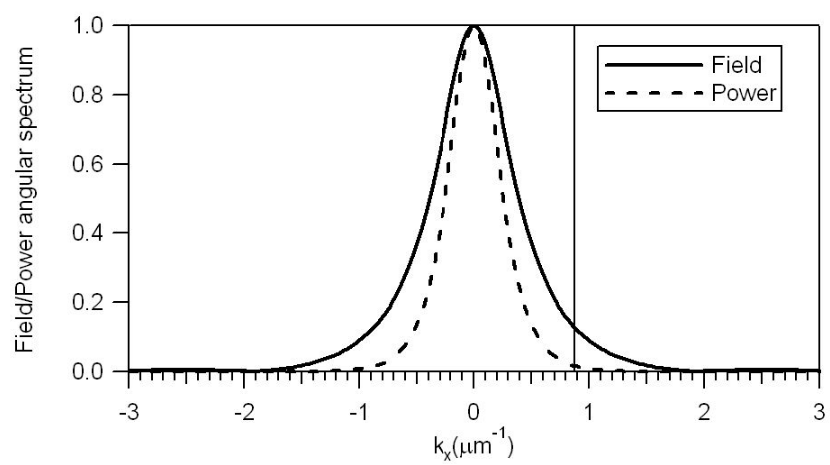

Figure 4.9 Field and power angular spectrum for Gyro waveguide

Due to the project's needs, this waveguide bend is required to work at Brewster angle incidence, and to reflect TM light while transmitting TE light. The reflectance for TM light is required to be as high as possible. The Brewster angle is defined by the cladding index 1.6414 seen by the TE light. With an approximate interface of this cladding and air the Brewster angle is approximately 31.35°, which is equivalent to a 117.3° bend angle. FDTD predicts bend efficiency of 20.7% for a single air-interface mirror with TM illumination.

This low bend efficiency 20.7% can be understood from the waveguide's angular spectrum as shown in Figure 4.9. The critical angle is about 38.0° based on a plane wave approximation with cladding refractive index 1.6251, seen by the TM light, and air n=1. Figure 4.9 shows that most of the plane wave components are at the left side of the critical line $k_{xc} = 0.89 \mu m^{-1}$ and those components can only have partial reflection. Thus it is not a surprise to get the low bend efficiency of 20.7% for a single air-interface mirror approach.

However, because of this partial reflection for the 117.3° waveguide bend from a plane-wave approximation, a Bragg mirror with periodic air interlayers can be designed to improve the TM bend efficiency. The reason to choose air is for the consideration of high index contrast and feasibility of fabrication. To design a high-efficiency Bragg mirror, the important parameters to define are the thickness and number of the alternate layers. For an abnormal incidence, the formula calculating the thickness is [75]

$$nt \cos\theta = M \frac{\lambda_0}{4} \ , \tag{4.1}$$

where n, t and θ stand for refractive index, layer thickness and propagating angle in each alternate layer, M stands for any odd numbers, and λ_0 = 1.33 μm for this example.

For the feasibility of fabrication, it is better to have thick layers, thus taking M =1 for the air layer and M =3 for the layer with n=1.6251, then the layer thickness is 0.62 μm and 0.72 μm respectively. To get a reflectivity higher than 99% with a plane-wave approximation at TM illumination, five alternate layers are needed.

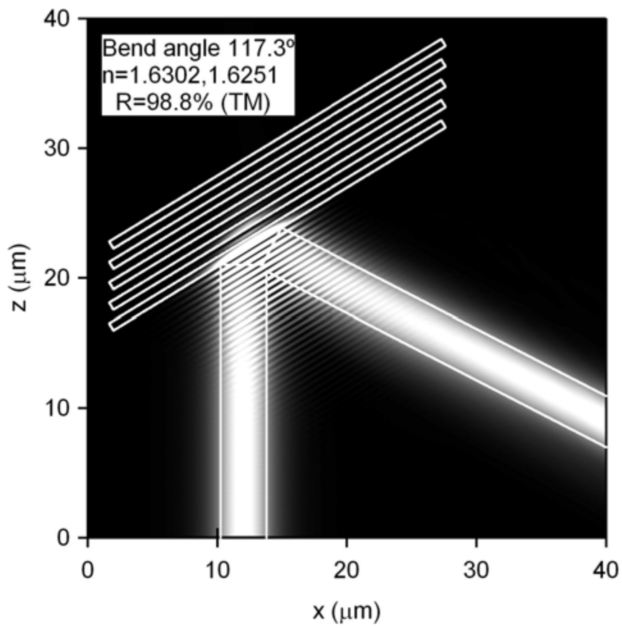

(a) TM

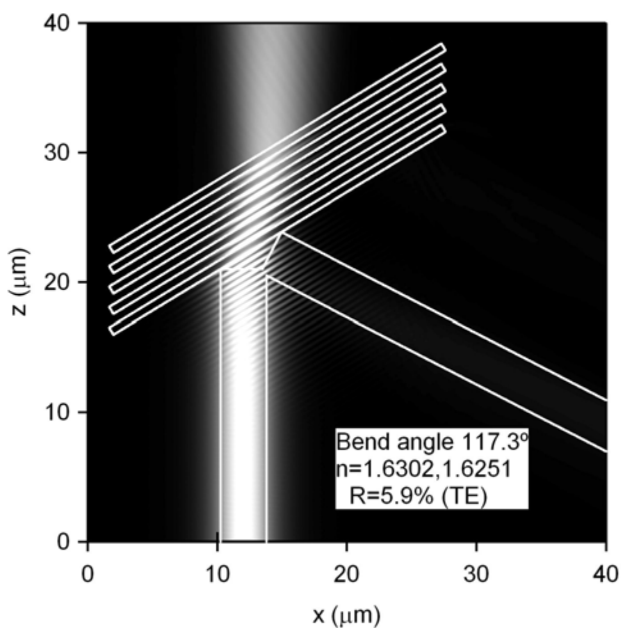

(b) TE

Figure 4.10 FDTD simulation of an air-trench Bragg mirror for Gyro waveguide

Figure 4.10 are the FDTD simulations for this 117.3° waveguide bend with the air Bragg mirror approach with FDTD grid size $\lambda_0/60$. Because of the Brewster angle incidence, this five-layer mirror achieves a high bend-efficiency (98.8% by MOI and 99% by power ratio) for TM light while very low efficiency (5.9%) for TE light. It is seen from Figure 4.10(b) that the TE light has mostly transmitted.

4.3 Bragg/Quasi-Bragg silicon waveguide 90° bends

Section 4.2 has designed a rigorous periodic Bragg mirror for the 117.3° Gyro waveguide bend with five air interlayers. As explained before, the reason to choose air is for the consideration of high index contrast and feasibility of fabrication. If just for the consideration of high index contrast, other material, for example, silicon (Si, n=3.4), is also a good alternative option. In this section, a Bragg mirror as a 90° waveguide bend with a stack of Si for the same waveguide as in Section 4.1 with core and cladding indices of n=1.5, 1.465 is examined.

This example also has a partial reflectance approximation, thus an analytical layer thickness can be calculated using Equation 4.1 with n_1=1.465, θ_1=45°, and n_2=3.4 at λ_0=1.55 μm. The alternate layer thicknesses are 0.37 μm and 0.12 μm for the cladding and Si layer, and it takes three alternate layers to achieve higher than 99% reflectivity theoretically for TM light.

Figure 4.11 is the 3-layer Si Bragg mirror as waveguide 90° bend with FDTD grid size $\lambda_0/100$. The relatively higher resolution is for accurate simulation for the small thickness dimension for the Si layer. The bend efficiency is 97.8% for the TM case, which is better than the multiple air-layer bends as in Section 4.1 (93%). Part of the reason can be that the multiple layers in Figure 4.11 work together to increase the partial reflectance for the entire waveguide mode, or all the plane-wave components, while the multiple-layer structures with air in Section 4.1 have to compensate for some TIR part while improving the partial reflectance part.

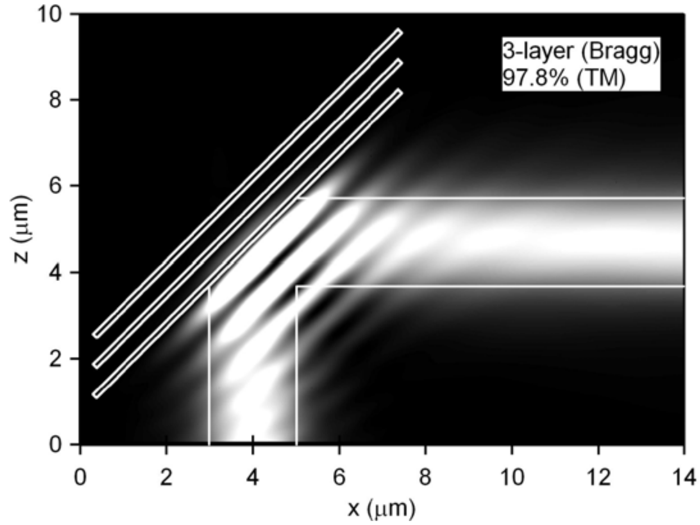

Figure 4.11 FDTD simulation of silicon Bragg mirror as a waveguide 90° bend

Figure 4.12 is the bend efficiency (calculated by power ratio without MOI) as a function of wavelength, and it is still a relatively flat curve over a range of 1.3 μm to 1.7 μm. Therefore this Si Bragg mirror is also not very sensitive to wavelength as the multiple air-layer bend is.

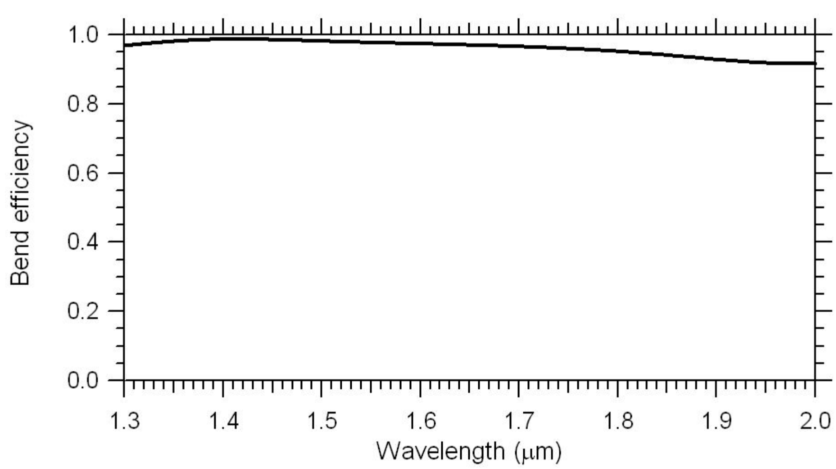

Figure 4.12 Bend efficiency dependence on wavelength for a Si Bragg mirror

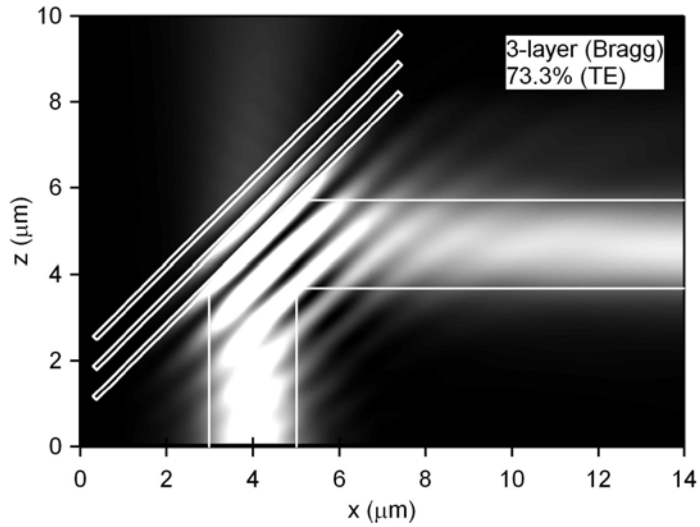

Figure 4.13 FDTD simulation of Si mirrors in Figure 4.12 (TE)

Figure 4.13 is the FDTD simulation with TE light for the same geometry as in Figure 4.11. The bend efficiency is not high, 73.3%. However, based on interference for stratified films, a more-layer structure is expected to give higher reflectance than a less-layer one is. Based on plane-wave approximation for TE light, a six-Si-layer structure can improve bend efficiency higher than 99%.

The top two figures in Figure 4.14 are the FDTD simulations for this 6-layer Si Bragg mirror with both TM and TE illuminations. It is seen that the bend efficiency for TE light has been improved approximately 13% from the 3-layer structure.

Applying μGA-FDTD to optimize this 6-layer structure for higher BE with TE light gives the two figures at bottom of Figure 4.14.

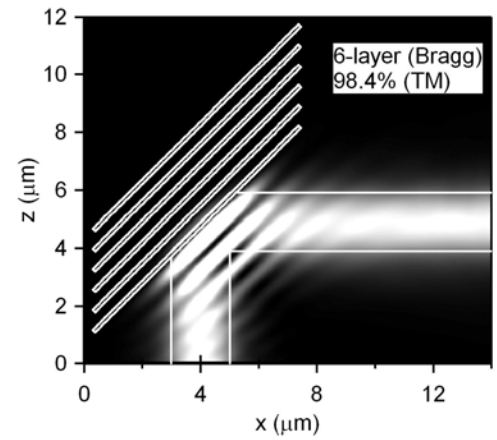

(a) Si Bragg mirror (TM)

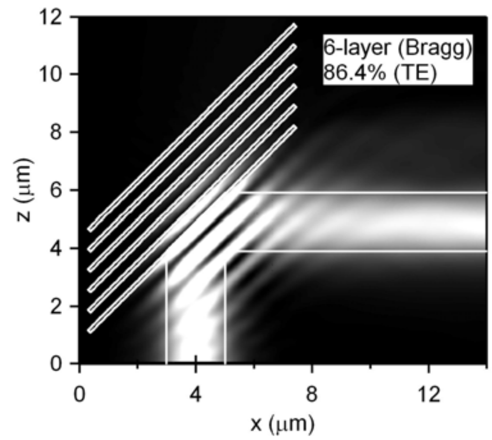

(b) Si Bragg mirror (TE)

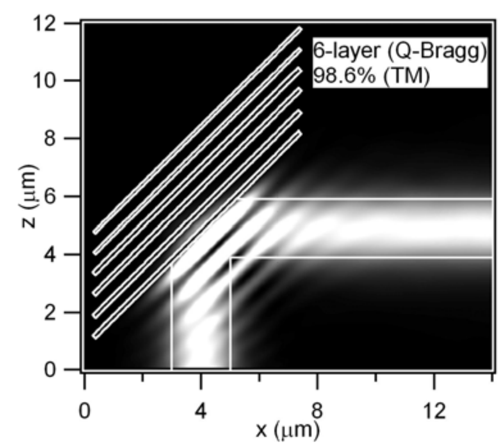

(c) Quasi-Bragg mirror (TM)

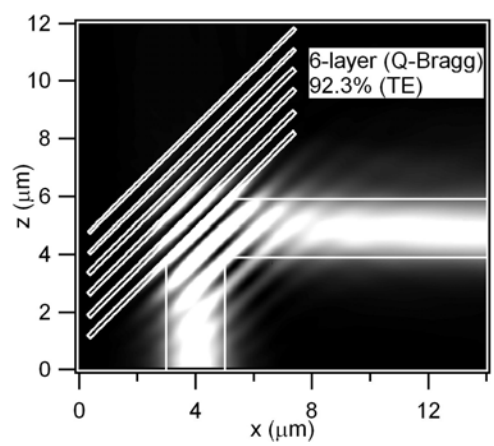

(d) Quasi-Bragg mirror (TE)

Figure 4.14 FDTD simulations of 6-layer Si mirrors

The optimized Quasi-Bragg mirror has slightly unequal Si layer thickness starting from the side close to waveguide, 0.149, 0.153, 0.145, 0.157, 0.114, 0.106, in the unit of μm. BE improvement about 6% from the rigorous periodic mirror has been achieved by μGA optimization. This again shows the powerfulness of μGA-FDTD design tool. The BE for TM stays essentially unchanged high for the three and six-layer Bragg or Quasi-Bragg mirrors. This again shows the wide thickness tolerance for the multiple-layer Si mirror just as the multiple-layer air-trench structures in Section 4.1.

Figure 4.15 is the bend efficiency (calculated by power ratio without MOI) as a function of wavelength for the 6-layer Si mirror. It is still a relatively flat curve over a range of 1.5 μm to 1.7 μm for TM light for both these 6-layer mirrors. For TE light, the 6-layer Bragg mirror does not have a flat range while the Quasi-Bragg mirror does have a flat range from 1.5 μm to 1.7 μm. This is another slightly favorite characteristic for this 6-layer Quasi-Bragg mirror besides having higher bend efficiency.

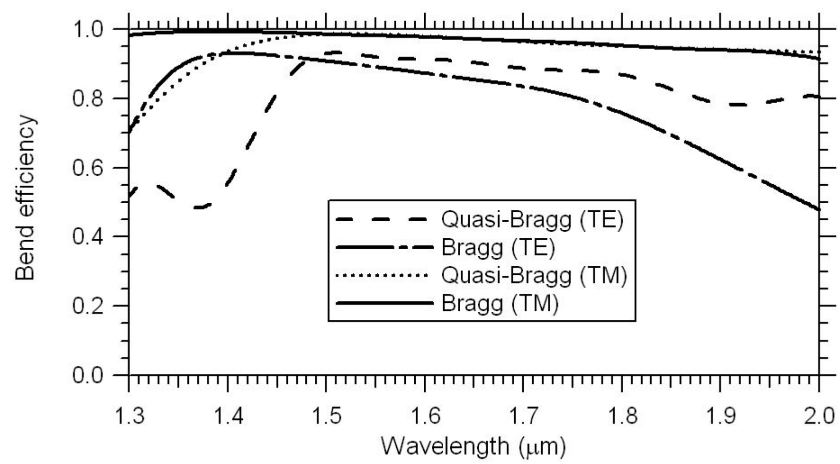

Figure 4.15 Bend efficiency dependence on wavelength for the 6-layer Si Bragg mirror in Figure 4.14

Overall, Chapter 4 has proposed and numerically simulated multiple-layer structures as waveguide bends. Bend efficiency can be effectively improved by using the multi-layer structures. Rigorous periodic Bragg mirrors can be analytically designed for bends with a partial reflection from a plane-wave approximation. High bend efficiency can be achieved for waveguide contrast at 2.4%, and it is expected to have further improvement for waveguides with lower-Δ because they are more close to plane-wave approximation. It has been shown that the μGA-FDTD design tool is very powerful in helping search for a good solution at situations without analytical guidance, or some other difficult conditions. One common feature for the multiple-layer air or silicon waveguide bends is that they have relatively flat wavelength response, which infers that they have relaxed thickness tolerance. This is because the phase difference forming the constructive interference from the neighboring layers is a function of wavelength and layer thickness for a fixed incident angle.

CHAPTER 5

AIR-TRENCH BEAMSPLITTERS

Chapters 3 and 4 present several approaches to realize compact high-efficiency waveguide bends by taking a panoramic view of a waveguide's angular spectrum. Inspired from the observed frustrated total internal reflection (FTIR) [76] phenomenon when designing the one-layer 90° bend in Section 4.1, amplitude beamsplitters are first designed in this chapter. This FTIR phenomenon has been widely used in bulk optics, for example, the prism coupler can couple light from a fiber or free space into a waveguide. The same phenomenon can also been used to create a waveguide beamsplitter with an air-gap as the separation medium [69]. Changing the air-gap thickness can vary the ratio of reflectance and transmittance. However, to make an even-ratio beamsplitter, it turns out that TE and TM light needs different air-gap thickness for the same waveguide as in Section 3.1. The second part of this chapter presents a design of a waveguide polarization beamsplitter for a Gyro project, which is based on two principles: (1) high-efficiency multiple-layer structure reflects TM light; (2) Brewster angle incidence transmits TE light. Combining these two, the TM and TE lights get split.

5.1 Air-trench amplitude beamsplitter

The amplitude beamsplitter designed in this section uses the same waveguide as in Section 3.1 with n=1.5, 1.465 and width 2 μm at wavelength λ_0=1.55 μm. Based on FTIR phenomenon, changing the air-gap thickness can get variable power ratio of reflection (R) and transmission (T). The design goal here is to get an even-ratio beamsplitter for both TM and TE light at a 90° crossing.

5.1.1 Air-trench amplitude beamsplitter (TM)

For a single air-gap FTIR beamsplitter, the air-gap thickness has the lowest limit of zero, then all the light will go through and no reflection, which represents T=1 and R=0. The highest limit is to have infinite gap thickness, which is close to the single air-interface 90° bend as simulated in Section 3.1, which has reflection R=78.4% (by power ratio). In the middle of these two limits with increasing gap thickness, the reflection generally gets higher while transmission gets lower. However, it is not a direct proportional relationship for the R and T with the air-layer thickness. Reflection for TM light achieves its highest, 85.7% (by power ratio), for an optimized thickness t=1.14 μm as simulated in Section 4.1.

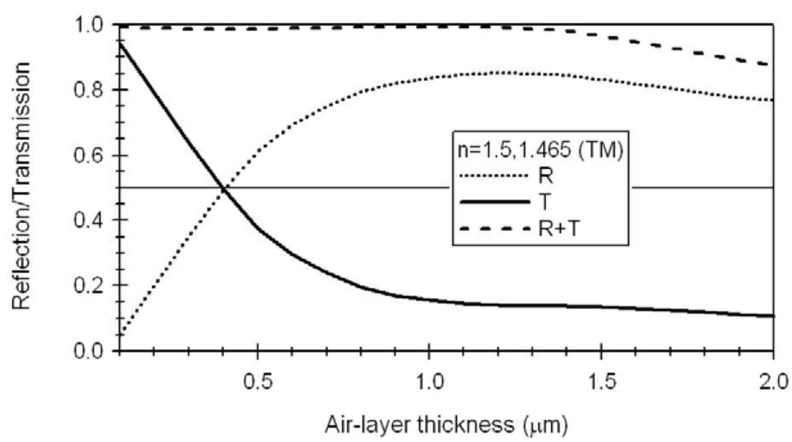

Figure 5.1 Reflection and Transmission vs. thickness of a single air layer (TM)

A quantitative relationship of R and T with the air-gap thickness for TM light is shown in Figure 5.1. This figure is attained after a series of FDTD simulations for the one air-layer 90° beamsplitter with different layer thickness by keeping the input and output waveguide unmoved. The maximum reflection occurs at thickness of t=1.0 μm approximately, which matches the optimized result (t=1.14 μm) as in Figure 4.2 (page 81). Also it is noticed that the total addition of R and T drops when the layer thickness gets greater than 1.5 μm. This can be understood that a thicker layer spreads the light due to the angular spectrum of the waveguide mode and thus some light gets lost and can't couple into either the refection or transmission arm.

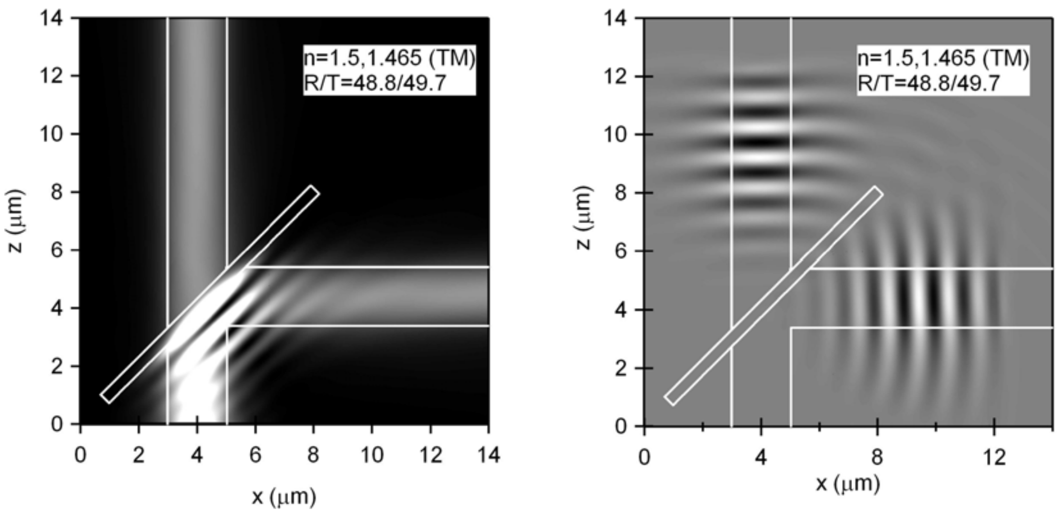

(a) with waveguide mode as a source

(b) with a pulse as a source

Figure 5.2 Even-ratio air-trench amplitude beamsplitter (TM)

It is shown in Figure 5.1 that a 50/50 beamsplitter can be achieved with an air thickness at around t=0.4 μm. This even-ratio amplitude beamsplitter for TM light is simulated as shown in Figure 5.2 with an actual air-trench thickness of 0.39μm and FDTD simulation grid size of $\lambda_0/80$. The actual power ratio of reflection over transmission is 48.8/49.7 (by power ratio). Figure 5.2(a) and (b) have the same geometry, but they use a different source. Figure 5.2(a) uses a continuous waveguide mode with a fixed wavelength λ_0=1.55μm as a source, while (b) uses a pulse of Δλ=0.36μm as its source and the plot is a time snap shot of square of the electrical field.

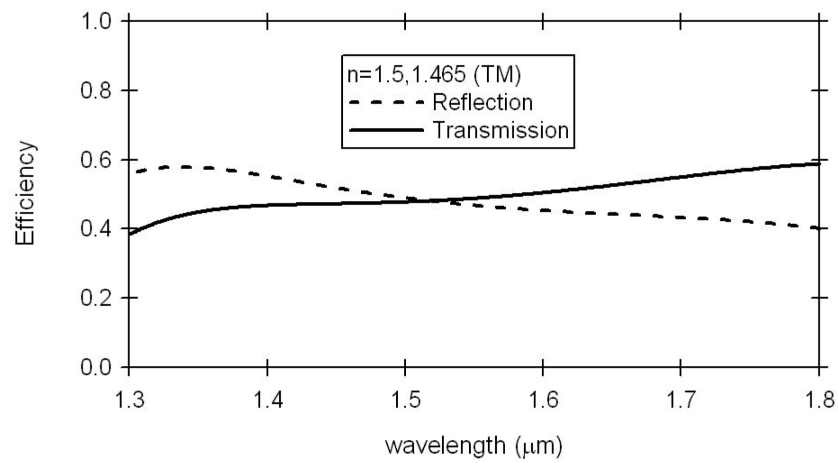

Figure 5.3 Air-trench amplitude beamsplitter spectrum response (TM)

With the pulse Δλ=0.36μm as a source, the spectrum response of the beamsplitter is generated as in Figure 5.3. It is seen that the reflection and transmission changes differently with the wavelength. Comparing Figure 5.3 with Figure 4.4 (page 83), the spectrum response for the one-layer bend, the beamsplitter is a little more sensitive to the wavelength than the one-layer bend is.

5.1.2 Air-trench amplitude beamsplitter (TE)

Following the same procedure as above by first doing a series of FDTD runs with different air-layer thicknesses, Figure 5.4 is generated for TE light, it turns out that a thickness close to 0.7 μm is needed for an even-ratio beamsplitter with TE light.

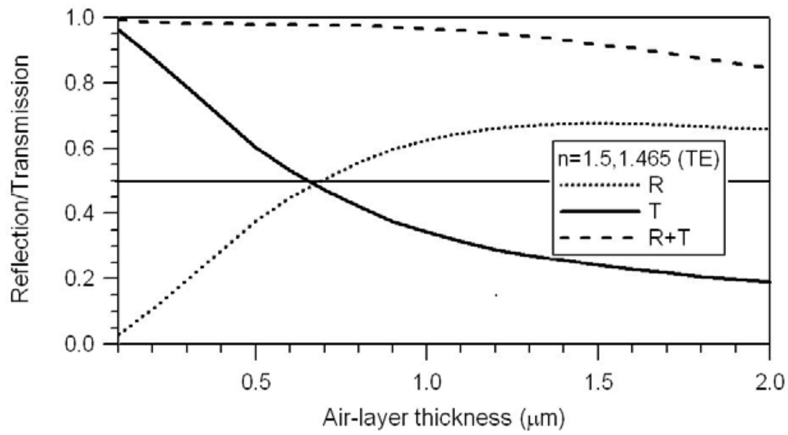

Figure 5.4 Reflection and Transmission changes with thickness of one air-layer (TE)

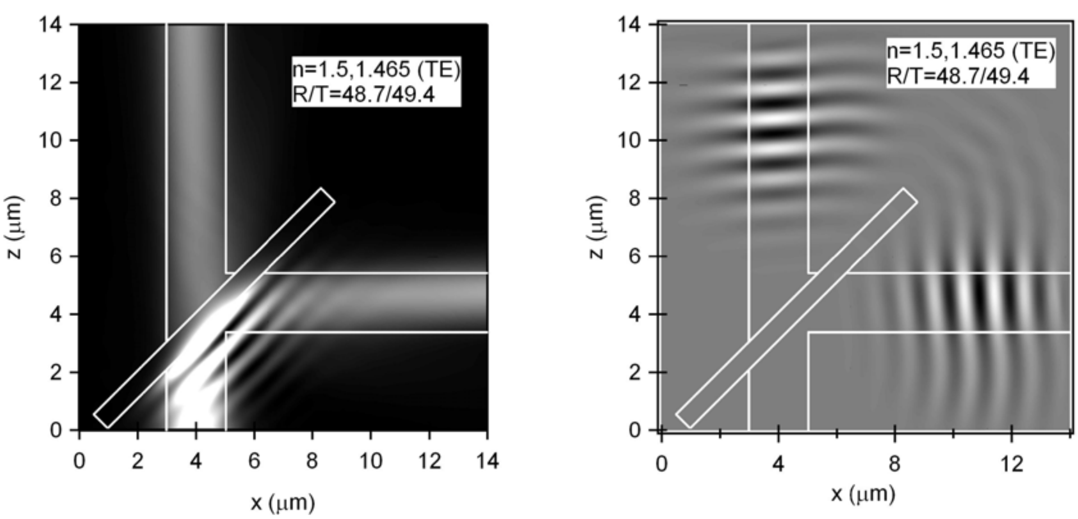

(a) with waveguide mode as a source

(b) with a pulse as a source

Figure 5.5 Even-ratio air-trench amplitude beamsplitter (TE)

FDTD simulation of the even-ratio amplitude beamsplitter for TE light is shown in Figure 5.5 with an actual air-trench thickness of 0.69 μm and FDTD grid size of $\lambda_0/80$. The actual power ratio of reflection over transmission is 48.7/49.4 (by power ratio). Figure 5.5(a) and (b) have the same geometry, but use a different source as in Figure 5.2.

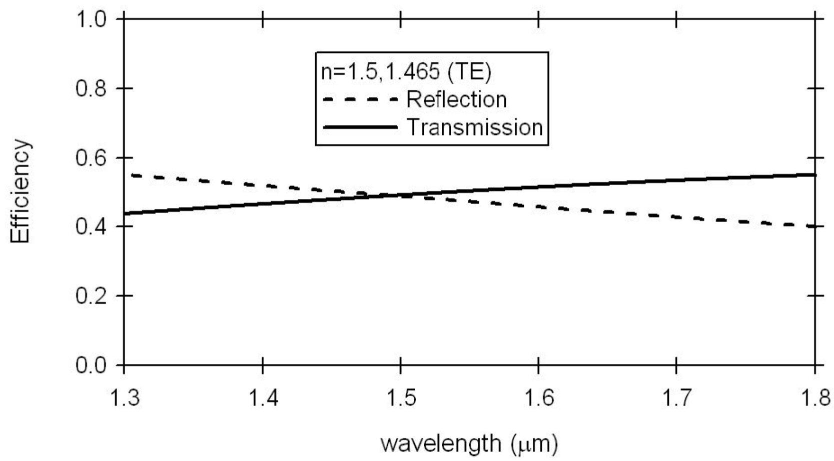

Figure 5.6 Air-trench amplitude beamsplitter spectrum response (TE)

With the same pulse of $\Delta\lambda$=0.36μm as a source as for Figure 5.3, the spectrum response of the beamsplitter for TE light is generated as in Figure 5.6. It can be seen that the reflection and transmission changes differently with the wavelength. Comparing Figure 5.6 with Figure 5.3, the spectrum response for TM and TE light has the similar pattern: the reflection gets lower with increasing wavelength while transmission changes oppositely.

5.2 Air-trench polarization beamsplitter

The scheme of designing a polarization beamsplitter (PBS) is totally different from the amplitude beamsplitter. It fully uses the high reflectance property for a multi-layer structure as in Section 4.3 while combining a Brewster angle incidence. With a special Brewster angle incidence, TE light should transmit through the multiple layers while TM light gets reflected in very high-efficiency, thus TE and TM polarizations get split.

A design example for this polarization beamsplitter (PBS) with a multi-layer structure is based on Gyro waveguide. The Gyro waveguide has core and cladding refractive indices of 1.6302 and 1.6251 for TM light and 1.6464 and 1.6414 for TE light, and width 3.5 μm to support its only fundamental mode at wavelength λ_0=1.33 μm. Because of the birefringence effect for the Gyro waveguide, the Brewster angle is decided by the waveguide' cladding refractive index seen by the TE light, which is n=1.6414. At an interface of such a waveguide system and air, the Brewster angle is approximately 31.35°. For such a Brewster angle incidence, the corresponding bend angle is 117.3°.

The Bragg mirror in Section 4.1 uses five alternative air layers to achieve bend efficiency of 98.8% for TM light. However, it is found that this five-layer structure degrades the transmittance for TE light. Part of the reason is because of the waveguide mode incidence. The Brewster angle 31.35° is calculated based on an approximation of a plane wave incidence. With an actual waveguide mode incidence, some of the plane-wave components decomposed from the mode have different incident angles from the Brewster angle, which will have both reflection and transmission at each mirror interface. The more layers the structure has, the reflection effect for TE light will be more severe. However, fewer layers will degrade the reflection for TM light. For a balance for TM and TE, the PBS here is chosen to have three air layers and the layer thicknesses are the same as the Bragg mirror in Section 4.2, which are 0.62 μm for the air layer and 0.72 μm for the cladding layer.

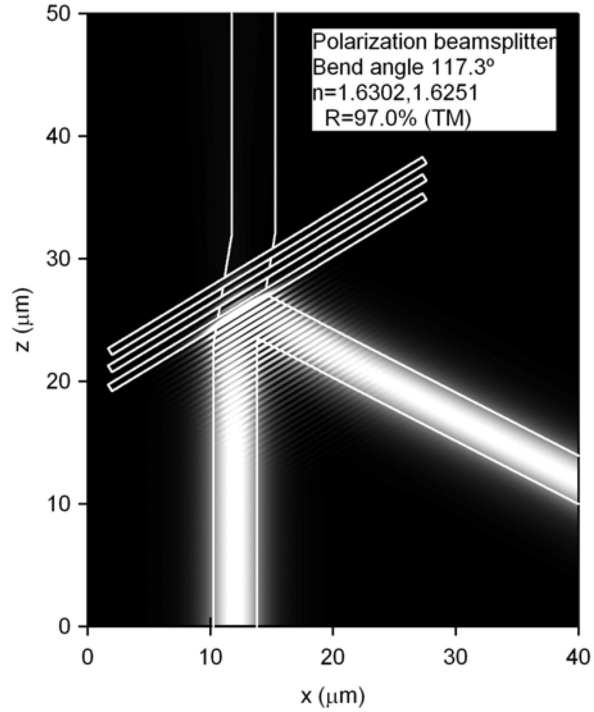

(a) reflection for TM light

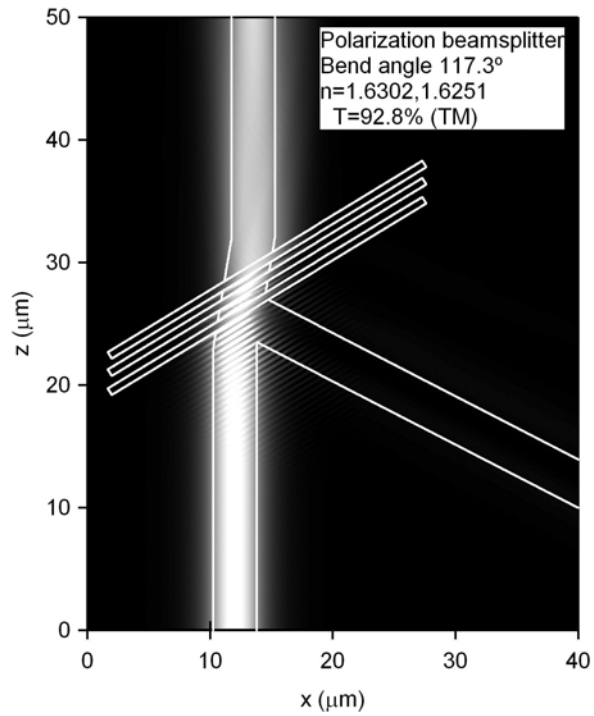

(b) transmission for TE light

Figure 5.7 FDTD simulation of an air-trench polarization beamsplitter for Gyro waveguide

Figure 5.7 is the FDTD simulation for this polarization beamsplitter with FDTD grid size of $\lambda_0/60$. The polarization splitting ratio of reflection (TM) over transmission (TE) is 97.0%/92.8% (by MOI), and 97%/96.0% (by power ratio). The reflections for TE and transmission for TM are 0.24% and 1.9% with MOI. This small numbers stand for cross-talk. It is observed that the field profile from the reflection path matches with the waveguide mode better than from the transmission path. Therefore the reflection is higher than the transmission, especially by MOI calculation.

This polarization beamsplitter, together with the air Bragg mirror designed in Section 4.2, are two critical components for the waveguide depolarizer given in Chapter 6. To have high performance it generally requires a polarization beamsplitter with balanced transmission and reflection.

CHAPTER 6

INTEGRATED DEPOLARIZER

For a system using intrinsically polarized light, such as most of the laser sources, the state of polarization generally will evolve in a random way during the propagation, as on the long single-mode optical fibers. The polarization change is a response to any environment changes, such as temperature, bending, inhomogeneity of the fiber itself. Most of the detectors are sensitive to the state of polarization, thus a noise from the random change of polarization may appear [77].

Specially for an Interferometric Fiber Optic Gyroscope (IFOG) system that needs long fiber coils as the sensing part, high performance is generally made by winding polarization maintaining (PM) fibers following a special procedure to remove the unwanted polarization-related noise. However, PM fibers are expensive. To avoid its high cost, inexpensive single mode (SM) fibers can be used instead. However, if polarized light enters a SM fiber coil, small variations, such as in temperature, stress, or vibration, will cause random birefringence changes, which will cause the polarization state to vary randomly. Because of this random variation, the beam's intensity, when measured after the polarizer, will vary to the point when the signal at times will drop all the way to zero. This phenomenon is called polarization fading. However, if a depolarizer is introduced before the fiber coils, these variations will not result in polarization fading. The function of a depolarizer is to change a polarized light to an unpolarized light, and the depolarized beam will have no definite polarization state. Therefore the random perturbations along the fibers can't cause a polarization change, thus polarization fading is avoided.

Some fiber-version depolarizers using fibers in meters have already been in use [78,79]. However, they are not in a compact form and are at high cost. In this chapter a waveguide-version depolarizer (called Gyro depolarizer) is proposed for a waveguide Gyro project, which means to make a low-cost waveguide Gyro system. The Gyro depolarizer needs to be designed compatible with other components developed by other groups for a Navy program. The components introduced in Chapters 4 and 5, the Bragg mirror and the polarization beamsplitter are used to compose this depolarizer, which are all in very compact form. Its working principle and overall performance will be presented in this chapter.

6.1 Depolarizer concept

A depolarizer is a device that transforms either completely or partially polarized light to an unpolarized light. To best describe the Gyro depolarizer approach in mathematics, it is better to start from Jones vectors and polarization ellipse together with Stokes vectors and Poincare sphere. Stokes vectors describe incoherent light and its intensity (coherent light is a special case of incoherent light), while Jones vectors describe only coherent light and its fields.

6.1.1 Jones vector and polarization ellipse for coherent light

For a monochromatic time-harmonic plane wave traveling in the z direction (coherent light), its electric field can be decomposed into x and y components as (shown in Figure 6.1)

$$\begin{aligned} E_x &= a_1 \cos(\tau + \delta_1) \\ E_y &= a_2 \cos(\tau + \delta_2) \end{aligned} , \tag{6.1}$$

where a_1 and a_2 are amplitude magnitudes in x and y directions, $\tau = \omega t - k \bullet r$ is the time-changing phase, and δ_1 and δ_2 are initial phase at x and y directions.

The phase difference δ is defined as $\delta = \delta_2 - \delta_1$.

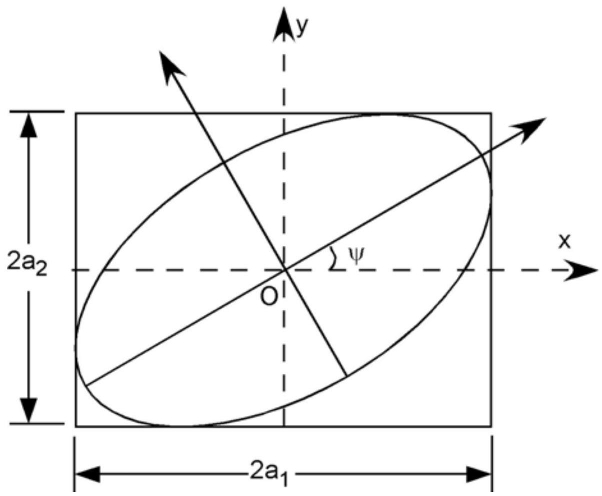

Figure 6.1 Polarization ellipse for coherent light

After eliminating τ of Equation 6.1, the ellipse function is left as

$$\left(\frac{E_x}{a_1}\right)^2 + \left(\frac{E_y}{a_2}\right)^2 - 2\left(\frac{E_x}{a_1}\right)\left(\frac{E_y}{a_2}\right)\cos\delta = \sin^2\delta \quad . \tag{6.2}$$

In general the ellipse axes are not in the Ox and Oy directions. Let Oξ (major) and Oη (minor) be a new set of axes along the ellipse axes and let ψ [0,π) be the angle between Ox and the major axis Oξ, then the components E_ξ and E_η are related to E_x and E_y by

$$E_\xi = E_x \cos\psi + E_y \sin\psi$$
$$E_\eta = -E_x \sin\psi + E_y \cos\psi \quad , \tag{6.3}$$

where ψ ($0 \le \psi < \pi$) is the orientation angle of the ellipse, which describes the separation between the Ox axis and the major axis Oξ, and

$$\tan 2\psi = \tan 2\alpha \sin\delta \ , \tag{6.4}$$

where angle α is defined as $\tan\alpha = \frac{a_2}{a_1}$.

The ellipse function for E_ξ and E_η is

$$\left(\frac{E_\xi}{a}\right)^2 + \left(\frac{E_\eta}{b}\right)^2 = 1 \ , \tag{6.5}$$

where a and b ($a \ge b$) are the half lengths along the elliptical axes Oξ and Oη. The quantities of a and b are related with a_1 and a_2 by

$$a^2 + b^2 = a_1{}^2 + a_2{}^2 \ . \tag{6.6}$$

The ellipticity χ ($-\pi/4 \le \chi \le \pi/4$) is defined as

$$\tan\chi = \pm\frac{b}{a} \ . \tag{6.7}$$

6.1.2 Stokes vectors and Poincare sphere for incoherent light

The Poincare sphere shown in Figure 6.2 is a powerful tool to express all kinds of polarization states. Going from the surface to the central point, the light goes from completely polarized to completely unpolarized. The equator stands for all linearly polarized light, while the top and bottom polar points are right and left handed polarized states, respectively. Between them, on the surface are all possible elliptically polarized states. Any incoherent light can be expressed as Stoke vectors ($(s_0 \quad s_1 \quad s_2 \quad s_3)^T$) (G.G. Stokes introduced in 1852 the four vectors), and Stokes vectors can be added together for incoherent light, just as adding Jones vectors for coherent light.

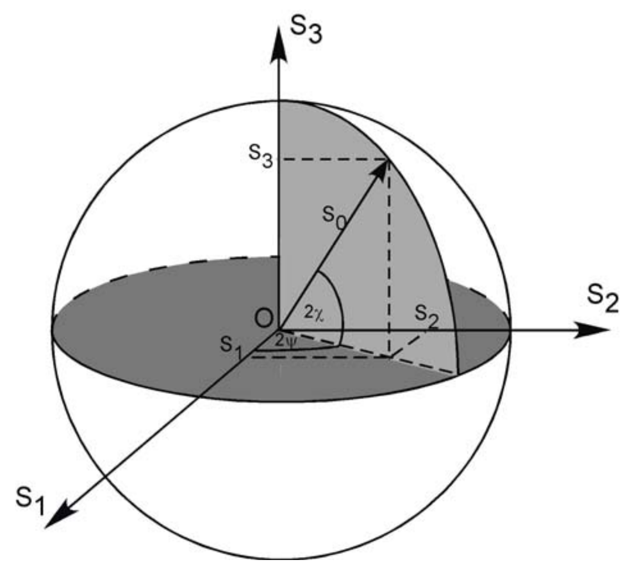

Figure 6.2 Poincare sphere for incoherent light

Using the same notation as in Figure 6.1, the Stokes parameters of a plane monochromatic wave (which is special coherent light) are

$$
\begin{aligned}
s_0 &= a_1^{\,2} + a_2^{\,2} \\
s_1 &= a_1^{\,2} - a_2^{\,2} \\
s_2 &= 2a_1 a_2 \cos\delta \\
s_3 &= 2a_1 a_2 \sin\delta
\end{aligned} \quad . \tag{6.8}
$$

Only three of them are independent and they are related by the identity

$$
s_0^{\,2} = s_1^{\,2} + s_2^{\,2} + s_3^{\,2} \quad . \tag{6.9}
$$

The parameter s_0 is proportional to the intensity of the wave. Equation 6.9 is especially true for a polarized light while it is generally $s_0^{\,2} > s_1^{\,2} + s_2^{\,2} + s_3^{\,2}$ for a partially polarized light. The other parameters are related to the orientation angle ψ of the ellipse and the ellipticity χ as

$$
\begin{aligned}
s_1 &= s_0 \cos 2\chi \cos 2\psi \\
s_2 &= s_0 \cos 2\chi \sin 2\psi \\
s_3 &= s_0 \sin 2\chi
\end{aligned} \quad . \tag{6.10}
$$

The two stokes vectors s_1 and s_2 are related by the orientation angle ψ as

$$
s_2 = s_1 \tan 2\psi \quad . \tag{6.11}
$$

6.1.3 Depolarizer concept expressed in Poincare sphere

As stated above, Stokes vectors can be added together for incoherent light. Thus adding two incoherent beams with equal intensity and orthogonal polarization together will result to be an unpolarized light [77]. To be general, the two parts are assumed to be both elliptically polarized, which can be expressed in the Poincare sphere as S_a and S_b vectors shown in Figure 6.3. When they meet incoherently, their Stokes vectors will add up and result to the central point of the sphere O, which stands for an unpolarized light. This is the basic design principle for the Gyro depolarizer.

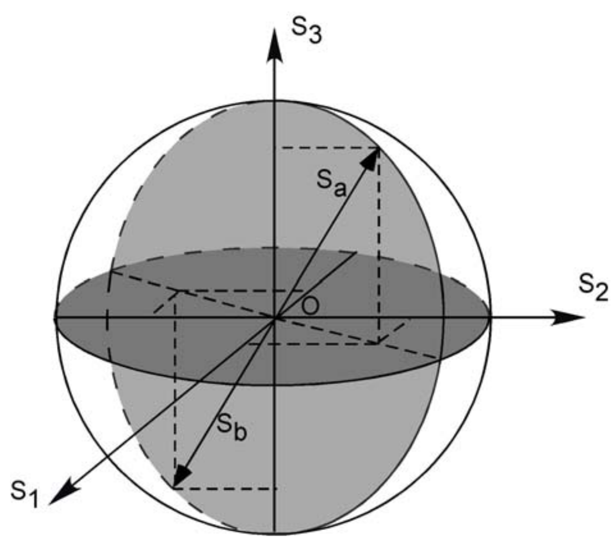

Figure 6.3 Depolarizer concept expressed in Poincare sphere

Degree of polarization (DoP) is used to describe the performance of a depolarizer. The smaller the DOP is, the better a depolarizer is. The Degree of Polarization (0≤DoP≤1) is defined with stokes parameters as

$$DoP = \frac{\sqrt{s_1{}^2 + s_2{}^2 + s_3{}^2}}{s_0} \quad . \tag{6.12}$$

$DoP = 1$ stands for a fully polarized light, which is on the surface of the sphere.

$DoP = 0$ stands for a fully unpolarized light, which means every component of s_1, s_2, and s_3 would be 0. That is the central point O at the Poincare sphere and its stokes vector is

$$s_o{}^T = [1 \quad 0 \quad 0 \quad 0]^T \quad . \tag{6.13}$$

An ideal depolarizer (with Muller matrix as in Equation 6.14) will change any incident polarization state to an unpolarized light, and such a depolarizer is an incident-state-independent depolarizer. The Gyro depolarizer is, however, an incident-state-dependent depolarizer.

$$\begin{bmatrix} 1 & 0 & 0 & 0 \\ 0 & 0 & 0 & 0 \\ 0 & 0 & 0 & 0 \\ 0 & 0 & 0 & 0 \end{bmatrix} \begin{bmatrix} s_0 \\ s_1 \\ s_2 \\ s_3 \end{bmatrix} = \begin{bmatrix} s_0 \\ 0 \\ 0 \\ 0 \end{bmatrix} \tag{6.14}$$

6.2 Depolarizer approach

In connection with other Gyro components, the incoming light for the Gyro depolarizer is TM polarized light. Based on the depolarizer concept explained above, the component layout of the Gyro depolarizer is illustrated in Figure 6.4. The TM incidence is first transformed half of its intensity to its orthogonal polarization by the polarization rotator. Then the TM and TE light gets split apart and combined back by two polarization beamsplitters after going through a path difference greater than the source's coherent length. When these two equal-intensity and incoherent light combine again, their Stokes vectors get added to generate an unpolarized light. At real situations, it is impossible to have a mirror of 100% reflection and a polarization beamsplitter of 100% reflection for TM and 100% transmission for TE light. However it should be pointed out that the critical point is at point E to have equal intensity of TE and TM light to have a better-performance depolarizer.

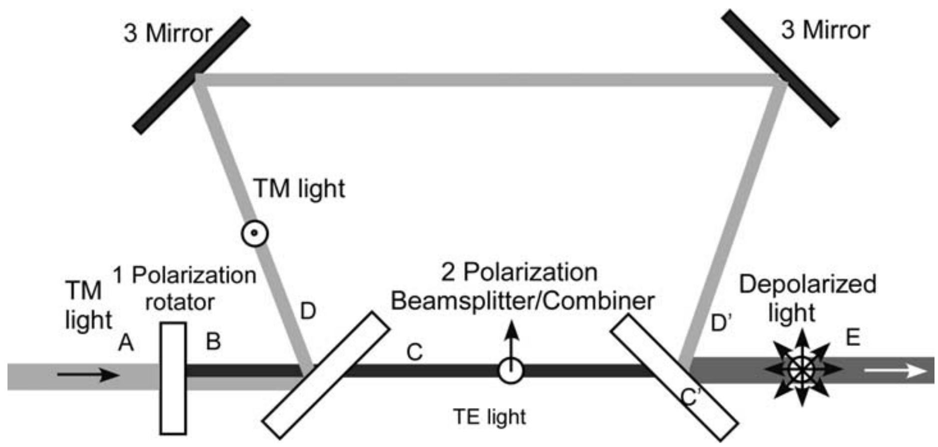

Figure 6.4 Component layout of the Gyro depolarizer approach

The Gyro depolarizer is required to work on both directions, where from left to right, the incidence is TM polarized light, and from right to left, the incidence is an unpolarized light coming from the fiber coils. To check how this depolarizer works in both ways, a detailed mathematical derivation is given in the following.

(1) When TM light goes from left to right (→)

The incident TM polarized light at point A can be expressed as Jones and Stokes vectors as

$$J_A = \begin{pmatrix} 1 \\ 0 \end{pmatrix}, \; S_A = \begin{pmatrix} 1 \\ 1 \\ 0 \\ 0 \end{pmatrix}. \tag{6.15}$$

Then the light comes through a polarization rotator which transforms the TM state to a state with equal-intensity TE and TM. Generally this state is elliptically polarized (with arbitrary phase difference δ). Specially it can be 45° linearly polarized light (with zero phase difference δ), or circularly polarized light (with phase difference δ= ±90°). Assuming an arbitrary phase difference δ, the Jones and Stokes vectors at point B become

$$J_B = \begin{pmatrix} \frac{1}{\sqrt{2}} \\ \frac{1}{\sqrt{2}} e^{j\delta} \end{pmatrix}, \; S_B = \begin{pmatrix} 1 \\ 0 \\ \cos\delta \\ \sin\delta \end{pmatrix}. \tag{6.16}$$

The polarization beamsplitter next reflects TM light while transmitting TE light, ideally at 100% for TM reflection and TE transmission. Thus after this component, the states at point C and D will be orthogonally different as

$$J_C = \begin{pmatrix} 0 \\ \frac{1}{\sqrt{2}} \end{pmatrix}, \; S_C = \begin{pmatrix} 1/2 \\ -1/2 \\ 0 \\ 0 \end{pmatrix}, \tag{6.17}$$

$$J_D = \begin{pmatrix} \frac{1}{\sqrt{2}} \\ 0 \end{pmatrix}, \; S_D = \begin{pmatrix} 1/2 \\ 1/2 \\ 0 \\ 0 \end{pmatrix}. \tag{6.18}$$

In the TM path, two mirrors will reflect ideally 100% of TM light without varying its polarization. A critical requirement is that the TM path should be long enough to make the path difference for TE and TM greater than the source's coherence length. Then TE and TM can incoherently meet at C' and D' points with a polarization state at E point as

$$S_E = S_{C'} + S_{D'} = \begin{pmatrix} 1/2 \\ -1/2 \\ 0 \\ 0 \end{pmatrix} + \begin{pmatrix} 1/2 \\ 1/2 \\ 0 \\ 0 \end{pmatrix} = \begin{pmatrix} 1 \\ 0 \\ 0 \\ 0 \end{pmatrix} . \tag{6.19}$$

The Stokes vectors for the output light at E point will be a completely depolarized light at ideal condition.

(2) When unpolarized light goes from right to left (←)

For application of the Gyro depolarizer at its opposite direction, the light source comes from the fiber coils, which will still be the depolarized light inputting to the coils. The depolarizer function for this direction should be keeping the light depolarized. The right-side polarization beamsplitter will spit the depolarized light to TE and TM polarized light; however, their phase difference is still arbitrary. When they combine after the left-side polarization beamsplitter, it will recover back to an unpolarized light at point B. The rotator would leave the polarization unchanged for an unpolarized light. Therefore for an unpolarized incidence from right to left, the depolarizer keeps its unpolarized nature.

Together this depolarizer approach is expected to work for both directions.

6.3 Waveguide implementation

As stated before, the Gyro project is meant to make a waveguide-version Gyro system in a very robust and compact form. To be compatible with other subsystems from other groups, the Gyro depolarizer uses the same waveguide material system. The waveguide is given to be a ridge waveguide in 3D, and can be transformed to a 2D slab waveguide by using the Effective Index Method (EIM). Detailed information about this transformation has been given in Section 2.3.3. The transformed 2D waveguide has width 3.5 μm to support its only fundamental mode at wavelength λ_0 =1.33 μm, and refractive index 1.6302 and 1.6251 for TM light and 1.6464 and 1.6414 for TE light.

The main components as shown in Figure 6.4 are the polarization rotator, two identical polarization beamsplitters (PBS) and two identical mirrors. This dissertation focuses on the design of the latter two components while another graduate student Jinbo Cai is working on the rotator design. Detailed design and simulation for the waveguide mirrors and polarization beamsplitters have been given in Section 4.2 and Section 5.2 with air-trench multilayer structures. Table 6.1 lists their performance for both TM and TE light incidences.

Table 6.1 Component performance of waveguide depolarizer

Component	**TM (Reflection)**		**TE (Transmission)**	
	by MOI	**by Power ratio**	**by MOI**	**by Power ratio**
Mirror	98.8%	99.0%	---	---
PBS	97.0%	97.0%	92.4%	96.0%

Based on Table 6.1, the DoP value and power loss of the Gyro depolarizer can be approximately calculated. First, the intensity at point C' for TE and D' for TM light can be calculated as

$$I_{C'} = \frac{1}{2} \times 0.924 \times 0.924 = 0.4269 \ ,$$

$$I_{D'} = \frac{1}{2} \times 0.97 \times 0.988^2 \times 0.97 = 0.4592 \ .$$

Then the Stokes vectors at C', D' and E points will be the follows from Equation 6.19

$$S_{C'} = \begin{bmatrix} 0.4269 & -0.4269 & 0 & 0 \end{bmatrix}^T \ ,$$

$$S_{D'} = \begin{bmatrix} 0.4592 & 0.4592 & 0 & 0 \end{bmatrix}^T \ ,$$

$$S_E = S_{C'} + S_{D'} = \begin{bmatrix} 0.8861 & 0.0323 & 0 & 0 \end{bmatrix}^T \ .$$

The DoP value of the Gyro depolarizer can be calculated based on Equation 6.12 as

$$DoP = \frac{0.0323}{0.8861} = 0.0365 = -14.4dB \ .$$

The power through-out of this depolarizer is 0.8861, which is an addition of $I_{C'}$ and $I_{D'}$. This is equivalent to loss=0.525 dB.

Both DoP and power loss exceeds the requirement for the Gyro depolarizer, which is 0.05 (-13 dB) and 1 dB respectively. However the above calculation is approximate. In a real situation, the rotator will take some power budget; cross leaking of TM and TE light and misalignment of the whole system will degrade the depolarizer's performance. From Table 6.1

and above DoP and power loss calculation, it is the transmission of the polarization beamsplitter (92.4% by MOI) that is relatively poor, which degrades both the power through-out and the DoP. Originally using the numbers calculated by the power ratio method as in Table 6.1, the DoP and power through-out would be 0.000325 (-34.9 dB) and 0.9216 (0.353 dB), which is extremely good. This mainly benefits from the balanced T and R for the PBS, 97%/96%. Therefore improving the transmission of the polarization beamsplitters to get a balanced TE and TM will be one effective way to improve the depolarizer's performance if needed.

6.4 Experimental demonstration with bulk optical components

To test the performance of the Gyro depolarizer before its waveguide components get fabricated, a benchtop experiment was setup with bulk optical elements with similar performance as its waveguide counterparts. A schematic diagram of the setup is shown in Figure 6.5. The polarizing beamsplitter (PBS) specifications for TE transmission, T_p, and TM reflection, R_s are T_p>96% and R_s>98%, respectively. The mirror reflectance is R>99.8%.

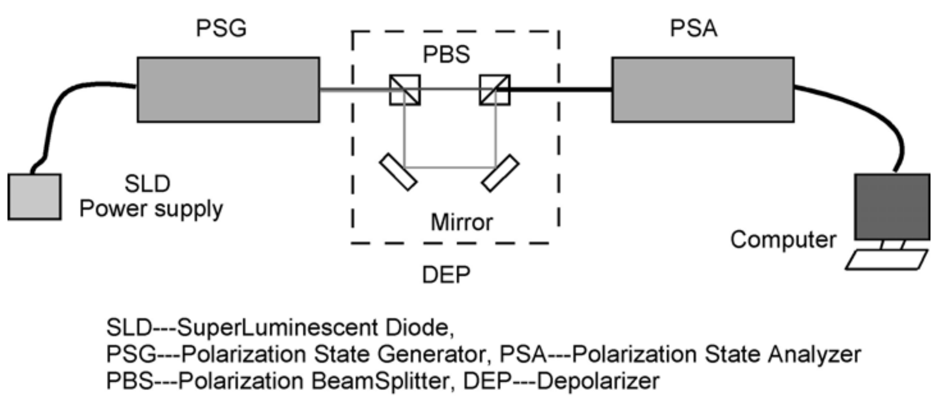

Figure 6.5 A benchtop arrangement for testing a bulk-version Gyro depolarizer

The optical source is a Superluminescent Diode (SLD) (model SLD-1310) from *Fermionics Lasertech* with an output power of 0.3 mW (-5.23 dBm). Figure 6.6 shows the SLD's power spectrum measured with an *ANDO* optical spectrum analyzer (AQ-6315E). The center wavelength is approximately 1330 nm and the full width half maximum (FWHM) spectral width is 53.3nm and so its coherence length is 33 μm. The path difference between the R and T paths in the depolarizer is about 10 cm, which is far greater than the coherence length of the source.

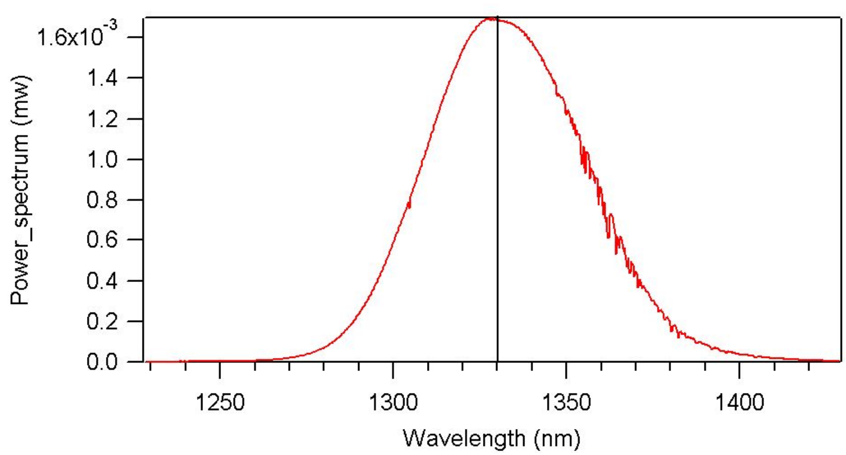

Figure 6.6 SLD (SuperLuminescent Diode) scanned spectrum

The depolarizer is mounted between the polarization state generator (PSG) and polarization state analyzer (PSA) of a polarimeter, which is an automatic dual-rotating-retarder Mueller Matrix Polarimeter (*Axometrics*) to measure polarization characteristics of the depolarizer. Accurate measurements depend upon careful alignment of the R and T beam paths to ensure colinearity of the output beams from each path.

To obtain equal-intensity TE and TM components at the output of the depolarizer, the input polarization state to the depolarizer from the source is set to 48° linear polarization to compensate the small amount of unequal T_p and R_s (T_p<R_s). The experiments have been arranged to test three configurations: (1) T path only, (2) R path only, and (3) Combined T and R paths. For the first two cases the DoP values are expected to be close to 1 while the DoP should be very close to zero for the third.

Experimental results are listed in Table 6.2. For the first two cases, the output DoP is very close to one, indicating that the light is highly polarized as expected. For the third case, the DoP is 0.002 (-27.0 dB), which means the light has been well depolarized. Note that the insertion loss for the depolarizer is quite small at 0.079 dB and that the insertion loss for the T only and R only paths is 3dB as one would expect.

Table 6.2 Measurement results of the bulk-version Gyro depolarizer

Configurations	Output DoP	Out DoP (dB)	Out T	Insertion Loss (dB)
T only	0.980	-0.088	0.497	3.054
R only	0.993	-0.03	0.491	3.076
R&T	0.002	-27.0	0.982	0.079

Based on the experimental measurements, the Mueller matrix for this bulk-version Gyro depolarizer (R&T configuration) is

$$M_{RT} = \begin{bmatrix} 0.982 & 0 & 0 & 0 \\ -0.002 & 0.957 & 0.104 & -0.006 \\ 0 & 0.0114 & 0.012 & 0 \\ 0.004 & 0 & 0 & 0 \end{bmatrix}.$$

This is close to the ideal Mueller matrix for depolarizing a beam with equal TE and TM polarization components, which is given by

$$M_{RT}^{ideal} = \begin{bmatrix} 1 & 0 & 0 & 0 \\ 0 & 1 & 0 & 0 \\ 0 & 0 & 0 & 0 \\ 0 & 0 & 0 & 0 \end{bmatrix}.$$

Obviously this Gyro depolarizer is an incident-dependent depolarizer, which is different from the Mueller matrix in Equation 6.14 (page 113). The upper left-hand element of the measured matrix, M_{RT}, 0.982, is the total transmission for the depolarizer (T and R configuration), which is exactly the same as the Output T in Table 6.2 for the R&T configuration. The four numbers in the central 2×2 matrix $\begin{bmatrix} 0.957 & 0.104 \\ 0.0114 & 0.012 \end{bmatrix}$ of M_{RT} represent a 3° diattenuation for the T only path. The other nonzero matrix elements are all very small and represent slight non-idealities of the depolarizer together with measurement noise.

This experiment shows that the DoP can achieve up to 0.002 (-27 dB) with component properties as explained above, and the power through-out can be 0.982 (Loss= 0.079 dB).

CHAPTER 7

CONCLUSION AND DISCUSSION

This dissertation focuses on the design and simulation of compact waveguide components, bends and beamsplitters. Single air-interface waveguide bends with different bend angles have been designed for several waveguide material systems. In the meantime waveguide mode plane wave expansion theory has been explored in a panoramic view to explain the bend's performance. Among all the approaches presented in this dissertation, multi-layer bends and beamsplitters are originally proposed in this dissertation, which includes Bragg and Quasi-Bragg mirrors. Besides component designs, as an application example, a waveguide depolarizer, has been designed using some of the above components. Since waveguide bends and beamsplitters are very basic components in the integrated optics regime, a wide range of applications can be found, and some of them will be mentioned in the recommendation section in this chapter.

7.1 Summary

This dissertation belongs to practical application type. It has lots of design and simulation figures for waveguide bends, beamsplitters. However, the designs of these waveguide components are all based on theories, basically from physics optics, which involves reflection, transmission, interference, and polarization.

The design of waveguide bends is based on reflection and transmission, and improving bend efficiency is actually equivalent to improving power reflectivity. Balancing the ratio of reflection and transmission is the basis for designing an amplitude beamsplitter. However, all these components are designed not for a simple single plane wave, but for some waveguide mode. The waveguide mode nature makes all these designs not so straightforward.

The finite-size waveguide mode can be looked as an infinite range of plane-wave components from a waveguide mode plane wave expansion theory. Therefore the design of bends and beamsplitters has to deal with all these plane-wave components that are propagating in slightly different directions and in slightly different mediums. For some waveguide systems, part of the plane-wave components have incident angles greater than a critical angle, and this part will have total internal reflection (TIR) (100% reflection); the other part has different partial reflection for different plane-wave components. This complicated situation is faced basically in Chapters 3 and 4 for all the bend structures. Chapter 3 proposes several approaches for improving bend efficiency based on understanding the angular spectrum in a panoramic view. Using smaller bend angles or smaller index-contrast waveguide material system can make more plane-wave components have TIR. To evaluate the approaches proposed in Section 3.3 experimentally and explore the usage of polymer material, the bends designed in Section 3.6 have been fabricated on some polymer waveguide. Extensive laboratory tests are at present under way.

The approaches proposed in Chapter 4 are directly working on improving the reflectance for the part having partial reflection by using multilayer structures. The multilayer structures utilize constructive interference to provide high power reflectivity. The quarterwave-thickness periodic Bragg mirrors can work well as waveguide bends for a waveguide mode incidence having partial reflection approximation. However for situations with a TIR plane-wave approximation but still having low overall bend efficiency due to partial reflection from a large part of the plane-wave components, there is no analytical guidance for the geometry of a Bragg mirror. Improving the bend efficiency for this tough situation initially needs our powerful tool, μGA-FDTD, to find an optimal geometry for a multi-layer structure. The multilayer structures work on the full spectrum of the waveguide mode and it has to compensate the frustrated TIR (FTIR) due to the finite thickness of the first layer. The optimized multilayer structures given by the μGA-FDTD are generally not rigorous periodic structures; however, it is found later that some periodic structure works well too for this tough situation. This indicates that there is a wide latitude of geometries for the multi-layer structures that can have similar high performance. The relatively flat spectrum response for the multilayer structures in Chapter 4 is the basic support for this indication. However, direct support is a relationship of bend efficiency as a function of layer thickness change, which needs further more FDTD runs.

This dissertation treats the optical electromagnetic fields in vector form. The light's polarization state plays a big factor on the design of waveguide components and the depolarizer device. For the bends and amplitude beamsplitters, separate designs and simulations have been done for each polarization, TE and TM. One important phenomenon involved in bend designs is the Goos-Hanchen (G-H) shift related to the total internal reflection for a finite-size beam. Different polarizations produce different G-H shifts generally, the optimal bend geometry in Chapter 3 has given preference for TM light for each single bend case. For the design of polarization beamsplitters, the Brewster phenomenon has been applied to combine with high-reflectivity multilayer bends to split the TM and TE light. Finally the design of the waveguide depolarizer heavily involves the light's polarization state. Jones ellipse and Poincare sphere, Jones vectors and Stokes vectors, are reviewed to help explain the depolarizer concept. The waveguide depolarizer is one application example for our simple bend and beamsplitter structures.

In the process of designing waveguide components, some related techniques have been reviewed and investigated in detail. The mode overlap integral (MOI) method has been used to calculate the bend efficiency, and detailed derivation and explanation have been accomplished in this dissertation, which, however, is not available from any literature. A graphic explanation about how to transform from a 3D waveguide to a 2D slab waveguide using the effective index method (EIM) is given in Section 2.3.3. Through so many designs in this dissertation, the application of FDTD and μGA-FDTD tools have been expanded considerably.

Finally, besides all the computer work for the design and simulations, some laboratory experiments are performed to test the Gyro depolarizer's performance. This benchtop experiment has shown low degree of polarization (DoP) and low power loss can be achieved by using similar-performance bulk-version optical elements replacing their waveguide counterparts.

7.2 Recommendations for future research

Extensive designs of waveguide bends and beamsplitters have been accomplished in this dissertation. One application example, a waveguide depolarizer has been designed using some of the waveguide components. However, these components are such basic elements for the integrated optics regime, a wide latitude of applications should exist and are worth exploring. Besides, along designing these waveguide components, there are still some unsolved and interesting problems that are worth working on further. This section will address these issues to conclude this dissertation.

Direction change is a very basic need for a simple waveguide device or a complicated planar integrated circuit. Approaches for high-efficiency waveguide bends and variable-ratio beamsplitters with different bend angles and for different material systems have been proposed in this dissertation. Further applications for these components can be anywhere with a need of direction change.

One special example can be a waveguide-version Fresnel's rhomb [75], which is essentially a phase-shifter. A phase shifter with linear phase shift of $\pi/2$ or π is practically the most important one because it allows any state of polarization be created out of the linear states of polarization [77]. One simple way to make these components in macro optics is using isotropic materials in total reflection [75]. The use of vitreous reflections at the separation surface of two different isotopic media makes the most of the properties concerning the phase states of TE and TM polarization in total reflection. Traditional Fresnel's rhomb has a parallelogram configuration made of a block glass of n=1.51, and with a specific interior angle of 54°37′. A 90° phase difference between TM and TE is attained by two total internal reflections (TIR) where each reflection generates a 45° phase difference. Thus a linearly 45° polarized light incident from air can be transformed to a circularly polarized light by this Fresnel' rhomb.

A waveguide version of Fresnel's rhomb can be easily realized on a waveguide having effective index of 1.51 and with two single air-interface bends of 54°37′. However, a different waveguide material may be used, which may need a different bend angle. Combining two of such Fresnel's rhombs in row, a π phase-shifter can be easily composed. These devices are in principle simple and have a non-negligible advantage----quasi-achromatism. Nevertheless, to achieve some phase shift based on TIR phenomenon, it requires the incident light have a special polarization state, which sometimes can be hard to achieve for a waveguide-version phase-shifter.

More examples can be as follows. Traditional S bends can be redesigned to Z bends, which can be applied to the in and out arms of a n×n coupler. Bends and beamsplitters can be easily combined to construct a ring, which can function as a resonator, or a Mach-Zehnder (MZ) interferometer. Complicated devices, such as an arrayed waveguide grating (AWG) multiplexer, may be composed by these basic bends and beamsplitters. Active devices, such as switches, may be made from some transformation of these components by adding some extra power source.

During the development process of the waveguide components in this dissertation, there are interesting problems occurring along the way. Some of them have been addressed in this dissertation while some of them need further future explorations.

Regarding the waveguide bends, the main focus of this dissertation is on low-index and low-Δ waveguides; however, it is worthwhile to investigate how the multi-layer structures work for other materials, such as high-index and high-Δ waveguides. From the literature the bend efficiency for an actual fabricated high-index and high-Δ waveguide mirror bends is still not very high although analysis or numerical simulation expects super high numbers. And it is also expected that the multiple-layer structures may work better for lower-Δ waveguides than 2.4% as used in this dissertation.

As introduced in Section 2.2, three factors contribute to the bend loss: pure radiation loss, transition loss between the straight and the bent waveguide, and the phase constant of the propagating field. Among them radiation loss is the most significant one, thus the approaches proposed in this dissertation mainly focus on decreasing radiation loss and improving power reflectivity. However, the transition loss and phase change will become critical when further improvement is desired for an already high-efficiency bend. Some phase compensators can be considered to compensate the small phase distortions from the reflections at the bend area for the waveguide mode by either inserting in the output waveguide path or along the reflecting surfaces. Curved reflecting surfaces have been applied in some switch structures [80] to improve the reflection effect for a waveguide mode, it will be worthy to explore further its application and combination with the bend structures presented in this dissertation.

It is found in Section 4.1 that a mirror with a periodic structure (3-layer Bragg mirror) can work as well as an optimized structure can. However, it needs more FDTD runs to prove directly that a wide latitude of geometries exist for that waveguide 90° bend. This will need a relationship of bend efficiency as a function of layer thickness change.

For the waveguide component application example, the integrated depolarizer, this dissertation has proposed the design concept and accomplished initial waveguide component designs. However, as a small functional system, the depolarizer needs more simulations at the system level for its overall performance. Further simulation works may include tolerance analysis for the system, alignment analysis, and 3D simulations. All these simulations involve big-size heavy computations, which will highly depend on cluster-based super computers. Besides that, further research can focus on improving the transmission for the polarization beamsplitter to improve the depolarizer's performance.

APPENDICES

APPENDIX A

MATLAB M FILE FOR CALCULATING BEND EFFICIENCY BASED ON WAVEGUIDE MODE PLANE WAVE EXPANSION THEORY

```
%The following program named Pwr_Ref_singangl.m calculates power reflectance based
% on waveguide-mode plane-wave expansion theory, waveguide mode theory, and Fresnel' law
% This program runs at Matlab 6.5
% TE refers to Ey polarized out of plane (TM in this dissertation)
%TM refers to Ex polarized in plane (TE in this dissertation)

% Waveguide geometry
wg_width =2;
core_index = 1.5;
clad_index1 =1.465;
clad_index2 =1.465;
lam= 1.55;

incident_angle =45*pi/180;   %90° bend with 45° incident angle in unit of radians
k0=2*pi/lam;
m=0;                   % waveguide mode number
dx = 0.019375;       %sampling size
N=2000;            % total sampling numbers for the waveguide mode
x0=dx*N/2;       %center of waveguide mode
start_id = 1;

DFT_size = N;       % DFT(Discrete Fourier transform)
delta_kx = 2*pi/(DFT_size*dx);    % sampling size in kx domain
kx =(-DFT_size/2:DFT_size/2-1)*delta_kx;

% Solving Maxwell equations to get analytical mode by
% loading function named TE_guide_mode()

[n_eff_TE, x_pos, Ey_TE_mode, Hx_TE_mode] = TE_guide_mode(wg_width,
core_index,clad_index1,clad_index2, lam,m,N,x0,dx, start_id);

power_TE = -0.5*Ey_TE_mode.* Hx_TE_mode; %get a power distribution
%plot(x_pos, Ey_TE_mode)
```

```
%plot(x_pos, power_TE)
mode_total_power =sum(power_TE)*dx;    % get total power

% Calculate equivalent medium n for each kx plane
n_eff_TE_fft = sqrt(kx.*kx/k0/k0+ n_eff_TE*n_eff_TE);

Kz= n_eff_TE*k0;   %Kz is the propagation constant
theta_critical=asin(1/n_eff_TE);
% Calculate incident angle for each plane wave component
theta_kx=incident_angle+atan(kx/Kz);
%Fresnel' equation
Rs_fld_kx=(cos(theta_kx)-sqrt((1./n_eff_TE_fft).^2-(sin(theta_kx)).^2))./ ...
    (cos(theta_kx)+sqrt((1./n_eff_TE_fft).^2-(sin(theta_kx)).^2));
% “space+…” is the row change sign

% Calculate power reflectance by summation of each reflection
%theta_kx_tran=theta_kx(theta_kx<theta_critical & theta_kx>=0);
% Snell's Law for theta2_kx
%theta2_kx=asin(n_eff_TE*sin(theta_kx_tran));
% Fresnel formula
%t_kx=(2*n_eff_TE*cos(theta_kx_tran))./(n_eff_TE*cos(theta_kx_tran)+ …
cos(theta2_kx));
%T_power_kx= (cos(theta2_kx)./(n_eff_TE*cos(theta_kx_tran))).*abs(t_kx).^2;
%power_reflect_TE=1-sum(T_power_kx.*Ey_TE_mode_FFT_amp_2(theta_kx<
%   theta_critical&theta_kx>=0))/sum(Ey_TE_mode_FFT_amp_2);

% Get Ey(kx) by Fourier transform
FFT_in =zeros(1, DFT_size);
%FFT_in(DFT_size/2-N/2:DFT_size/2-N/2+N-1) = Ey_TE_mode;
FFT_in = Ey_TE_mode;
% Now do FFT on the mode profile
Ey_TE_mode_FFT  = fft(FFT_in, DFT_size);
Ey_TE_mode_FFT = fftshift(Ey_TE_mode_FFT);
%Ey_TE_mode_FFT_amp = abs(Ey_TE_mode_FFT)/max(Ey_TE_mode_FFT);
Ey_TE_mode_FFT_amp = abs(Ey_TE_mode_FFT);
% get power distribution along kx
Ey_TE_mode_FFT_amp_2= Ey_TE_mode_FFT_amp.* Ey_TE_mode_FFT_amp;

% get reflected field Er(kx)
%Real_Er_TE_kx=Ey_TE_mode_FFT_amp.*real(Rs_fld_kx);
%Imag_Er_TE_kx=Ey_TE_mode_FFT_amp.*imag(Rs_fld_kx);
Er_TE_kx=Ey_TE_mode_FFT_amp.*Rs_fld_kx;       % Er(kx) is complex
% get phase of Er(kx)
Er_TE_kx_phs =atan2(imag(Er_TE_kx), real(Er_TE_kx));
% get Er(x) by inverse FFT
Er_TE_x = fftshift(ifft(Er_TE_kx));
% get phase of Er(x) by processing the Pi/2Pi phase jump at every other sampling point
Er_TE_x_phs =atan2(imag(Er_TE_x), real(Er_TE_x));
E_phs = Er_TE_x_phs;
%plot(x_pos,E_phs)
%E_phs(2:2:length(E_phs)) =pi+E_phs(2:2:length(E_phs));
```

```
E_phs(2:2:315) =pi+E_phs(2:2:315);
%plot(x_pos,E_phs)
E_phs(316:2:2000) = E_phs(316:2:2000)-pi;
%plot(x_pos,E_phs)
E_phs(1743:2:2000) =E_phs(1743:2:2000)-2*pi;
%plot(x_pos,E_phs)
% equivalent process of the phase
%E_phs(2:2:length(E_phs)) =pi+E_phs(2:2:length(E_phs));
%E_phs(316:2:1741) = E_phs(316:2:1741)-2*pi;
%plot(x_pos,E_phs)
%E_phs(1742:2000) =E_phs(1742:2000)-2*pi;
%plot(x_pos,E_phs)
%plot(x_pos,Er_TE_x_phs)
%plot(x_pos,E_phs)
%plot(x_pos(x_pos>9.375 & x_pos<=29.375),E_phs(x_pos>9.375 & x_pos<=29.375))
%Er_TE_x_phs=unwrap(Er_TE_x_phs,0.9*pi);
%Er_TE_x = circshift(Er_TE_x, 45);
%Er_TE_x=Er_TE_x(x_pos-0.7);

% get best matched Er(x) with E0(x) by Goos-Hachen shift some amount
% to maximize power reflectance by Mode integral method (MOI)
shift_size = 41;  % amount of G-H shift in # of sampling points
Er_TE_x_shifted = zeros(1,DFT_size);
Er_TE_x_shifted = [Er_TE_x(shift_size+1:DFT_size), Er_TE_x(1:shift_size)];
%plot(x_pos,abs(Er_TE_x_shifted))

% Calculate power reflectance after G-H shift by MOI
R_TE_MOI=((sum(abs(real(Er_TE_x_shifted)).*Ey_TE_mode)).^2 +(sum (abs(imag …
(Er_TE_x_shifted)).*Ey_TE_mode)).^2)/(sum(Ey_TE_mode.*Ey_TE_mode))^2;

% TM case
%k0=2*pi/lam;
%m=0;
%dx = 0.019375;
%N=2001;
%x0=dx*N/2;
%start_id = 1;

%DFT_size = 2^14+1;
%delta_kx = 2*pi/(DFT_size*dx);
%kx =(-DFT_size/2:DFT_size/2-1)*delta_kx;

[n_eff_TM, x_pos, Ey_TM_mode, Hx_TM_mode] = TM_guide_mode (wg_width,
core_index, clad_index1,clad_index2, lam,m,N,x0,dx, start_id);
power_TM = -0.5*Ey_TM_mode.* Hx_TM_mode;
%figure(2)
%plot(x_pos, Ey_TM_mode)
mode_total_power_TM =sum(power_TM)*dx;
%plot(x_pos, power_TM)
%n_eff_TE = 1.5;
Kz_TM= n_eff_TM*k0;
```

```
theta_critical_TM=asin(1/n_eff_TM);

% Calculate incident angle for each palne wave component
theta_kx_TM=incident_angle+atan(kx/Kz_TM);
n_eff_TM_fft= sqrt(kx.*kx/k0/k0+ n_eff_TM*n_eff_TM);

% Fresnel's equation for TM relection
Rp_fld_kx=(cos(theta_kx_TM)-n_eff_TM_fft.*sqrt(1-(n_eff_TM_fft).^2.*
(sin(theta_kx_TM)).^2))./(cos(theta_kx_TM)+n_eff_TM_fft.*sqrt(1-
(n_eff_TM_fft).^2.*(sin(theta_kx_TM)).^2));

%calculate power reflectance by summation
%theta_kx_tran_TM=theta_kx_TM(theta_kx_TM<theta_critical_TM&
%  theta_kx_TM>=0);
% Snell's Law for theta2_kx
%theta2_kx_TM=asin(n_eff_TM*sin(theta_kx_tran_TM));
% Fresnel formula
%t_kx_TM=(2*n_eff_TM*cos(theta_kx_tran_TM))./(cos(theta_kx_tran_TM)+
%   n_eff_TM*cos(theta2_kx_TM));
%T_power_kx_TM=
%(cos(theta2_kx_TM)./(n_eff_TM*cos(theta_kx_tran_TM))).*abs(t_kx_TM).^2;
%power_reflect_TM=1sum(T_power_kx_TM.*Ey_TM_mode_FFT_amp_2
%(theta_kx_TM<theta_critical_TM & theta_kx_TM>=0))/sum(Ey_TM_mode_FFT_amp_2);

% get Ey(kx) by FFT
FFT_in =zeros(1, DFT_size);
%FFT_in_TM(DFT_size/2-N/2:DFT_size/2-N/2+N-1) = Ey_TM_mode;
FFT_in=Ey_TM_mode;

% Now do FFT on the mode profile
Ey_TM_mode_FFT  = fft(FFT_in, DFT_size);
Ey_TM_mode_FFT = fftshift(Ey_TM_mode_FFT);
%Ey_TM_mode_FFT_amp = abs(Ey_TM_mode_FFT)/max(Ey_TM_mode_FFT);
Ey_TM_mode_FFT_amp = abs(Ey_TM_mode_FFT);
Ey_TM_mode_FFT_amp_2= Ey_TM_mode_FFT_amp.* Ey_TM_mode_FFT_amp;
%Real_Er_kx=Ey_TM_mode_FFT_amp.*real()

%get reflected Er(kx)and Er(x)
Er_TM_kx=Ey_TM_mode_FFT_amp.*Rp_fld_kx;
Er_TM_kx_phs =atan2(imag(Er_TM_kx), real(Er_TM_kx));
Er_TM_x = fftshift(ifft(Er_TM_kx));
Er_TM_x_phs =atan2(imag(Er_TM_x), real(Er_TM_x));
Em_phs = Er_TE_x_phs;
%plot(x_pos,E_phs)
%Em_phs(2:2:length(Em_phs)) =pi+Em_phs(2:2:length(Em_phs));
Em_phs(2:2:315) =pi+Em_phs(2:2:315);
%plot(x_pos,E_phs)
Em_phs(316:2:2000) = Em_phs(316:2:2000)-pi;
%plot(x_pos,E_phs)
Em_phs(1743:2:2000) =Em_phs(1743:2:2000)-2*pi;
```

```
%Er_TM_x_phs=unwrap(Er_TM_x_phs);
%Er_TE_x = circshift(Er_TE_x, 45);
%Er_TE_x=Er_TE_x(x_pos-0.7);
%hold on
%plot(x_pos_shift,abs(Er_TE_x))
Er_TM_x_shifted = zeros(1, DFT_size);
shift_size = 41;
Er_TM_x_shifted = [Er_TM_x(shift_size+1:DFT_size), Er_TM_x(1:shift_size)];
%plot(x_pos,abs(Er_TM_x_shifted))
%calculate power reflectance by MOI
R_TM_MOI=((sum(abs(real(Er_TM_x_shifted)).*Ey_TM_mode)).^2+(sum(abs(imag
(Er_TM_x_shifted)).*Ey_TM_mode)).^2)/(sum(Ey_TM_mode.*Ey_TM_mode))^2;

%output figures of Ey(kx) and abs(Er(kx)), Ey(x) and abs(Er(x)) for TE  light
%plot(x_pos, Ey_TE_mode)
plot(kx(kx<5 & kx>-5), Ey_TE_mode_FFT_amp(kx<5 & kx>-5) …
/max(Ey_TE_mode_FFT_amp (kx<5 & kx>-5)))
hold on
plot(kx(kx<5 & kx>-5),abs(Er_TE_kx(kx<5 & kx>-5))/max(abs(Er_TE_kx(kx<5 & kx>-
5))))
%hold on
figure (2)
plot(x_pos, Ey_TE_mode)
hold on
plot(x_pos,abs(Er_TE_x))
figure (3)
% output phase change of Er(kx) or Er(x) for TE light
plot(kx(kx<5 & kx>-5), Er_TE_kx_phs((kx<5 & kx>-5)))
figure (4)
plot(x_pos(x_pos>9.375 & x_pos<=29.375),E_phs(x_pos>9.375 & x_pos<=29.375))
% the center of the 40 µm-width mode is in 19.375 µm

%output reflectance by MOI for TE and TM
R_TE_MOI
R_TM_MOI

%*******End of main program named Pwr_Ref_singangl.m********


% Function TE_guide_mode() loaded in main

function [n_eff_TE, x_pos, Ey_TE_mode, Hx_TE_mode] = TE_guide_mode(
guideWidth,guideIndex, substrIndex,supstrIndex, waveLength,m,N,x0,deltaX, start_id)

%	real(8):: V % waveguide normalized frequency
%	real(8):: B % waveguide normalized porpogation constant
%	integer,intent(in):: m  % mode subscript
%	real(8),intent(in):: guideWidth % diameter of waveguide core in unit of meter
%	real(8),intent(in):: waveLength % wavelength in free space in unit of meter

%	real(8),intent(in):: guideIndex % refractive index of waveguide core
```

```
%        real(8),intent(in):: substrIndex % refractive index of lower cladding.
%        real(8),intent(in):: supstrIndex % refractive index of upper cladding.
%        integer, intent(in) :: start_id
%        real(8):: cladIndex_biger, cladIndex_smler
%        real(8):: waveNum  % wavenumber in free space
%        real(8):: belta   % waveguide propogation constant
%
%        integer, intent(in):: N % size of corrosponding dimension of FDTD Ey array.
% (Ez for Taflove's convention)
%        real(8), intent(in):: x0 % waveguide central line position in FDTD grid,
% measured from the center of FDTD grid.
%        real(8), intent(in):: deltaX % size of corrosponding dimension of FDTD
% Yee Cell.
%        real(8), allocatable,dimension(:):: x_pos
%        real(8) kapa, sigma, ksi, init_phi
%        integer i
%        real(8) epsi_0, mu_0, c0


         mu_0 = 1.2566e-6;
         epsi_0 = 8.8542e-12;
         c0 = 1.0/sqrt(mu_0 * epsi_0);


         waveNum = 2.0 * pi / waveLength;
         cladIndex_biger = max(substrIndex,supstrIndex);
         cladIndex_smler = min(substrIndex,supstrIndex);

% Calculate Normalized freq.

         V = sqrt((waveNum * guideWidth / 2.0)^ 2 * (guideIndex* guideIndex -
cladIndex_biger * cladIndex_biger));
         B=EIGEN_TE(V,guideIndex,supstrIndex,substrIndex,m);

% Calculate porpogation constant
         belta = waveNum * sqrt(B * (guideIndex *guideIndex - cladIndex_biger *
cladIndex_biger) + cladIndex_biger ...
       *cladIndex_biger);

         n_eff_TE = belta / waveNum;
         kapa = sqrt((waveNum * guideIndex)*(waveNum * guideIndex) - belta *belta);
         sigma = sqrt(belta *belta - (waveNum * supstrIndex)*(waveNum *
supstrIndex));
         ksi = sqrt(belta *belta - (waveNum * substrIndex)*(waveNum * substrIndex));

    x_pos = zeros(1, N);
    x_pos = (start_id-1:N+start_id-2).*deltaX;
%        x_pos = (/(dble(i - 1) * deltaX, i = start_id,N+start_id-1)/)
%        x_pos = (/((i - 1) * deltaX - (N - 1) * deltaX / 2.0, i = 1,N)/)

%        init_phi = m * pi / 2
```

```
            init_phi = get_phi_TE(kapa,sigma,ksi,m);

        Ey_TE_mode = zeros(1,N);
        for i = 1:N
                Ey_TE_mode(i) = find_Ey_TE(init_phi,kapa,sigma,ksi,guideWidth / 2.0,
x_pos(i) - x0);
        end

        Hx_TE_mode = zeros(1, N);
            Hx_TE_mode = -belta / (2.0 * pi * c0 / waveLength * mu_0) .* Ey_TE_mode;

    % *******End of function TE_guide_mode() *******


    % Function find_Ey_TE() loaded in function TE_guide_mode()

    function the_value=find_Ey_TE(init_phi,kapa,sigma,ksi,a,x)
            % init_phi, kapa, sigma, ksi,a, x
            % the_value

            if (x > a)
                    the_value = cos(kapa * a - init_phi) * exp(-sigma * (x - a));
        elseif((x < -a))
                    the_value = cos(kapa * a + init_phi) * exp(ksi * (x + a));
        else
                the_value = cos(kapa * x - init_phi);
            end



    % *******End of function find_Ey_TE() *******

    % Function get_phi_TE() loaded in function TE_guide_mode()

    function the_value=get_phi_TE(kapa,sigma,ksi,m)
            % TE mode means Ey, Hx and Hz. Z is the propogation direction, Y is the
            % uniform direction, and X is the index varying direction.
            % kapa %wavenumbers along x-axis in core.
            % sigma  %wavenumbers along x-axis in upper clading
            % ksi  %wavenumbers along x-axis in lower clading
            % m  %mode subscript
            % the_value  % the phi value

            the_value = m * pi / 2.0 + atan(ksi / kapa) / 2.0 - atan(sigma / kapa) / 2.0;

    % ******End of function get_phi_TE() **********
```

```
% Function TM_guide_mode() loaded in main

function [n_eff_TM, x_pos, Hy_TM_mode, Ex_TM_mode] =
TM_guide_mode(guideWidth,guideIndex, substrIndex,supstrIndex, waveLength, ...
        m,N,x0,deltaX, start_id)

%       real(8):: V % waveguide normalized frequency
%       real(8):: B % waveguide normalized porpogation constant
%       integer,intent(in):: m  % mode subscript
%       real(8),intent(in):: guideWidth % diameter of waveguide core in unit of meter
%       real(8),intent(in):: waveLength % wavelength in free space in unit of meter

%       real(8),intent(in):: guideIndex % refractive index of waveguide core
%       real(8),intent(in):: substrIndex % refractive index of lower cladding.
%       real(8),intent(in):: supstrIndex % refr*active index of upper cladding.
%       integer, intent(in) :: start_id
%       real(8):: cladIndex_biger, cladIndex_smler
%       real(8):: waveNum  % wavenumber in free space
%       real(8):: belta   % waveguide propogation constant
%       integer, intent(in):: N % size of corrosponding dimension of FDTD Ey array.
% (Ez for Taflove's convention)
%       real(8), intent(in):: x0 % waveguide central line position in FDTD grid,
% measured from  the center of FDTD grid.
%       real(8), intent(in):: deltaX % size of corrosponding dimension of FDTD
% Yee Cell.
%       real(8), allocatable,dimension(:):: x_pos
%       real(8) kapa, sigma, ksi, init_phi
%       integer i
%       real(8) epsi_0, mu_0, c0

        mu_0 = 1.2566e-6;
        epsi_0 = 8.8542e-12;
        c0 = 1.0/sqrt(mu_0 * epsi_0);


        waveNum = 2.0 * pi / waveLength;
        cladIndex_biger = max(substrIndex,supstrIndex);
        cladIndex_smler = min(substrIndex,supstrIndex);

% Calculate Normalized freq.

        V = sqrt((waveNum * guideWidth / 2.0) ^ 2 * (guideIndex *guideIndex -
cladIndex_biger *cladIndex_biger));
        B = EIGEN_TM(V,guideIndex,supstrIndex,substrIndex,m);

  % Calculate porpogation constant
        belta = waveNum * sqrt(B * (guideIndex *guideIndex - cladIndex_biger
*cladIndex_biger) + ...
      cladIndex_biger *cladIndex_biger);

        n_eff_TM = belta / waveNum;
```

```
                kapa = sqrt((waveNum * guideIndex)*(waveNum * guideIndex) - belta *belta);
                sigma = sqrt(belta *belta - (waveNum * supstrIndex) *(waveNum *
supstrIndex));
                ksi = sqrt(belta *belta - (waveNum * substrIndex) *(waveNum * substrIndex));
               x_pos = (start_id-1:N+start_id-2).*deltaX;
        %       x_pos = (/((i - 0.5) * deltaX - N * deltaX / 2.0, i = 1,N)/)

        %       init_phi = m * pi / 2
                init_phi = get_phi_TM(kapa,sigma,ksi,m,guideIndex,supstrIndex,substrIndex);

            Hy_TM_mode = zeros(1, N);
            for i = 1:N
                   Hy_TM_mode(i) = find_Hy_TM(init_phi,kapa,sigma,ksi,guideWidth / 2.0,
x_pos(i) - x0);
            end

            Ex_TM_mode = zeros(1, N);


            Ex_TM_mode(x_pos - x0 >= -guideWidth / 2.0 & x_pos - x0 <= guideWidth / 2.0) =
... belta / (2.0 * pi * c0 / waveLength * epsi_0 * guideIndex *guideIndex) .* Hy_TM_mode( ...
              x_pos - x0 >= -guideWidth / 2.0 & x_pos - x0 <= guideWidth / 2.0);

                Ex_TM_mode(x_pos - x0 < -guideWidth / 2.0) = belta / (2.0 * pi * c0 /
waveLength * epsi_0 * substrIndex ^ 2) ...
              .* Hy_TM_mode(x_pos - x0 < -guideWidth / 2.0);

                Ex_TM_mode(x_pos - x0 > guideWidth / 2.0) = belta / (2.0 * pi * c0 /
waveLength * epsi_0 * supstrIndex^ 2) ...
              .* Hy_TM_mode(x_pos - x0 > guideWidth / 2.0);


        % *******End of function TM_guide_mode() *******


        % Function find_Hy_TM() loaded in function TM_guide_mode()


        function the_value = find_Hy_TM(init_phi,kapa,sigma,ksi,a,x)
                %init_phi, kapa, sigma, ksi,a, x

                if (x > a)
                        the_value = cos(kapa * a - init_phi) * exp(-sigma * (x - a));
               elseif ((x < -a))
                        the_value = cos(kapa * a + init_phi) * exp(ksi * (x + a));
               else
             the_value = cos(kapa * x - init_phi);
                end


        % *******End of function find_Hy_TM() **********
```

```
% Function get_phi_TM() loaded in function TM_guide_mode()

function the_value=get_phi_TM(kapa,sigma,ksi,m,ng,ng_up,ng_low)
        % TE mode means Ey, Hx and Hz. Z is the propogation direction, Y is the
        % uniform direction, and X is the index varying direction.
        % kapa %wavenumbers along x-axis in core.
        % sigma  %wavenumbers along x-axis in upper clading
        % ksi  %wavenumbers along x-axis in lower clading
        % m  %mode subscript
        % ng % refractive index of waveguide core
        % ng_up % refractive index of upper clading
        % ng_low % refractive index of lower clading
        % the_value  % the phi value

        the_value = m * pi / 2.0 + atan((ng / ng_low) *(ng / ng_low) * ksi / kapa) / …
 2.0 - atan((ng / ng_up) *(ng / ng_up) * sigma / kapa) / 2.0;



% *******End of function get_phi_TM() *********
```

APPENDIX B

IGOR PROCEDURE FILE FOR CALCULATING BEND EFFICIENCY BASED ON FDTD NUMERICAL SIMULATIONS

```
    // Before running this procedure, the data file of amplitude and phase of E field needs to
//be loaded into Igor as waves (2D data).
    // This function named Bd_slant.ipf runs under the command window of Igor
//environment, and this procedure works on Igor Pro 4.09A.
    //This Igore procedure process data from FDTD simulations to calculate bend efficiency
    //using MOI method for slanted bend cases and waveguide n=1.5, 1.465.

    Function Bd_slant(w_E,w_phs,wm_E,wm_phs,Cord_X,Cord_z,theta)
    variable Cord_X,Cord_z,theta
    wave w_E,w_phs,wm_E,wm_phs
    wave Emd60,Emd60m   // variables and waves in the function must be first defined
    variable BE_E,BE_M,num_points, xValue, yValue

    // wavelength λ=1.55 µm, FDTD grid size λ/60. Actual Yee cell is about 0.0258 µm.
    // Power monitor width is 10 µm, corresponding to 388 cells.

    make/O/N=388  out_e,out_phs,out_ae1,out_ae2,out_aa
    make/O/N=388  outm_e,outm_phs,outm_ae1,outm_ae2,outm_aa

    // Using interpolation method to get best matched E field and phase
    for (num_points = 0; num_points<388; num_points+=1)
        xValue = (Cord_x)*0.0258 -(num_points-
388/2)*0.0258*cos(theta*3.1415926/180)
        yValue = ( cord_z)*0.0258 + (num_points-
388/2)*0.0258*sin(theta*3.1415926/180)
        //Out_p=w_p[Cord_x-72+round(p*0.4586)][cord_z-139+round(p*0.8886)]
        //Out_p[num_points] =  Interp2D (w_p, xValue, yValue)
        out_e[num_points] = Interp2D (w_E, xValue, yValue)
        out_phs[num_points] = Interp2D (w_phs, xValue, yValue)
        outm_e[num_points] = Interp2D (wm_E, xValue, yValue)
        outm_phs[num_points] = Interp2D (wm_phs, xValue, yValue)
    endfor
```

```
//Out_e=w_E[Cord_x][155+p]
//out_phs=w_phs[Cord_x][155+p]
//phs_avg=w_phs[cord_x][217]
//out_phs=out_phs-phs_avg

out_ae1=out_e*cos(out_phs)*Emd60
out_ae2=out_e*sin(out_phs)*Emd60
//out_ae_nop=out_e*outmd_r80
//out_ee=out_e^2
out_aa=Emd60^2
//out_aa2=outmd_r80^2
//Eff_p=sum(out_p,0,517)/sum(inp_r80,0,517)


//Outm_e=wm_E[Cord_x][155+p]
//outm_phs=wm_phs[Cord_x][155+p]

outm_ae1=outm_e*cos(outm_phs)*Emd60m
outm_ae2=outm_e*sin(outm_phs)*Emd60m
outm_aa=Emd60m^2

BE_E=((sum(out_ae1,0,388))^2+(sum(out_ae2,0,388))^2)/(sum(out_aa,0,388))^2
BE_M=((sum(outm_ae1,0,388))^2+(sum(outm_ae2,0,388))^2)/(sum(outm_aa,0,388))^2
//Eff_E_nop=(sum(out_ae_nop,0,517))^2/sum(out_ee,0,517)/sum(out_aa,0,517)
//Eff_all=Eff_p*Eff_E
//Eff_all2=((sum(out_ae1,0,517))^2+(sum(out_ae2,0,517))^2)/sum(out_aa,0,517)/sum(ou
t_aa2,0,517)
//Eff_all_nop=Eff_p*Eff_E_nop

print BE_E,BE_M

end


//*************End of Igor procedure*******************//
```

REFERENCES

[1] L. Eldada, “Advances in telecom and datacom optical components,” Opt. Eng., **40** (7), 1165-1178, (2001).

[2] K. Gilleo, “Photonics challenge to electronic packaging,” IEEE Trans. on Components and Packaging Technol., **24** (2), 309-311, (2001).

[3] J. T. Boyd, “Integrated Optics, Devices and Applications,” Progress in Lasers and Electro-optics, IEEE Press, (1991).

[4] Y. P. Li, C. H. Henry, “Silica-based optical integrated circuits,” IEEE Proc. Optoelectron, **143** (5), 263-280, (1996).

[5] R. Adar, M. R. Serbin, V. Mizrahi, “Less that 1 dB per meter propagation loss of silica waveguides measured using a ring resonator,” J. Lightwave Technol., **12** (8), 1369-1372, (1994).

[6] R. G. Hunsperger, *Integrated Optics*, 5th edit., Springer, (2002).

[7] T. Miya, “Silica-based planar lightwave circuits: Passive and thermally active devices,” IEEE J. Selected Topics in Quantum Electronics, **6** (1), 38-45, (2000).

[8] G. L. Bona, W. E. Denzel, B. J. Offrein, R. Germann, H. W. M. Salemink, F. Horst, “Wavelength division multiplexed add/drop ring technology in corporate backbone networks,” Opt. Eng., **37**, 3218-3228, (1998).

[9] M. Kawachi, “Recent progress in silica-based planar lightwave circuits on silicon,” IEEE Proc. Optoelectron, **143** (5), 1339-1365, (1996).

[10] H. Ma, A. K.-Y. Jen, L. R. Dalton, “Polymer-based optical waveguides: Materials, processing, and devices,” Adv. Mater., **14** (19), 1339-1365, (2002).

[11] C. T. Sullivan, B. L. Booth, A. Husain, “Polymeric waveguides,” IEEE Circuits and Devices, 27-31, (1992).

[12] L. Eldada, L. W. Shacklette, “Advances in polymer integrated optics,” IEEE J. Selected Topics in Quantum Electron., **6** (1), 54-68, (2000).

[13] D. P. Prakash, DV. Plant, D. Zhang, H. R. Fetterman, Proc. SPIE, **1774**, 118, (1993).

[14] J. T. Gallo, J. L. Hohman, B. P. Ellerbusch, R. J. Furmanak, L. M. Abbott, D.M. Graham, C. A. Schuetz, B. L. Booth, "High-density interconnects for 2-dimensional VCSEL arrays suitable for mass scale production," SPIE ITCom2001 Conf. on Modeling and Design of Wireless Networks, Denver, USA, 23-24, (2001).

[15] T. Pliska, V. Ricci, A. C. Le Duff, M. Canva, P. Raymond, F. Kajzar, G. I. Stegeman, "Low loss polymer waveguides fabricated by plasma etching for nonlinear-optical devices operating at telecommunication wavelengths," Tech Digest Quantum Electronics and Laser Science Conference, 138, (1999).

[16] J. E. van der Linden, P. P. Van Daele, P. M. Dobbelaere, M. B. Diemeer, "Compact multichannel in-line power meter," IEEE Photon. Technol. Lett., **11**, 263, (1999).

[17] A. Chen, V. Chuyanov, S. Garner, W. H. Steier, J. Chen, Y. Ra, S. S. H. Mao, G. Lan, L. R. Dalton, "Fast maskless fabrication of electrooptic polymer devices by simultaneous direct laser writing and electric poling of channel waveguides," Proc. Lasers and Electro-optics Society Annual Meeting, LEOS'97, **2**, 250, (1997).

[18] L. Eldada, R. Blomquist, L. Shaklette, M. McFarland, "High performance polymetric componentry for telecom and datacom applications," Opt. Eng., **39**, 596 (2000).

[19] A. Chen, V. Chuyanov, F. Marti-Carrera, S. Garner, W. H. Steier, J. Chen, S. Sun, L. R. Dalton, "Vertically tapered polymer waveguide mode size transformer for improved fiber coupling," Opt. Eng., **39**, 1507, (2000).

[20] Y. Hida et al., Electron Lett., **30** (12), 959-960, (1994).

[21] T. Watanabe et al., Electron. Lett., **33** (18), 1517-1518, (1998).

[22] Y. H. Min, M-H. Lee, J. J. Ju, S. K. Park, J. Y. Do, "Polymeric 16×16 Arrayed Waveguide Grating router using fluorinated polyethers operating around 1550 nm," IEEE J. Selected Topics in Quantum Electron., **7** (5), (2001).

[23] A. Morand, S. Tedjini, P. Benesch, D. Bosc, B. Loisel, "Processing glass electro-optic polymer structure for light modulation and switching," Proc. SPIE, **3278**, 63, (1998).

[24] A. Shoustikov, Y. You, M. E. Thompson, "Electroluminescence color tuning by dye doping inorganic light emitting diodes," IEEE J. Selected Topics in Quantum Electron., **4**, 1077, (1998).

[25] A. Schulzgen, C. Spiegelberg, S. B. Mendes, P. M. Allemand, Y. Kawabe, M. KuwataGonokami, S. Honkanen, M. Fallahi, B. N. Kippelen, N. Peyghambarian, "Light amplification and laser emission in conjugated polymers," Opt. Eng., **37**, 1149, (1998).

[26] A. Melloni, F. Carniel, R. Costa, M. Martinelli, "Determination of bend mode characteristics in dielectric waveguides," J. Lightwave Technol., **19** (4), (2001).

[27] T. Kitoh, N. Takato, M. Yasu, M. Kawachi, "Bending loss reduction in silica-based waveguides by using laterial offsets," J. Lightwave Technol., **13** (4), (1995).

[28] M. Rajarajan, S. Obayya, B. Rahman, et al., "Design of compact optical bends with a trench by use of finite-element and beam-propagation methods," Appl. Opt., **39** (27), 4946-4953, (2000).

[29] C. Seo, J. C. Chen, “Low transition losses in bent rib waveguide,” J. Lightwave Technol., **14** (10), 2255-2259, (1996).

[30] M. Popovic, K. Wada, H. A. Haus, J. Michel, “Air trenches for sharp silica waveguide bends,” J. Lightwave Technol., **20** (9), 1762-1772, (2002).

[31] L. H. Spiekman, Y. S. Oei, et al., “Ultrasamll waveguide bends: The corner mirrors of the future?,” IEEE Proc.-Optoelectron, **142** (1), 61-65, (1995).

[32] R. L. Espinola, R. U. Ahmad, F. Pizzuto, M. J. Steel, R. M. Osgood, Jr., “A study of high-index-contrast 90^o waveguide bend structures,” Opt. Express, **8** (9), 517-528, (2001).

[33] R. U. Ahmad, F. Pizzuto, G. S. Camarda, et al., “Ultracompact corner-mirrors and T-branches in silicon-on-insulator,” IEEE Photon. Technol. Lett., **14** (1), 65-67, (2002).

[34] S. Lardenois, D. Pascal, R. Orobtchouk, “Low-loss submicrometer silicon-on-insulator rib waveguides and corner mirrors,” Opt. Lett., **28** (13), 1150-1152, (2003).

[35] Y. Z. Tang, W. H. Wang, T. Li, Y. L. Wang, “Integrated waveguide turning mirror in silicon-on-insulator,” IEEE Photon. Technol. Lett., **14** (1), 68-70, (2002).

[36] P. Buchmann, H. Kaufmann, “GaAs single-mode rib waveguides with reactive iron-etched totally reflecting corner mirrors,” J. Lightwave Technol., **3** (4), 785-788, 1985.

[37] H. Han, D. V. Forbes, J. J. Coleman, “Self-aligned high-quality total internal reflection mirrors,” IEEE Photon. Technol. Lett., **7** (8), 899-901, (1995).

[38] Y. Chung, N. Dagli, “Analysis of integrated optical corner reflectors using a finite-difference beam propagation method,” IEEE Photon. Technol. Lett., **3** (2), 150-152, (1991).

[39] E. Gini, G. Guekos, H. Melehior, “Low loss corner mirrors with 45^o deflection angle for integrated optics,” Electron. Lett., **28** (5), 499-501, (1992).

[40] A. Himeno, H. Terui, M. Kobayashi, “Loss measurement and analysis of high-silica reflection bending optical waveguides,” J. Lightwave Technol., **6** (1), 41-46, (1988).

[41] S. Wiechmann, H. J. Heider, J. Muller, “Analysis and design of integrated optical mirrors in planar waveguide technology,” J. Lightwave Technol., **21** (6), 1584-1591, (2003).

[42] A. Melloni, R. Costa, F. Carniel, M. Martinelli, “An effective method for the analysis of bent dielectric waveguides,” Proc. LEOS’99, 641-642, (1999).

[43] A. Melloni, F. Carniel, R. Costa, M. Martinelli, “Determination of bend mode characteristics in dielectric waveguides,” J. Lightwave Technol., **19** (4), 571-577, (2001).

[44] C. Manolatou, S. G. Johnson, S. Fan, P. R. Villeneuve, H. A. Haus, J. D. Joannopoulus, “High-Density Integrated Optics,” J. Lightwave Technol., **17** (9), 1682-1692, (1999).

[45] R. Elio, E. El-Sharawy, “Reducing losses in dielectric waveguide discontinuities,” IEEE Transactions on Microwave Theory and Technique, **46** (8), 1045-1054, (1998).

[46] U. Peschel, L. Leine, F. Lederer, C. Wachter, “Bending the path of light with a micro-prism,” Tuesday morning, CLEO 2001, 129-130, (2001).

[47] J. D. Joannopoulos, R. D. Meade, J. N. Winn, *Photonics Crystals*, Princeton U. Press, Princeton, N. J. (1995).

[48] R. D. Meade, A. Devenyi, J. D. Joannopoulos, et al., "Novel applications of photonics band gap materials: low-loss bends and high Q cavities," Science, **282**, 274-276, (1998).

[49] E. Chow, S. Y. Lin, J. R. Wendt, S. G. Johnson, J. D. Joannopoulos, "Quantative analysis of bending efficiency in photonic crystal waveguide bends at $\lambda = 1.55$ μm wavelengths," Opt. Lett., **26** (5), 286-288, (2001).

[50] C. Chen, A. Sharkawy, D. W. Prather, "Optimizing bending efficiency of self-collimated beams in non-channel photonic crystal waveguides," Opt. Express, **11** (23), 3153-3159, (2003).

[51] G. P. Nordin, S. Kim, J. Cai, J. Jiang, "Hybrid integration of conventional waveguide and photonic crystal structures," Opt. Express, **10**, 1334-1341 (2002), http://www. opticsexpress. org/abstract. cfm?URI=OPEX-10-23-1334.

[52] T. Shiina, K. Shiraishi, S. Kawakami, "Waveguide-bend configuration with low-loss characteristics," Opt. Lett., **11** (11), 736-738, (1986).

[53] H.-B Lin, J. –Y Su, P.-K Wei, W.-S Wang, "Design and application of very low-loss abrupt bends in optical waveguides," IEEE J. Quantum Electron., **30** (12), 2827-2835, (1994).

[54] C.-T Lee, M. –L Wu, "Apexes-linked circle gratings for low-loss waveguide bends," IEEE Photon. Technol. Lett., **13** (6), 597-599, (2001).

[55] S. -P Han, C. -G Choi, S. -H Ahn, et al. "A simple structure of low-loss large-angle abrupt-bend waveguide," IEEE Photon. Technol. Lett., **13** (10), 1085-1087, (2001).

[56] *Rsoft Inc*., www. rsoftinc.com.

[57] *Photon Design*, www. photond. com.

[58] C. A. Balanis, *Advanced Engineering Electromagnetics*, Wiley, New York, (1989).

[59] J. Jiang, "*Rigorous Analysis and Design of Diffractive Optical Elements*," A dissertation from U. of Alabama in Huntsville, (2000).

[60] J. Berenger, "A perfectly matched layer for the absorption of electromagnetic waves," J. Comput. Physics, **114**, 185-200, (1994).

[61] V. P. Tzolov, D. Feng, S. Tanev, Z. J. Jakubczyk, "Modeling tools for integrated and fiber optical devices,"162-173, SPIE conf. on integrated optics devices III, Proc. SPIE, **3620**, (1999).

[62] D. Correia, J. P. da Silva, H. E. Hernandez-Figueroa, "Generic algorithm and finite-element design of short single-section passive polarization converter," IEEE Photon. Technol. Lett., **15** (7), 915-917, (2003).

[63] J. Jiang, G. Nordin, "A rigorous unidirectional method for designing finite aperture diffractive optical elements," Opt. Express, **7** (6), 237-242 (2000).

[64] M. F. van der Vliet, G. Beelen, "Design and simulation tools for integrated optic circuits," SPIE conf. on integrated optics devices III, Proc. SPIE, **3620**, 174-184, (1999).

[65] *BeamPROP* manual from *Rsoft Inc*. (2001).

[66] D. F. G. Gallagher, T. P. Felici, "Eigenmode expansion methods for simulation of optical propagation in photonics-Pros and Cons," Proc. SPIE, **4987**, 69-82, (2003).

[67] R. Orobtchouk, S. Laval, D. Pascal, A. Koster, "Analysis of integrated optical waveguide mirrors," J. Lightwave Technol., **15** (5), 815-820, (1997).

[68] S. T. Lau, T. Shiraishi, P. R. McIsaac, et al., "Reflection and transmission of a dielectric waveguide mirror," J. Lightwave Technol., **10** (5), 815-820 (1992).

[69] R. Syms, J. Cozens, *Optical Guided Waves and Devices*, McGraw-Hill, New York, Chapter 6 and 9, (1992).

[70] K. Okamoto, *Fundamentals of Optical Waveguides*, Academic Press, San Diego, (2000).

[71] K. Ogusu, "Transmission characteristics of optical waveguides corners," Opt. Communications, **55** (3), 149-153, (1985).

[72] R. Le Dantec, T. Benyattou, G. Guillot, et al., "Tunable microcavity based on InP-air Bragg mirror," IEEE. J. Selected Topics on Quantum Electronics, **5** (1), (1999).

[73] M. V. Klein, T. E. Furtak, *Optics*, 2^{nd} Ed. John Wiley and Sons, New York, (1986).

[74] L. Li, G. P. Nordin, J. English, J. Jiang, "Small-area bends and beamsplitters for low-index-contrast waveguides," Opt. Express, **11** (3), 282-290, (2003).

[75] M. Born, E. Wolf, *Principles of Optics*, 7^{th} ed., Chapter 1, Cambridge University Press, (1999).

[76] F. de Fornel, *Evanescent Waves from Newtonian Optics to Atomic Optics*, Chapter 1, Springer, (2001).

[77] E. Collett, "*Polarized Light: Fundamentals and Applications*," Marcel Decker, New York, (1993).

[78] M. Martinelli, J. C. Palais, "Dual Fiber-ring depolarizer," J. Lightwave Technol., **19** (6), 899-905, (2001).

[79] P. Shen, J. C. Palais, "Passive single-mode fiber depolarizer," Appl. Opt., **38**, 1686-1691, (1999).

[80] H. Hatami-Hanza, J. Nayyer, S. Safavi-Naeini, "Extinction ratios and scattering loss of optical intersecting-waveguide switches with curved electrodes," J. Lightwave Technol., **12** (8), 1475-1481, (1994).